POLITECNICO
MILANO 1863

DIPARTIMENTO DI
INGEGNERIA CIVILE E AMBIENTALE

MŰEGYETEM 1782

BUDAPESTI MŰSZAKI
ÉS GAZDASÁGTUDOMÁNYI EGYETEM
Építőmérnöki Kar - építőmérnöki képzés 1782 óta

Tartószerkezetek Mechanikája Tanszék

Multi-scale Topology Optimization with Graded Microstructures

Doctoral Dissertation of:
Hussein Ismail

Advisors: Prof. János Lógó and Prof. Matteo Bruggi
Tutor: Prof. Stefano Mariani
Year 2024 - XXXVI Cycle

Abstract in English

The optimal design of lightweight structural components subjected to single and multiple loading conditions is explored through a multi-scale topology optimization framework. The challenges posed by the incorporation of graded infills and the enforcement of displacement constraints are addressed.

The methodology relies on the formulation of multi-constrained minimum volume problems of topology optimization which are solved via an augmented Lagrangian method, as inspired by recent advancements in stress-based structural optimization. The assessment of the structural performances of 2D/3D isotropic microstructures given by hexagonal close-packed arrangements of circular/spherical holes in a continuous medium is provided. Numerical homogenization is used to derive the macroscopic elastic properties of several type of isotropic and orthotropic cells that can play as an infill for lightweight structures. The adoption of suitable interpolation laws for managing the design of two-material structures made by a full phase and a graded one, along with void, is investigated. The thesis delves into the design of composite structures not only by considering deterministic loads, but also by providing a focus on the impact of uncertainties that may affect the loading amplitude. Sequential convex programming is utilized to tackle the arising multi-constrained problems, considering both deterministic and probabilistic displacement enforcements.

The findings highlight the effectiveness and the numerical efficiency of the proposed approaches in optimizing lightweight structural components composed by a solid phase and an infill one. The achieved composite layouts leverage on the potential of additive manufacturing in creating complex porous layouts to gain stiffness and redundancy of the load path. The research contributes insights regarding the optimal design of lightweight components, when the optimization of both their boundaries and the internal arrangement of the infill is dealt with. The relevance and impact of these methodologies in practical engineering applications is highlighted, especially in light of the adoption of additive manufacturing for fabrication.

Keywords: Multi-Scale Topology Optimization, Displacement-Constrained Design, Graded Infill Structures, Additive Manufacturing, Lightweight Structures.

Magyar nyelvű absztrakt

A dolgozat a többszintű (mikro illetve makró szinteket magába foglaló) topológiai optimálási keretrendszer felhasználásával egy illetve több terhelési esetbe integrált terhekkel terhelt minimális súlyú szerkezeti elemek optimális tervezését mutatja be. Megoldást adok az osztályozott kitöltések (a 0-1 megoldások közötti részek) és az elmozdulási feltételek érvényesítése jelentette kihívásokra.

A módszertan a topológia optimalizálás többszörös feltételű minimális térfogati célfügvénnyel definiált feltételes szélsőérték problémáinak megfogalmazásán alapul, amelyeket egy kiterjesztett Lagrange-módszerrel oldok meg, a feszültség alapú szerkezeti optimalizálás legújabb fejlesztései alapján. A 2D/3D izotróp mikrostruktúrák szerkezeti teljesítményének értékelését körkörös/gömb alakú lyukak hatszögletű, szorosan egymásra épülő elrendezése adja folyamatos közegben. A numerikus homogenizálást számos izotróp és ortotróp cellák makroszkopikus rugalmas tulajdonságainak származtatására használom, amelyek a könnyűszerkezetek kitöltéseként szolgálhatnak. Megvizsgáltam a megfelelő interpolációs eljárások alkalmazhatóságát a két anyagból álló szerkezetek teljes fázisú és fokozatos, az ürességgel együtt történő tervezésének kezelésére. A dolgozat nemcsak a determinisztikus terhelések figyelembe vételével, hanem a terhelési amplitúdót befolyásoló bizonytalanságok hatásával is foglalkozik a kompozit szerkezetek tervezésénél. A szekvenciális konvex programozást a felmerülő, többszörös feltételekkel megfogalmazott szélsőérték problémák kezelésére használom, figyelembe véve mind a determinisztikus, mind a valószínűségi változókkal leírt elmozdulási feltételeket. Az eredmények rávilágítanak a javasolt megközelítések hatékonyságára és numerikus alkalmazhatóságára a szilárd fázisból és egy kitöltőből álló könnyű szerkezeti elemek optimalizálása terén.

Az elért kompozit elrendezések kihasználják az additív gyártásban rejlő lehetőségeket összetett porózus elrendezések létrehozásában, a terhelési út merevségének és redundanciájának növelése érdekében. A kutatás betekintést ad a minimális súlyú alkatrészek optimális kialakításába, ha mind az alak (határvonalak), mind a kitöltés belső elrendezésének optimalizálásával foglalkozunk. Ezeknek a módszereknek a relevanciája és hatása a gyakorlati mérnöki alkalmazásokban kiemelkedik, különösen az additív gyártás alkalmazásának fényében.

Kulcsszavak: Többszintű topológia optimalizálás, elmozdulás korlátozott tervezés, osztályozott kitöltésű szerkezetek, additív gyártás, könnyűszerkezetek.

Abstract in lingua italiana

La tesi tratta della progettazione ottimale di componenti strutturali alleggeriti, sottoposti a casi di carico singoli e multipli, tramite tecniche di ottimizzazione topologica multiscala. Il lavoro si concentra sulla definizione della gradazione ottimale di materiali porosi di rimepimento per componenti strutturali, in presenza di vincoli per il controllo del campo di spostamento.

Vengono formulati problemi di ottimizzazione topologica per la ricerca di soluzioni di minimo volume in presenza di vincoli locali, questi ultimi trattati con un metodo di tipo Lagrangiano aumentato, ispirato ai recenti progressi nel campo dell'ottimizzazione con vincoli di sforzo. E' verificata l'adeguatezza delle prestazioni strutturali di microstrutture isotrope 2D/3D la cui geometria è caratterizzata da disposizioni a base esagonale di fori circolari/sferici a raggio variabile. Vengono impiegati metodi di omogeneizzazione numerica per ricavare le proprietà elastiche alla macroscala per diversi tipi di celle isotrope e ortotrope idonee all'alleggerimento dei componenti strutturali. Si propongono opportune leggi di interpolazione di materiale per la gestione della distribuzione di materiale pieno, poroso e vuoto. La tesi approfondisce la progettazione di strutture in materiale composito non solo considerando carichi deterministici, ma anche indagando l'impatto delle incertezze che possono influenzare l'intensità dei carichi applicati. La programmazione sequenziale convessa viene utilizzata per risolvere i problemi multi-vincolati che ne derivano, sia nel caso di carichi deterministici che probabilistici.

I risultati evidenziano l'efficacia e l'efficienza degli approcci di ottimizzazione di componenti strutturali composti da materiale pieno e riempimento di tipo poroso. Le soluzioni ottenute sfruttano il potenziale della produzione additiva nella realizzazione di geometrie complesse per ottenere rigidezza e ridondanza nel percorso di trasferimento del carico. La ricerca fornisce spunti per la progettazione ottimale di componenti strutturali alleggeriti, considerando la contemporanea definizione del profilo per i bordi esterni e disposizione e gradazione del materiale poroso di riempimento. L'utilizzo delle tecniche proposte è di rilievo per le applicazioni ingegneristiche, soprattutto alla luce dell'adozione della manifattura additiva per la fabbricazione.

Parole chiave: ottimizzazione topologica multiscala, vincoli sugli spostamenti, strutture in materiale composito, manifattura additiva, strutture alleggerite.

Acknowledgements

I would like to express my deepest gratitude to a number of people and organizations whose support was indispensable in the completion of this dissertation. Firstly, my sincerest thanks go to my parents and friends for their unwavering love, encouragement, and belief in my abilities throughout this journey. Your support has been my cornerstone.

I am profoundly grateful to the Stipendium Hungaricum for awarding me the PhD scholarship that made my studies possible. This opportunity has been instrumental in shaping my academic and professional pursuits.

Special thanks are due to my supervisors, Prof. János Lógó and Prof. Matteo Bruggi, for creating the joint PhD opportunity between BME and POLIMI. Their infinite support and guidance have been crucial to my research and personal growth. Without their wisdom and mentorship, this work would not have been possible.

I would also like to acknowledge the professors in both departments at BME and POLIMI for their contributions to my academic experience.

Lastly, I am thankful for the grants that financed our research, providing us with the resources necessary to succeed, particularly, the National Research, Development and Innovation Office (grant K 119440 and K 138615) and Joint grant of the Hungarian and the Polish Academy of Science.

This dissertation stands as a testament not only to my personal efforts but also to the collaborative spirit of all those who supported me along the way. Thank you.

Contents

Abstract in English **i**

Magyar nyelvű absztrakt **ii**

Abstract in lingua italiana **iii**

Acknowledgements **iv**

Contents **v**

1 Introduction **1**

1.1 History of Topology Optimization 1

1.1.1 The Inception of Topology Optimization 1

1.1.2 Evolution of Solution Techniques 4

1.2 Significant Milestones in Topology Optimization Over the Past Three Decades . 7

1.2.1 Optimization Methods 7

1.2.2 Key Publications and Notable Findings 7

1.2.3 Educational Publications and Codes 10

1.2.4 Multiscale Topology Optimization in Additive Manufacturing 11

1.3 Foundations of Probability in Topology Optimization 13

1.3.1 Overview of Topology Optimization Under Uncertainty 13

1.3.2 Computational Techniques in Topology Optimization Under Uncertainty 15

1.4 Problem Statement 16

1.5 Software Utilized in Our Research 17

2 Topology Optimization for Loads with Multiple Points of Application **18**

2.1 Problem formulation and Implementation 19

2.1.1 Detailed Problem Statement 19

2.1.2 Numerical Implementation Details 20

2.2 Case Studies and Numerical Simulations 22

2.2.1 Cantilever Beam . . . 23
2.2.2 Single Span Beam . . . 26
2.2.3 Two-Span Beam . . . 28
2.3 Summary and Conclusions . . . 30

3 Lightweight Additive Design: Graded Porosity with Displacement Constraints 32
3.1 Preliminaries . . . 33
3.1.1 Material Law . . . 34
3.1.2 A Two-Phase Material Model with Void . . . 38
3.2 Design for Minimum Weight Under Displacement Constraints . . . 39
3.2.1 Formulation . . . 39
3.2.2 Numerical Implementation . . . 40
3.2.3 Post-Processing for Manufacturing . . . 41
3.3 Numerical Simulations . . . 42
3.3.1 Design of a Simply-Supported Beam Under Multiple Load Cases . . . 43
3.3.2 Design of a Cantilever Beam Under a Uniformly Distributed Load . . . 48
3.3.3 Design of a Three-Dimensional Cantilever Beam . . . 53
3.4 Summary and Conclusions . . . 55

4 Enhanced Topology Optimization: Graded Infill for Loading Uncertainty 57
4.1 Uncertainty in Multi-Scale Topology Optimization . . . 57
4.2 Method: Theory to Implementation . . . 58
4.2.1 Material Law . . . 58
4.2.2 Probabilistic Formulation . . . 61
4.2.3 Numerical Implementation . . . 64
4.3 Numerical Case Studies . . . 64
4.3.1 Assessment of the Formulation: A Short Beam with Fixed Ends . . . 65
4.3.2 Structural Response in Case of Correlated Load . . . 68
4.3.3 Mechanical Response of the Optimal Layouts in Probabilistic Terms . . . 72
4.4 Summary and Conclusions . . . 76

5 Theses, and Future Developments 78
5.1 Theses . . . 78
5.2 Future Development . . . 79
5.3 List of Publications . . . 80

Bibliography 82

List of Figures **96**

List of Tables **99**

A Appendix A **100**
A.1 3D Isotropic behavior of HCP 100
A.2 Filtering 101
A.3 Solving Algorithm 102
A.4 Sensitivity 103
A.5 Topology Optimization Accounting for Self-Weight - Optimal Grading for an Infill Problem 104

B Appendix B **108**
B.1 Filtering 108
B.2 Sensitivity Computation 109
B.3 Preliminary Assessment of the Three-variable Multi-scale Approach, a Cantilever 110
B.4 Effect of Different Correlations of Loads 112

1 | Introduction

1.1. History of Topology Optimization

The field of structural optimization, particularly topology optimization, has been a focal point of engineering research for approximately 150 years. This review provides an examination of key developments within this field, highlighting how initial progress, once obscured by secrecy, featured significant contributions from researchers at renowned institutions like Cambridge and Oxford Universities during the 1950s. The advent of digitalization in the post-1970s era transformed the field, dramatically enhancing the accessibility and documentation of research. This shift greatly improved the dissemination of knowledge within the optimization community, marking the evolution of topology optimization from a niche academic area to a well-established and extensively documented field of study.

1.1.1. The Inception of Topology Optimization

Topology optimization is considered a complex computational procedure as it includes the elements of the size and shape optimization. In the case of skeletal structures, it integrates the layout optimization and the optimal cross-section design simultaneously. While many academic papers credit Michell's work from 1904 as the first in topology optimization, it is worth noting that the pioneering contribution was actually made by Maxwell [97]. This can be inferred from Michell's own acknowledgement in his paper, stating that he "only" extended Maxwell's results after 34 years [101]. Both Maxwell and Michell presented closed-form solutions for designing structures with minimum volume. Their works laid the foundation for subsequent developments in the field of topology optimization.

Before the history of topology optimization is discussed, one has to mention two important theories in mathematical programming [55]: the Farkas lemma for linear programming [57] and the Karush–Khun–Tucker conditions for nonlinear programming [72, 105]. In addition, the basic idea of multicriteria mathematical programming presented by Pareto [112] also plays a pivotal role. Without these theorems, the numerical procedures in topology optimization could not develop so effectively and rapidly.

The selection of the achievements in this field is a rather difficult task because in the early pe-

riod of the topology optimization history many meetings were classified and the results were not available for the public. The optimization community has almost no knowledge about the publications in topology optimization in the 1950s. Around that time, one can find some information on workshops and meetings connected to the Cambridge University or Oxford University with researchers such as Foulkes, Cox, Hemp, and Shield, who published significant results and these communications are generally not known for the reason mentioned above. After the 1970s of the 20th century, this situation has changed and there were more possibilities to find publications due to the changes and thanks to the digitalization. As indicated earlier, here subjectively selected works are overviewed from the optimization topology history focusing on the first 120 years.

Maxwell [97] in 1870, Cilley [36] in 1900 and Michell [101] in 1904 used the principle of full stress design (FSD) criteria in the case of statically determinate structures and obtained the same results as the minimum weight design. It is necessary to mention that for the final result the procedure took one iteration only. They concluded that FSD was the same as minimum weight design for statically determinate structures.

According to the literature research on the theorem of the optimal design, the topology design remained unnoticed for some fifty years until the publication of the papers of Foulkes [59], Cox [44] and Hemp [127]. The years around 1955 can be called the "golden age" of the optimal layout design of trusses. Independently from the English school, one can find several papers that can be named as original ideas of different topology branches. Among others, the papers written by Sved [146] and Barta [9] are the most significant ones. These two works have a lot of similarities in contents and conclusions. Barta's paper discussed the minimum volume design of plane and space structures (trusses). He proved the following theorem: "by removing a given number of properly chosen redundant bars from a given network, it was possible to obtain such a statically determinate structure, which yields a structure with the least weight". He also mentioned that "the proof did not guarantee that only the statically determinate structure could be the least weight solution".

Sved's paper can be considered as the origin of the stress limited and minimum volume design. It is also important to note that the minimum weight designs of different types of structures were studied by Drucker and Shield [51], Mróz [103], Prager and Shield [119] and their results are significant to understand the optimality in the case of complex problems.

The true surge in layout theory research was in the 1960s and 1970s. In the 1960s, the significant publications helped to derive optimality conditions for minimum volume designs. Shield [131] presented optimum design methods for multiple loading. He used variational principles to prove the optimality. In 1960 Schmit [128] applied FSD to statically indeterminate struc-

tures and found that FSD provides the exact optimum in a single sizing operation for statically determinate structures where the internal forces remain constant during resizing. However, for indeterminate structures, the number of resizing iterations can vary from a few to many as a function of the sensitivity of internal forces to changes in member sizes. The reason why these different results were obtained is known now: it mainly depends on the redundancy of structures or in other words, it depends on whether the internal forces remain almost constant during resizing, as it happens in most well designed practical structures.

During these years, Cox [44], Hemp [127], Prager and Shield [119], Prager and Taylor [120], Prager [116], Prager and Rozvany [118] elaborated several theories that can be named as the origins of the exact structural topologies. Nagtegaal and Prager [104] investigated the optimal truss layout theory in the case of alternative loads. Prager [117] derived an optimality condition for beams and frames subjected to alternating loading using the Foulkes mechanism. His results were based on the extension of the optimality conditions presented by Chan [33]. Prager and Rozvany [118] extended the existing optimal layout theory originally used for low volume fraction to grid-like structures.

The origins of the numerical solution technique of the constrained optimality criteria (COC) methods were presented by Berke and Khot [19] in 1974. This provided the mathematical background of an effective solution technique in topology optimization. The first numerical procedure for finite element (FE) based topology optimization was elaborated by Rossow and Taylor [124] in 1973, but its biggest development started at the end of the 1980s represented by works of Bendsøe and Kikuchi [17] and Rozvany [126].

It is important to mention the works of Kazinczy – the inventor of the plastic hinge theory [75] in 1914 – who produced significant results in this field but unfortunately his publications have remained unexplored. He investigated the volume minimization of trusses as an object of the economical design. Kazinczy was also among the first researchers who investigated the problem of the statically indeterminate trusses in the case of multiple load conditions [76]. Using the Cremona-type solution procedure, he investigated the case of the pre-stressing technique to reach the uniform collapse of the member forces in the case of statically indeterminate structures. With this technique, he used the shakedown theory without naming it, much earlier than Melan [98] published his work on it in 1936. This Cremona-type solution technique has recently been used again as a numerical procedure in topology design [155] . Kazinczy also discussed the questions of safety and reliability designs much earlier than anybody else in the world. Returning to Michell structures and theories connected to them, the recent book of Lewiński et al. [86] is a very complex and extensive study with new findings on this topic.

1.1.2. Evolution of Solution Techniques

Maxwell's problem [97] can be described as follows: consider a truss which maintains equilibrium with a set of forces $\bar{F}_i$ acting at the points $\bar{r}_i$, (i = 1, 2, ..., n). Denote by T_t the load carried in a typical tension member with length L_t and the section area A_t while in the case of typical compression members these variables are T_c, L_c and A_c. The permissible stresses were denoted by f_t and f_c, respectively. By the use of the principle of virtual work, Maxwell derived the optimality condition of the lightest structure, which has the volume given by:

$$V = V_c\left(1+\frac{f_c}{f_t}\right)+\frac{1}{f_t}\sum_i \bar{F}_i\bar{r}_i = V_t\left(1+\frac{f_t}{f_c}\right)-(1/f_c)\sum_i \bar{F}_i\bar{r}_i, \tag{1.1}$$

Here V_t is the volume of all the tension members and V_c is the volume of all the compression members.

The Michell problem can be described as follows: in addition to Maxwell's problem above, let us consider a series of external forces $\bar{F}_i$ acting at the points $\bar{r}_i$, (i = 1, 2, ..., n). Let D be a domain of space containing the points $\bar{r}_i$, (it should be noted that D can be the whole of feasible space). Consider then all possible frameworks (trusses) S, contained in D, which equilibrate the forces $\bar{F}_i$ and satisfy the limiting conditions on stresses. Let us assume that there is a framework S^* that satisfies the following condition of Michell: "There exists a virtual deformation of the domain D such that the strain along all members of S^* is equal to $\pm$e, where e is a small positive number, and where the sign agrees with the sign of the end load carried by the particular member, and further that no linear element of D has strain numerically greater than e." Michell's theorem states that the volume V^* of S^* is less than or equal to the volume V of any of the frameworks S.

$$V = \frac{(f_t+f_c)}{2f_tf_c}\sum_t L_tT_t+\sum_c L_cT_c-\frac{(f_t-f_c)}{2f_tf_c}\sum_i \bar{F}_i\bar{r}_i, \tag{1.2}$$

The actual value of V^* follows from the principle of virtual work. If the virtual displacements corresponding to Michell's statement above are $e\bar{v}_i$ at $\bar{r}_i$ this volume V^* is:

$$V^* = \frac{(f_t+f_c)}{2f_tf_c}\sum_i \bar{F}_i\bar{v}_i-\frac{(f_t-f_c)}{2f_tf_c}\sum_i \bar{F}_i\bar{r}_i, \tag{1.3}$$

The character of the deformation e imposes certain restrictions upon the layout of members in S^*. At a node of this framework, the directions of the strains $\pm$e, which are along the lines of members of S^* and are principal directions of strain, must satisfy certain orthogonality conditions. In a three-dimensional truss, at a node with three members, there are no restrictions if the loads in the members have the same sign, since in that case the virtual deformation is a pure dilatation and therefore isotropic. If one load is of opposite sign to the others, it must be at right

angles to them. For a node with four members, there is again no restriction if all the loads have the same sign. If one member has an opposite load to the other three, then it must be orthogonal to them all and so forces them to lie in a plane. Finally, if the members fall into pairs with opposite-signed loads, then one of these pairs must be in line and normal to the other two.

Michell also presented a very important property of the optimal structure: the optimum structure S^* has greater stiffness than any other structure of S. He also presented the value of the strain energy stored in the optimal structure.

It is noted that the original formulas of Michell are not valid for different allowable stresses in tension and compression. In 1960 A.S.L. Chan [31] and in 1963 H.S.Y. Chan [32], wrote down correctly Michell's theorem. The validity and the critical examination of Michell's theorem can be read in Rozvany's work [125] published almost 40 years later, too. One can also find a very specific overview of Michell's theorem and its extension in the book of Lewiński et al. [86]. Different theorems were presented in the book of Brandt [23], where minimum-potential criterion of Wasiutynski is presented.

Applications of the theorems of Maxwell and Michell to simple design problems have been made by Cox [45]. He has considered, first of all, the problem of three coplanar forces. In the case where their point of intersection lies within the triangle formed by their points of application, the optimum framework can consist of tension or compression members only. Some of his layouts are given in Figure 1.1. We have to note that all these structures have equal weights. One can recognize the non-uniqueness of the optimal layout and we can have an infinite number of solutions ranging from mechanisms through simple stiff structures to structures of any degree of redundancy.

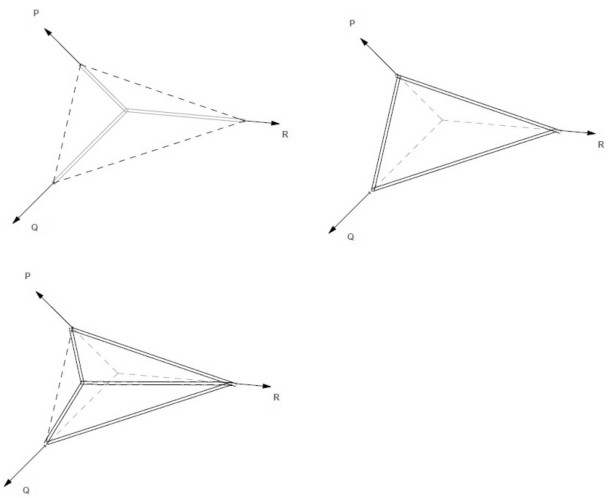

Figure 1.1: Simple tension structures by Cox.

Cox [45] extended the theory presented above to build a structure for the transmission of a bending moment. He showed that if the proportion of length over height of the structure is greater than 4, this structure is considerably lighter than a "simple tie and strut", and that for larger values of $\frac{length}{height}$ proportion, multiple constructions, along the lines of Figure 1.2, can be even lighter. He produced a competitive 14-bar framework and a variation of Figure 1.2a in which the circles are replaced by spirals, which for $\frac{length}{height} > 4$ is lighter than any other construction considered. These structures for the transmission of bending moments are not Michell's optimum structures, since they fail to satisfy the orthogonality conditions for members with opposite signed loads.

The derivation of the optimal layout of pure bending and the optimal solution of Cox's beam problem in Figure 1.2a was presented by Chan [31] in 1960 (Figure 1.2b). The solution of Shield [132] for the same problem can be seen in Figure 1.2c

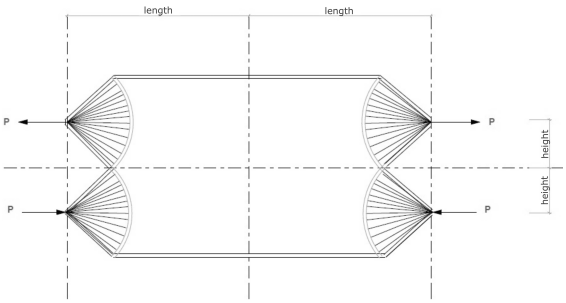

(a) Cox's optimal beam for bending.

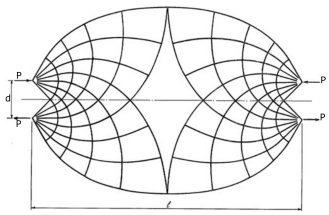

(b) The optimal solution for pure bending presented by Chan [31].

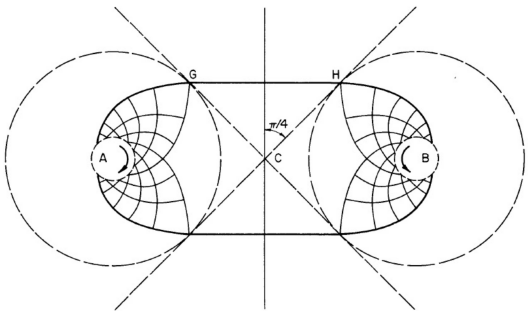

(c) The optimal solution for pure bending presented by Shield [132].

Figure 1.2: The development of the optimal solution for a beam under pure bending.

As it was indicated by Cox's work in the previous section, the optimal solutions are not unique in the case of Michell's structures. By using variational calculus, Shield [132] presented appropriate necessary conditions for the structural volume to be stationary, but he noted that there is

no guarantee to get the global optimum. This section is based on Shield's original work [132], and below the outline of the original paper is presented.

1.2. Significant Milestones in Topology Optimization Over the Past Three Decades

1.2.1. Optimization Methods

The special approaches used to solve successfully the majority of the problems in the second half of the 20th century are known in the literature as optimality criteria methods. Optimality criteria methods are based on radically different thinking from those applied in the development of the mathematical programming (MP) methods. Most MP methods concentrate on obtaining information from conditions around the current design point in design space in order to answer two questions: in what direction and how far to go to best reduce the value of the objective function directly. This is repeated until no more reduction is produced in the iterations within some selected tolerance. On the other hand, optimality criteria methods, exact or heuristic, derive or state conditions characterizing the optimum design, then find or change the design to satisfy those conditions while indirectly optimizing the structure.

The origin of the classical optimality criteria method (COC) dates back to the 1970s. By turning attention to certain stiffness-related constraints, theoretically valid optimality criteria were derived for discretized structures with displacement constraints employing classical Lagrangian multiplier methods of mathematical optimization. To satisfy the optimality criteria, an algorithm was proposed by Berke [18] and later Berke and Khot [19], based on the approach that if it provides an exact direct formula for statically determinate structures, same as FSD, then it would converge in a few iterations for most practical structures, again same as FSD. The difference, however, is an important one; this criterion, unlike FSD, was theoretically correct also for indeterminate structures. Furthermore it resulted in the separability of variables leading to member-by-member resizing, similar in this respect to FSD, thus inheriting its often benign convergence behavior. Berke also suggested that the design variables and constraints should be separated into a passive and active set. One can see the similarity in terminology and general steps of the COC method and the SIMP (solid isotropic material with penalization) method-one of the leading solution procedures in topology optimization recently.

1.2.2. Key Publications and Notable Findings

After the original homogenization technique to topology optimization was published in 1988, by Bensoe and Kikuchi [17], several new computational concepts and procedures were elaborated.

The most frequently applied computational methods are:

a) Density-based method (Bendsøe [13], Zhou and Rozvany [166], Mlejnek [102]), which is very often called SIMP;

b) Evolutionary approaches, [158], where the density and evolutionary approaches use simple element or nodal-based design variables.

c) The topological derivative (Sokołowski and Zochowski [141]). The basic idea is to predict the influence (derivative) of introducing an infinitesimal hole at any point in the design domain and use this as the driver for the generation of new holes;

d) The level set method (Allaire et al. [3], Wang et al. [154]) aims to combine some advantages of the shape sensitivity method and the topology approach. The method uses shape derivatives for the development of the optimal topology.

e) The phase-field (Bourdin and Chambolle [22]) approach works directly on the density variables and considers the minimization of a functional.

The methods mentioned above created the first genera directions in the field of continuum-based topology optimization. To overcome a serious numerical problem, that is, to avoid the checkerboard pattern, several filtering techniques and procedures were developed.

As quick as the numerical methods in topology design developed, the demand to verify analytically the numerically obtained optimal topologies increased. The first analytical solutions come from Rozvany and his research colleagues. In figure 1.3, one can see the analytical solution published by Lewiński, Zhou and Rozvany [85].

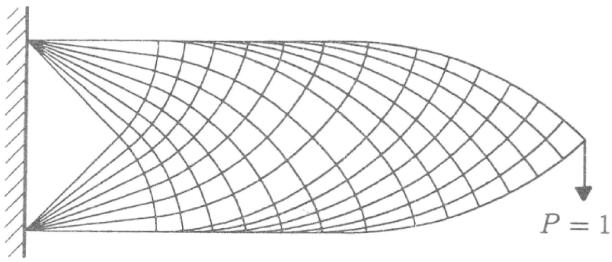

Figure 1.3: The exact optimal solution by Lewiński, Zhou and Rozvany [85].

A very similar solution and detailed calculation were published by Melchers [99]. Another well-known problem, the L-shape structure, was also solved by Lewiński and Rozvany [84]. In figure 1.3 and 1.4, one can see the analytically derived solution.

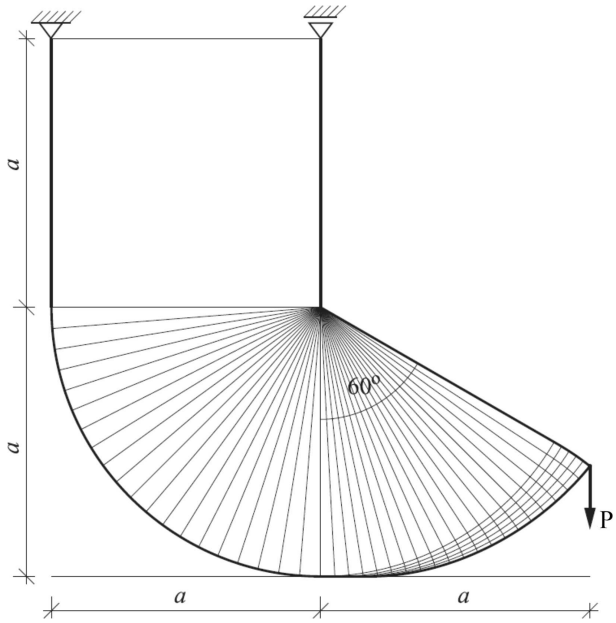

Figure 1.4: The exact optimal solution of the L-shape beam by Lewiński and Rozvany [84].

Here one has to mention the Danish school achievements. Besides the work of Bendsøe, one has to mention Olhoff [109], who has numerous applications of SIMP. Another important person in topology design is Sigmund, who contributed greatly to the general acceptance of SIMP.

His milestone works are: educational articles, checkerboard control, multiphysics applications, material model for SIMP. The pressure load solution calculated by Clausen and Sigmund [39] can be seen in figure 1.5.

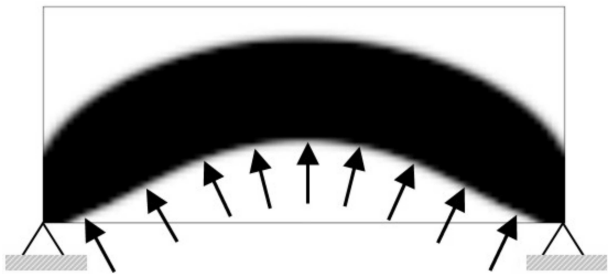

Figure 1.5: The pressure load solution by Clausen and Sigmund [39].

The SIMP method was also applied extensively by Rodrigues. Some of his major research topics have been: hierarchical topology optimization on macro and micro-scales [123], applications to bio-mechanics (e.g., bone tissue adaptation) [40] and optimization of piezoelectric properties [71].

Besides the numerical procedures mentioned above, Svanberg [145] in 1987 elaborated a math-

ematical programming subroutine – the method of moving asymptotes, which is one of the most frequently applied computational tools in topology optimization.

The method has been extensively used in multi-constrained problems of topology optimization, such as the minimization of the weight under local stress constraints (Duysinx and Bendsøe [54]), addressing symmetric and non-symmetric strength criteria also in conjunction with displacement constraints (Bruggi and Duysinx [42], Bruggi [25]).

As one can see there are many different fields in topology optimization. It is no surprise that all these branches can be found under the name of Kikuchi. His Research Lab at the University of Michigan, Ann Arbor, under his guidance, has "produced" a number of important researchers, who are currently leading scientists (Suzuki, Nishiwaki) in topology optimization. Together with Suzuki, the general theory of the homogenization method was elaborated (Suzuki and Kikuchi [144]). He and Gueddes [65] used the topology optimization for material design. Kikuchi and Nishiwaki et al. [106] extended the topology design to compliant design, and with Lee [82], the structural topology was used in electrical machinery. Having the leading scientist position at the Research Department of Toyota Motor Company, he successfully introduced topology optimization into the car industry [83].

1.2.3. Educational Publications and Codes

Given a geometric domain, topology optimization allows designing structural components by searching for the distribution of material that minimizes an objective function for a prescribed set of constraints [17]. Among the others, the design operated by distribution of isotropic material is widely adopted by academia and industry to sketch lightweight components. Assuming as unknown the density field that governs the elastic modulus of the material, an optimization problem can be formulated to minimize the work of the external loads at equilibrium (the so-called structural compliance), with constraints on the allowed amount of material (the available volume fraction), [16]. A strong penalization of the intermediate densities was especially conceived SIMP [15] to achieve optimal layouts made of void ("0" or "white") and solid material ("1" or "black"). The solutions for minimum compliance (i.e. minimum overall strain energy) usually consist of statically determinate truss-like structures that leverage the axial stiffness of struts and ties to get minimum deformability out of a limited amount of material.

Several papers have provided codes for solving the standard compliance topology optimization problem using the SIMP material interpolation scheme. The first educational code, known as top99, was developed by Sigmund in 2001 using MATLAB. It specifically deals with two-dimensional (2D) standard compliance minimization problems [135]. The code has a well-structured layout and employs a sequential implementation approach, making it highly compre-

hensible for students and newcomers in the field. It serves as an excellent educational resource.

Later, an 88-line MATLAB code called top88 was introduced to enhance the efficiency of the top99 code. The top88 code vectorizes the nested "for" loops present in top99 [7]. For three-dimensional (3D) topology optimization problems, several codes have been developed based on the standard 2D codes. One such code is top3D, a MATLAB code built upon the top88 code, specifically designed to handle 3D problems [88].

Ferrari and Sigmund utilized the latest MATLAB shortcuts and speed-up techniques to develop a new generation 99-line code, known as top99neo. This updated code is capable of efficiently handling medium to large-scale problems on a laptop, extending its functionality to three-dimensional (3D) optimization [58]. In addition to incorporating widely used update schemes like the OC (Optimality Criteria) method [14] and MMA (Method of Moving Asymptotes) [145], Zeng and Ma introduced their own 2D and 3D MATLAB codes, where those codes were built upon the top99 and top88 code structures and employed a novel gradient projection optimizer [163].

1.2.4. Multiscale Topology Optimization in Additive Manufacturing

Additive manufacturing (AM) is well-suited to bring layouts from concept to reality. It remarkably reduces limitations due to conventional manufacturing techniques, and is nowadays emerging as a competitive alternative to subtractive manufacturing in many fields of application. Indeed, 3D-printing allows for customizable products that can be effectively tailored to meet performance needs and requirements exploiting topology optimization. Reference is made to [87, 100, 115] for reviews on recent trends and achievements in their combined use.

Lattice structures are an example of complex features that can be easily manufactured through 3D-printing processes. They can be used to fabricate lightweight, robust and multi-functional infills that are generally preferred over solid interiors for parts of given shape, due to their intrinsic features, see e.g. [60]. Selective Laser Sintering (SLS) can take full advantage of porous infills of any given shape, whereas Fused Deposition Modelling (FDM) requires layouts with a limited overhang, unless printing supports are allowed, see e.g. [4, 152]. In the latter case, a plastic filament is melt and deposed layer-by-layer. For angles exceeding 45° degrees, supports are usually required, since the previous layers are not sufficient to build upon safely.

Optimal infill and external shape can be designed within the same numerical procedure by means of topology optimization. Among the available techniques to solve this design problem, multi-scale topology optimization represents an effective and efficient alternative, see the recent review in [157]. Assuming a separation of scales, numerical homogenization can be conveniently adopted to model the periodic microstructure of the infill (micro- or meso- level) by

using equivalent material properties at the macro-scale, see e.g. [65, 111, 142]. Asymptotic homogenization can be employed to compute the effective elastic properties of lattice material in terms of one or more design variables, i.e. one or more geometrical parameters governing a microstructure to be graded within the design domain, see e.g. [70, 162]. Alternatively, a procedure of inverse homogenization is needed to derive the shape of the microstructure corresponding to intermediate values of the unknown density field, see e.g. [5, 49]. It must be remarked that inverse homogenization was exploited in the early stages of topology optimization to circumvent the ill-posedness of the continuous problem that distributes a "void" and a solid phase only. Composites were allowed to occur at intermediate densities to this goal, see in particular [56] and [89].

In both cases, the achieved microstructures may be difficult to fabricate. When several patterns are generated, see e.g. [139], a peculiar issue is that different patches cannot be easily merged altogether. Loss of continuity or undesired geometrical singularities are likely to arise, unless this has been explicitly taken into account in the formulation, see e.g. [69]. Effective de-homogenization techniques have been proposed in the literature to overcome these problems, see in particular [64] and [159]. When grading honeycombs, see e.g. [156], or lattice and surface-based representations with given topology, see e.g. [110], issues to be faced include handling of anisotropy (especially in 3D), potential weakness of the microstructure (due to any abrupt change in section and sharp connections), features exhibiting critical overhang angles.

The adoption of self-supporting infills relieves manufacturing issues when fabricating the computed optimal layouts with 3d-printing techniques. However, there are many sources of uncertainties related to additive manufacturing. Among the others, the work in [113] analyzes the main factors that govern defect sensitivity in additive manufacturing, with special regard to the fabrication of architected porous microstructures. Macroscopic mechanical properties are sensitive to intrinsic characteristics of the base material, defects affecting geometrical features of the printed microstructure, process parameters, pre- and post-process treatments, to mention a few. A workflow is suggested to handle these issues, starting from the fabrication of prototypes, exploiting nondestructive techniques for defect detection and uncertainty quantification for an estimate of the impact of defects, see also [34], to end up with the formulation of problems of robust topology optimization.

The investigation presented in this contribution is limited to probabilistic loading, mainly focusing on the impact of this type of uncertainty, on the shape of the optimal layouts, and the load paths they provide. The implementation of the workflow presented in [113] would remarkably improve robustness of the achieved results.

1.3. Foundations of Probability in Topology Optimization

1.3.1. Overview of Topology Optimization Under Uncertainty

In engineering practice, uncertainties are significant factors that need to be considered. However, due to the complexity involved in stochastic calculations, designers often tend to use deterministic data during the design process. To address this limitation, stochastic programming theory and probabilistic notation have been introduced to provide a more rational approach. These methodologies account for the fact that the exact strength of a structure is not known and incorporate probabilistic inequalities as constraints. More importantly, they acknowledge the inherent lack of precision in the knowledge of applied loading on the structure. Loading, in particular, are best described using probabilistic methods, as their values are subject to various sources of uncertainty. Incorporating probabilistic notation into the design process allows for a more comprehensive analysis of the structure's performance under uncertain conditions, leading to designs that are more robust and reliable.

Until the end of the last century, there was a lack of publications on topology optimization that considered uncertainties. However, exceptions to this were often found in cases where multiple load or reliability constraints were used. While uncertainty was typically limited to loading conditions, some research has explored extensions to include support conditions and material properties. The existing probabilistic works can be classified into three distinct groups.

The first group assumes that the structure is built exactly as designed, with no uncertainty in its geometry. However, the load acting on the structure is uncertain. Within this group, the uncertainties in loading can be related to the magnitude, line of action, or point of application.

The second group focuses on scenarios where the load is deterministic, but the nodal locations used to define the structure's geometry are uncertain. The uncertainty in nodal locations introduces complexity to the problem, as it involves randomness in the inverse of the stiffness matrix. To simplify the analysis, it is assumed that the uncertainties in nodal locations are small compared to the length scale of the structural elements. This type of uncertainty model is particularly useful in representing fabrication errors.

The third group proposes a computational strategy for robust structural topology optimization in the presence of uncertainties with known second-order statistics. This strategy combines deterministic topology optimization techniques with a perturbation method to quantify uncertainties associated with structural stiffness, such as uncertain material properties or structure geometry. By using perturbation, the problem of topology optimization under uncertainty is transformed into an augmented deterministic topology optimization problem. This approach offers significant computational savings compared to simulation-based (Monte Carlo based) optimization

algorithms.

The overview and comparison of reliability procedures can be further explored in the review articles of Valdebenito and Schüeller [148], as well as Beck and de Santana Gomes [10]. Additionally, the foundational works of Ben Tal and Neminovski [11, 12] laid the groundwork for probability-based topology optimization nearly a decade before it gained popularity.

In the past twelve years, there has been a significant increase in the number of works addressing this topic. These publications are generally classified based on the specific object of topology optimization (e.g., trusses, continuum type structures, grids, plates), the numerical procedures employed (e.g., homogenization method, SIMP approach, evolutionary structural optimization (ESO) method, level-set based topology optimization method, meta-heuristic methods), and the sources of uncertainty (e.g., loading, geometry, stiffness, production tolerance).

One common approach among many of these studies is to reformulate uncertainties and create an alternate deterministic formulation. This involves replacing the uncertain objective function or constraints with their statistical averages. Alternatively, some approaches aim to minimize the influence of stochastic variability on the mean design by incorporating higher order statistics such as variance. These approaches are often referred to as robust design optimization (RDO).

In 1997, Sienz and Hinton [133] presented a paper describing a reliable and robust tool for structural shape optimization. This paper focused on the concept of reliability-based design optimization (RBDO), where the objective is to constrain or minimize (or maximize) a measure of the probability of failure, such as the reliability index. As well as other methods that utilize the upper bound theorems of stochastic optimization to provide an equivalent deterministic expression that bounds the probabilistic ones.

Maute and Frangopol [96] and Kim et al. [77] have also proposed a methodology for the design of micro-electro-mechanical systems (MEMS) using topology optimization, which takes into account stochastic loading, boundary conditions, and material properties. This methodology combines material-based topology optimization techniques for compliant mechanisms undergoing large displacements with design optimization under uncertainties using first-order reliability analysis methods. By incorporating these advancements, the authors aim to create robust designs that can account for the variability in loading, boundary conditions, and material properties typically encountered in MEMS applications. The robust optimal design procedure involves two main steps: a deterministic optimization phase for performance improvement, followed by a sensitivity analysis that considers uncertainties. During the deterministic optimization and sensitivity analysis, key performance indicators and critical uncertain variables are identified to define the gradient index.

The methodology of robust design, taking into consideration highly nonlinear structural behavior, is discussed by Schumacher and Olschinka [129]. This methodology focuses on addressing the challenges posed by highly nonlinear behavior in structural systems during the robust design process.

Califore and Dabbene [29] have utilized two standard theorems to find optimal solutions of uncertain convex optimization problems in the context of truss topology optimization mainly on incorporating uncertainty in both the load pattern and material characteristics. The first approach involves minimizing the expected value of the objective function with respect to uncertainty, commonly known as the average approach. In the second approach, known as the worst-case or min-max approach, the objective is to minimize the worst-case objective. This approach involves considering the most unfavorable scenario by selecting the design that performs the best under the worst possible conditions. Both of these approaches have been proven to yield exact and computationally efficient solution schemes, particularly when the uncertainty can be modeled in a simplified manner.

Dunning et al., [52, 53] present a robust structural topology optimization method that is both efficient and accurate. The main goal is to minimize expected compliance while considering uncertainty in both loading magnitude and applied direction. The authors assume that the uncertainties follow a normal distribution and are statistically independent. The approach can be comparable to solving a multiple load case problem, where load cases and weights are derived analytically to calculate expected compliance and sensitivities with precision and efficiency. To demonstrate the effectiveness of the proposed approach, the authors provide illustrative examples using a level-set-based topology optimization method.

1.3.2. Computational Techniques in Topology Optimization Under Uncertainty

The determination of the probability of failure through analytical means,is often impractical due to the reliance on numerical solutions like the finite element method to define the limit state function. This implicit form of the limit state function has given rise to several methods that enable numerical estimation of the probability of failure. One of the most well-known and straightforward methods is the Monte Carlo method. This method involves randomly selecting N implementations of random variables $(\theta_1, ..., \theta_N)$ based on their probability distributions. Subsequently, the limit function, g($\mathbf{x}$), is calculated for each value of $\theta \in \Theta$. The probability of failure is determined by the percentage of points where the value of the limit state function, g($\mathbf{x}$), is less than 0.

Designers aim to ensure the safety of structures, hence the probability of failure should be kept very low. In civil engineering, it is typically assumed that the probability of failure for a build-

ing structure should be in the order of 0.0001. To accurately determine such a low probability of failure, at least N=100,000 implementations of random variables need to be randomly generated.

However, the computation time required for evaluating such a large number of limit state function values using finite element analysis may be unfeasible. As a result, other methods have been developed to efficiently determine very low probabilities of failure.

One such method is the single loop approach, where an iterative procedure simultaneously updates the search for the minimum objective function and the search for the design point used for estimating the failure probability. This approach eliminates the need for nested reliability tasks by replacing reliability constraints with deterministic ones. The primary advantage of this method is its potential for high numerical efficiency, as it eliminates the need to determine the reliability index for each value of decision variables.

In the paper by Rashki et al. [122], a simulation-based method is presented for reliability-based design optimization. This method provides multi-level of solutions by performing just a single simulation run. The works of Lógó et al. [92, 93], Lógó [90, 91], and Pintér et al. [114] offer a suitable tool for conducting continuum type topology optimization procedures that account for uncertainty in applied loads. These publications employ a first-order approximation for compliance to address the presence of uncertainty. The consideration of robustness can also be found in Csébfalvi and Lógó [46].

1.4. Problem Statement

Adopting the conventional Solid Isotropic Model with Penalization to interpolate the elastic properties of the material with respect to its point-wise density, i.e. the minimization unknown, optimal layouts made of void and solid material are found. However, an improved overall performance can be achieved adopting alternative interpolation schemes with reduced penalization of the intermediate densities. Extended grey regions arise in the optimal layouts, which can be handled as infill zones of porous material to be further optimized. Alternatively, multi-scale topology optimization can be adopted to design both the macrostructure and the microstructure using a consistent material interpolation scheme. A wide range of lattices is achieved, and it is not straightforward to effectively combine their different shapes.

In this research, topology optimization approaches will be investigated that distribute a limited amount of material by grading throughout the domain the main geometrical features of a selected set of microstructures of assigned shape. Numerical homogenization will be employed to derive the relevant material schemes that interpolate the elastic properties of isotropic and

orthotropic lattices/microstructures both in 2D problems and 3D problems.

The material laws derived from homogenization of the selected graded microstructures will be used, at first, to replace SIMP in the conventional volume-constrained minimum compliance problem. This is equivalent to a minimum volume problem with constraints on the displacement fields in case of identical boundary conditions. The above problem will be investigated at first in the case of deterministic single loading. It will be investigated later the alternative loading and the multiple loading cases. The effect of probabilistic loads will be considered using Probabilistic Robust Design Optimization.

Optimal shapes will be investigated considering manufacturability when using AM techniques. Continuity among adjacent microstructures with different material density will be sought, as well as shapes that avoid undesired overhangs. The latter point is crucial for printers that use Fused Deposition Modelling (FDM) to melt a plastic filament while positioning it layer-by-layer. At 45 degrees, the newly printed layer is supported only by half of the previous layer, often still enough to build upon. For angles in excess of 45 degrees, some uneconomic support is generally required, at least for non-negligible “bridges”.

1.5. Software Utilized in Our Research

In my research, the analysis and simulations will be conducted using MATLAB, a powerful and versatile computational platform. The methodology will involve leveraging a fast and advanced code previously established by Ferrari and Sigmund [58] as a foundational base. This code, detailed in their paper, "A new generation 99 line Matlab code for compliance topology optimization and its extension to 3D," will be thoroughly adapted and expanded upon to align with the specific requirements and objectives of our study.

2 | Topology Optimization for Loads with Multiple Points of Application

Most of the contributions dealing with multi-scale design for maximum stiffness are based on the volume-constrained minimum compliance problem already mentioned. A displacement-constrained minimum volume formulation is ideally conceived to investigate lightweight design at the serviceability limit state. Indeed, displacement limits are prescribed for structural elements by technical codes, whereas the amount of material needed to fulfil these constraints is an outcome of the design problem.

When it comes to multiple load cases, a classical extension of the minimum compliance problem consists in using a weighted sum of the energy contribution pertaining to each one of the considered load cases. However, when local control of the deflection is requested under the effect of distributed loads, multiple forces and multiple load cases, the enforcement of a set of displacement constraints is required.

When the controlled displacement is that at single loaded point along the direction of the applied force, the work of the external load at equilibrium equals the scalar product of the controlled displacement and the applied force. In this case, the displacement-constrained minimum volume problem is equivalent to a classical volume-constrained minimum compliance problem. As discussed in [2], the same solution (up to a scaling) is expected to arise when considering either problem. This rationale does not apply when multiple loading or distributed loads are dealt with.

The proposed approach is concerned with the application of multiple local constraints to control the displacement field. A peculiarity of the proposed approach consists in the adoption of the augmented Lagrangian (AL) strategy to handle large sets of displacement constraints. Leveraging this framework, it is possible to control the deflection at each one of the loaded points when addressing distributed loads and (static) moving loads. Reference is also made to [130, 168] for examples of application of structural optimization on this topic.

2.1. Problem formulation and Implementation

When dealing with the considered multi-constrained problem of topology optimization, the finite element method is used to solve the governing equation, herein the linear elastic equilibrium. The element-wise constitutive properties of the material depend on the set of optimization unknowns through an interpolation law. A gradient-based minimization algorithm is used to iteratively update the unknowns in order to find the set that minimizes the objective function, accounting for the enforced constraints. In each step, a finite element analysis is performed to solve the elasticity problem with the current distribution of unknowns to compute updated information for the minimizer.

2.1.1. Detailed Problem Statement

Standard four-node displacement-based elements are used to get a discretization of a given design domain. A discrete design variable is assigned to each element. In the e-th of the n elements belonging to the mesh, $0 \leq \rho_e \leq 1$ is the so-called "density" of the material. Using SIMP [17, 165], the constitutive matrix $\boldsymbol{C}(\rho_e)$ reads:

$$\boldsymbol{C}(\rho_e) = \rho_e^p \boldsymbol{C_0} + \boldsymbol{C_{min}}, \tag{2.1}$$

where $\boldsymbol{C}_0$ is the plane stress constitutive matrix at full density, $\boldsymbol{C}_{min} = 10^{-9}\boldsymbol{C}_0$ stands for "void" and p is an interpolation parameter that penalizes intermediate densities, see in particular [58]. In the numerical simulations, p is increased from 3 to 9 during the optimization by means of the continuation approach used in the referenced work.

The statement of the displacement-constrained problem of minimum volume topology optimization, see [94], is:

$$\begin{cases} \min\limits_{0\leq\rho_e\leq 1} V = \sum\limits_{e=1}^{n} \rho_e V_{0,e} & \text{(2.2a)} \\ \text{subject to } \left(\sum\limits_{e=1}^{n} \rho_e^p \boldsymbol{K}_{0,e}\right) \boldsymbol{U}_j = \boldsymbol{F}_j, \quad \text{for } j = 1...l, & \text{(2.2b)} \\ \begin{cases} u_i \cdot \text{sign}(u_{lim,i}) \leq |u_{lim,i}|, \\ \text{sign}(u_i) = \text{sign}(u_{lim,i}) \end{cases} \quad \text{for } i = 1...m. & \text{(2.2c)} \end{cases}$$

In the above problem, the objective function shown in Eqn.(2.2a) is the volume of the structural element V. This may be computed through the sum over the contributions $\rho_e V_{0,e}$, being $V_{0,e}$ the

volume of the e-th element at full density, that is for $\rho_e = 1$.

Eqn.(2.2b) prescribes the static equilibrium of the structural element under multiple load cases. The global stiffness matrix is given by the element contributions accounting for the constitutive law of Eqn.(2.1). The element stiffness matrix reads $\rho_e^p \, \boldsymbol{K}_{0,e}$, where $\boldsymbol{K}_{0,e}$ refers to $\rho_e = 1$. For the j-th of the l load cases, $\boldsymbol{F}_j$ is the load vector, and $\boldsymbol{U}_j$ is the relevant nodal displacement vector.

The i-th of the m displacement components to be controlled is denoted by u_i. Eqn.(2.2c) enforces a prescribed limit $u_{lim,i}$. This quantity $u_{lim,i}$ stands for the maximum value that the i-th displacement component is allowed to undergo at the serviceability limit state. Assuming that u_i is an entry of $\boldsymbol{U}_j$, meaning that the i-th constraint refers to the j-th load case, one has:

$$u_i = \boldsymbol{L}_i^T \boldsymbol{U}_j, \tag{2.3}$$

where $\boldsymbol{L}_i$ is a vector made of zeros with the exception of the entry referring to the i-th displacement degree of freedom, which takes unitary value.

2.1.2. Numerical Implementation Details

In this section, an insight is given on the treatment of the density field to avoid well-known numerical instabilities while achieving crisp black/white layouts, and on the gradient-based approach used to handle the arising multi-constrained problem.

2.1.2.1. Filtering and Projection

A linear filter [20, 21] is implemented on the element variables ρ_e to avoid the arising of checkerboard patterns and mesh dependence. The original variables ρ_e are mapped to the new set of $\widetilde{\rho}_e$ as:

$$\begin{aligned} \widetilde{\rho}_e &= \tfrac{1}{\sum_n H_{es}} \textstyle\sum_n H_{es} \rho_s, \\ H_{es} &= \max\left(0\,,\, r_{min} - \mathrm{dist}(e,s)\right), \end{aligned} \tag{2.4}$$

where $\mathrm{dist}(e,s)$ is the distance between the centroid of the e-th and s-th element, and r_{min} is the filter radius, both entering the weight factor H_{es}. The filtered densities $\widetilde{\rho}_e$ are subsequently mapped to the set of physical densities $\widehat{\rho}_e$ to get crisp black/white solutions, see the projection proposed in [153]:

$$\widehat{\rho}_e = \frac{\tanh(\beta\eta\ ) + \tanh(\beta(\widetilde{\rho}_e - \eta))}{\tanh(\beta\eta\ ) + \tanh(\beta(1-\eta))}, \tag{2.5}$$

with $\eta = [0,1]$ and $\beta = [1,\infty]$. In the numerical simulations, $\eta = 0.5$, whereas β is smoothly increased during the run from 2 to 16, by means of the continuation approach used in [58]. The layout of the optimal solution is given using maps of $\widehat{\rho}_e$.

2.1.2.2. Solving Algorithm

The optimization problem in Eqn.(2.2) is solved via mathematical programming, using the Method of Moving Asymptotes (MMA) [145] as minimizer. Displacement constraints are treated following the augmented Lagrangian method implemented in [63]. Constraints are gathered in a modified version of the objective function such that the problem is turned into an unconstrained minimization. At the k-th AL step, this objective function reads:

$$V = V + \frac{1}{m}\sum_{i=1}^{m}\left(a_i^{(k)}\frac{|u_i|}{|u_{lim,i}|} + \frac{1}{2}b^{(k)}\left(\frac{u_i}{u_{lim,i}}\right)^2\right), \tag{2.6}$$

where $a_i^{(k)}$ is the i-th entry of the vector of the Lagrangian multiplier estimators and $b^{(k)} > 0$ is a penalty factor. MMA is used to find an approximate solution of the normalized function in Eqn.(2.6). This solution allows updating the current values of the estimators of the Lagrangian multipliers and the penalty factor for the subsequent AL step. In the numerical simulations, the number of MMA iterations per AL step has been set to 5. Further details on this approach will be given in Chapter 3, dealing with multiple displacement constraints within a multi-scale framework.

The overall process is repeated until convergence is met, i.e. the maximum difference in terms of the minimization unknowns between two subsequent steps is less than 10^{-3}.

2.1.2.3. Sensitivity Computation

The adjoint method is used to compute derivatives in order to provide the gradient-based minimizer with the sensitivity with respect to the design variables, see e.g. [16]. Accordingly, u_i of Eqn.(2.3) does not change when a zero function is added at the right hand side. Exploiting the discrete equilibrium in Eqn.(2.2b), denoting by $\boldsymbol{K}(\boldsymbol{\rho})$ the overall stiffness matrix depending on the vector gathering the element unknowns, one may write:

$$-\boldsymbol{\lambda}_i^T\left(\boldsymbol{K}(\boldsymbol{\rho})\boldsymbol{U}_j - \boldsymbol{F}_j\right), \tag{2.7}$$

where $\boldsymbol{\lambda}_i$ is any arbitrary but fixed vector. After re-arrangment of terms, the derivative of u_i with respect to the h-th entry of $\boldsymbol{\rho}$ may be computed as:

$$\frac{\partial u_i}{\partial \rho_h} = \left(\boldsymbol{L}_i^T - \boldsymbol{\lambda}_i^T \boldsymbol{K}(\boldsymbol{\rho})\right) \frac{\partial \boldsymbol{U}_j}{\partial \rho_h} - \lambda_i^T \frac{\partial \boldsymbol{K}(\boldsymbol{\rho})}{\partial \rho_h} \boldsymbol{U}_j, \tag{2.8}$$

that can be in turn written as:

$$\frac{\partial u_i}{\partial \rho_h} = -\lambda_i^T \frac{\partial \boldsymbol{K}(\boldsymbol{\rho})}{\partial \rho_h} \boldsymbol{U}_j. \tag{2.9}$$

In the above expression, $\boldsymbol{\lambda}_i$ satisfies the adjoint equation:

$$\boldsymbol{K}(\boldsymbol{\rho})\boldsymbol{\lambda}_i = \left(\frac{\partial u_i}{\partial \boldsymbol{U}_j}\right)^T = \boldsymbol{L}_i. \tag{2.10}$$

Eqn.(2.9) can be evaluated recalling that the derivative of the e-th element stiffness matrix with respect to ρ_h is equal to $p\rho_e^{p-1}\boldsymbol{K}_{0,e}$, being $\boldsymbol{K}_{0,e}$ the element stiffness matrix at full density. This sensitivity is null if $e \neq h$.

The derivatives with respect to the filtered variables $\widetilde{\rho}_e$ and the physical ones $\widehat{\rho}_e$ can be evaluated by applying the chain rule to Eqn.(2.4) and Eqn.(2.5), respectively. At each iteration in the process, only one matrix inverse must be computed to evaluate constraints and their sensitivities. This is because the linear systems in Eqn.(2.2b) and Eqn.(2.10) share the same coefficient matrix $\boldsymbol{K}(\boldsymbol{\rho})$. It is also remarked that this framework is ideally conceived for a straightforward implementation within commercial finite element codes, exploiting their application programming interfaces, see e.g. [24].

2.2. Case Studies and Numerical Simulations

Numerical simulations considering the optimal design under displacement constraints are presented in this section, dealing with unitary fixed point forces, uniformly distributed loads, and forces with multiple points of application. The latter are referred to as moving point forces in the discussion that follows.

In all the examples, the controlled displacements u_i are those read at the m loaded nodes in the direction of the acting force. The limit $u_{lim,i}$ is defined either as $\alpha u_{0,i}$, i.e. α times the value found at the same point in case of full material beam $u_{0,i}$, or as $\alpha \max_m u_{0,i}$. In the former case, the goal is reproducing the stiffness provided by a full material beam, with the scaling given by α. In the latter case, the bound of the displacement is the same for all the controlled points, as conventionally done in the assessment of structures at the serviceability limit state. In the numerical simulations that follow $\alpha = 1.50$.

Rectangular domain analysed next have height equal to L and filter radius r_{min}=$L/10$. All the layouts presented next are respectful of all the enforced local constraints. Each solution is endowed with the value of the volume fraction of the material at convergence $v_f = \frac{V}{V_0}$, that is the ratio of the last value of the objective function in Eqn.(2.2a) to the volume of a full material beam.

2.2.1. Cantilever Beam

The first numerical investigation refers to a 3L $\times$ L, cantilever beam that is fully clamped at the left side, where L = 100 unit length. A mesh of 300 $\times$ 100 four-node elements is used.

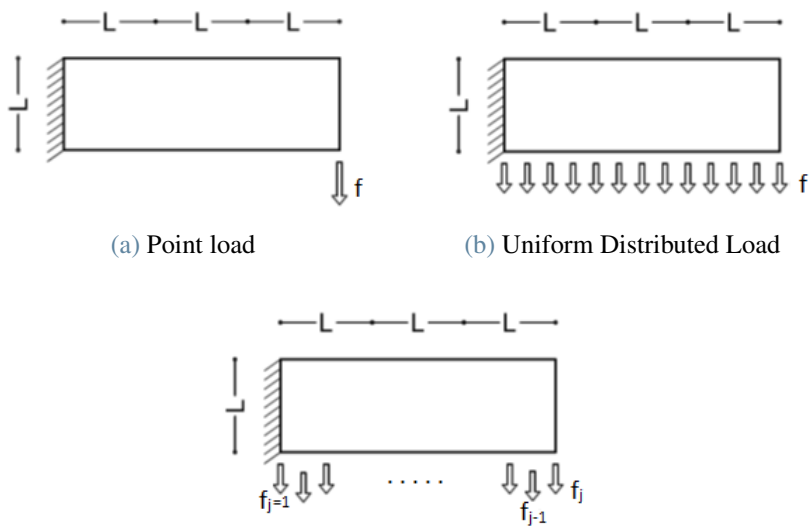

(a) Point load (b) Uniform Distributed Load

(c) Moving Load

Figure 2.1: Cantilever beam: Initial problem

At first, it is assumed that the specimen is acted upon by a vertical force located at the bottom right corner of the rectangular domain. The formulation in Eqn.(2.2) is implemented considering one load case ($l = 1$) and controlling the vertical component of the displacement read at the loaded point, that is the lower corner of the tip ($m = 1$). The achieved design is the truss-like structure shown in Figure 2.2. The volume fraction is $v_f = 0.50$. This means that only half of the material making a full material beam is needed if an increase by half in the deflection is allowed.

Figure 2.2: Cantilever beam: optimal design considering a force applied at the tip ($v_f = 0.50$).

A second investigation is performed considering a uniformly distributed load acting all over the lower side of the rectangular domain. A set of constraints is enforced in the formulation of Eqn.(2.2c) to control the vertical displacement at each one of the loaded nodes within the same load case ($l = 1$, $m = 300$). The optimal layouts that are found by enforcing the same u_{lim} throughout the span ($\alpha \max_m u_{0,i}$) and by implementing the varying u_{lim} ($\alpha u_{0,i}$), are shown in the left and right picture of Figure 2.3, respectively.

Figure 2.3: Cantilever beam: optimal design considering a uniformly distributed load, for the same u_{lim} all over the span (left, $v_f = 0.40$), and varying u_{lim} to approximate the deflection of a full material beam (right, $v_f = 0.50$).

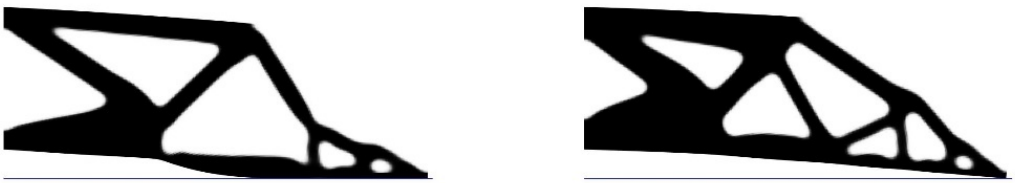

Figure 2.4: Cantilever beam: deformed shapes of the layouts achieved considering a uniformly distributed load: same u_{lim} all over the span (left), and varying u_{lim} to approximate the deflection of a full material beam (right).

The relevant deformed shapes are sketched in Figure 2.4, along with a horizontal line representing the quantity $\alpha \max_m u_{0,i}$. In the latter case, the design is heavier than in the former ($v_f = 0.50$ vs. 0.40) due to the stricter displacement constraints. Indeed, almost one half of the bottom side of the domain lies along the line representing the quantity $\alpha \max_m u_{0,i}$ in the former case, whereas in the latter such a deflection is allowed at the tip only.

Two additional simulations are set to investigate the difference between displacement-constrained minimum volume optimization and volume-constrained minimum compliance design. Minimum compliance layouts are found using as input the volume fractions found in output for the minimum volume layouts of Figure 2.3. The optimal layouts (in their deformed configuration) for $v_f = 0.40$ and $v_f = 0.50$ are represented in the left and right picture of Figure 2.5, respectively. In both pictures, the horizontal line representing the quantity $\alpha \max_m u_{0,i}$ already used in Figure 2.4 is reported to check the deformability. The achieved minimum compliance layouts have some similarity with the minimum volume design approximating the deflection of a full material beam, see Figure 2.3 (right). However, as expected, neither of them is stiff as the solutions found by enforcing a local control of the displacement field.

Figure 2.5: Cantilever beam: deformed shapes of the minimum compliance layouts achieved considering a uniformly distributed load and prescribing: $\mathrm{v}_f = 0.40$ (left), and $\mathrm{v}_f = 0.50$ (right).

Finally, the optimal design in case of a point force moving along the lower side of the geometrical domain of the cantilever is considered. This may be simply implemented in Eqn.(2.2) by defining a load case for each one of the nodes belong to the load path of the point force ($l = 300$), and by controlling the relevant displacement at the loaded node ($m = 300$). Along the lines of the simulations performed in case of uniformly distributed load, two optimization strategies have been tested. The picture on the left in Figure 2.6 is the layout achieved by enforcing the same displacement limit all over the load cases ($\alpha \max_m u_{0,i}$). The optimal design has the same volume fraction of the optimal design found in the case of a specimen loaded by a vertical force at the tip. However, it has less and thicker members than the layout in Figure 2.2. Dealing with the moving force, a subsequent optimization is performed using the varying u_{lim} that is aimed at reproducing the deflection of a full material beam ($\alpha u_{0,i}$). A much heavier design arises in this case to fulfil the stricter deflection constraints, see the picture on the right in Figure 2.6.

Figure 2.6: Cantilever beam: optimal design considering a moving vertical force, for the same u_{lim} throughout the span (left, v_f =0.50), and varying u_{lim} to approximate the deflection of a full material beam (right, v_f = 0.58).

2.2.2. Single Span Beam

In this section the displacement-constrained minimum volume design is investigated dealing with single span beams occupying a rectangular domain with size 6L × L, where L = 100 unit length. A mesh of 600 × 100 four-node plane elements is used. Forces are applied at the lower side of the rectangular domain.

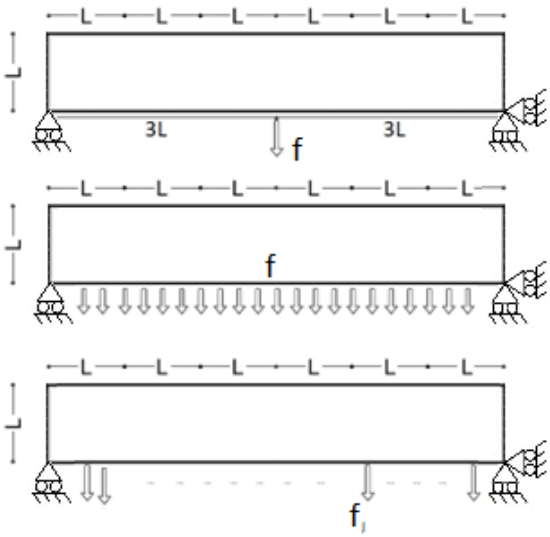

Figure 2.7: Single Span Beam: Initial problems

At first, the case of simply supported beam is considered. Figure 2.8 gathers pictures representing the optimal layouts found when considering a force applied at midspan (top), a uniformly distributed load (center), and a moving vertical force (bottom). The last two layouts have been found by enforcing the same displacement limit all over the loaded points ($\alpha \max_m u_{0,i}$). The optimal design achieved in case of uniformly distributed load takes full advantage of the symmetry of the load and of the low value of the shear force around midspan. The solution found

for the moving force is a more branched variation of that found considering a force applied at midspan. Indeed, this is the location of the point force for which the deflection is the largest in a beam with uniform cross section. The achieved design costs a very minor increase in terms of volume fraction ($v_f = 0.52$ vs. 0.50).

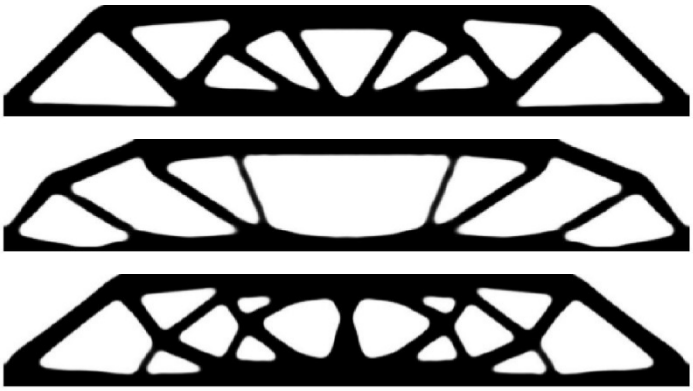

Figure 2.8: Simply supported beam: optimal design considering a force applied at midspan (top, $v_f = 0.50$), a uniformly distributed load (center, $v_f = 0.37$), and a moving vertical force (bottom, $v_f = 0.52$).

Then, the case of a two hinged beam is analysed, considering the same loads and optimization problems already implemented for the simply supported beam. The achieved results are given in Figure 2.9. The optimal layout found for the uniformly distributed load is an efficient arch-like structure with inclined ties, a widely implemented solution in bridge design. In the solution found considering a force applied at midspan, the point load hangs from a central stiff region that is supported by two inclined struts. This layout cannot accommodate effectively forces with different point of applications. Indeed, the optimal solution found for the moving point force is a much heavier structure: the arch already exploited in the design for the uniformly distributed load is here endowed with a strut-and-tie sub-structure that supports the point force all over its path.

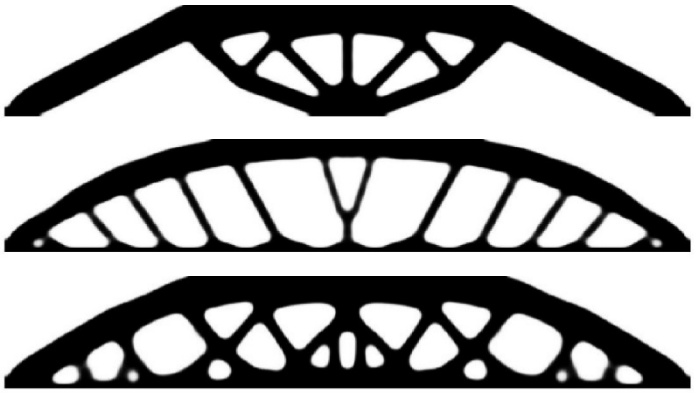

Figure 2.9: Hinged beam: optimal design considering a force applied at midspan (top, $v_f = 0.42$), a uniformly distributed load (center, $v_f = 0.36$), and a moving vertical force (bottom, $v_f = 0.53$).

2.2.3. Two-Span Beam

A two-span beam is considered adopting the same mesh used in the previous example. An additional support is added in the middle of the lower side. At first the optimal design is dealt with considering a uniformly distributed load applied at the lower edge all over the two spans ($l = 1$ and $m = 598$). The same displacement limit ($\alpha \max_m u_{0,i}$) is enforced at all the loaded points. The optimal design is represented in the top picture of Figure 2.11. The arm between the upper and the lower chord of the structure is in good agreement with the diagram of the bending moment of a two-span beam made of full material. To maximize the deflection, an alternative load scenario could be conveniently considered. The optimal design shown in the bottom picture of Figure 2.11 concerns the implementation of two load cases. The uniformly distributed load acts in one span at a time, i.e. $l = 2$ and $m = 598$, with half of the constraints referring to the points loaded in the left span (first load case) and half to the points loaded in the right span (second load case). In each of the two spans the design is quite similar to that found for the simply supported beam, see Figure 2.8 (center).

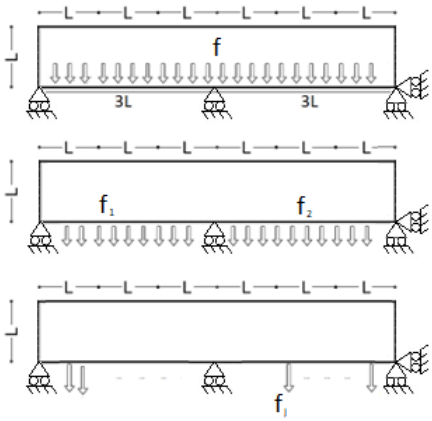

Figure 2.10: Two Span Beam: Initial Problems

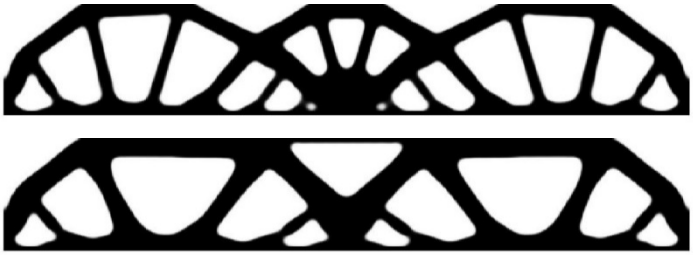

Figure 2.11: Two-span beam: optimal design considering a uniformly distributed load acting on both spans simultaneously (top, $v_f = 0.46$), and acting in one span at a time (bottom, $v_f = 0.50$).

The last set of investigations refers to a moving point force whose path is the lower side of the rectangular domain. This is implemented in Eqn.(2.2) by defining a load case for each one of the nodes belonging to the path followed by the point force ($l = 598$) and by controlling the relevant displacement at the loaded node ($m = 598$). As done in Section 2.2.1, two optimization strategies have been tested. In Figure 2.12 the optimal layout achieved by enforcing the same displacement limit all over the load cases ($\alpha \max_m u_{0,i}$) is represented. In Figure 2.13 the optimal design achieved by enforcing the varying u_{lim} that is aimed at reproducing the deflection of a full material beam ($\alpha u_{0,i}$) is given. In both figures a map of the vertical displacements computed at the varying loaded point is provided, along with a plot of the fixed/ varying u_{lim}. Although the optimal layouts are quite similar in terms of topology and volume fraction ($v_f = 0.62$ vs. 0.65), the relevant displacement plots are quite different. While most of the deck undergoes the maximum allowed displacement in the former case, a smoother variation is found, as expected, in the latter.

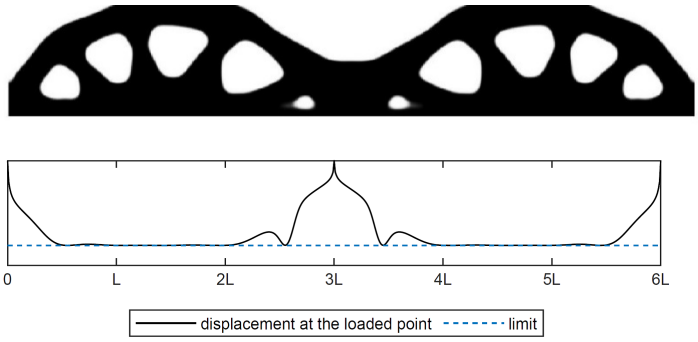

Figure 2.12: Two-span beam: design considering a moving vertical force and the same u_{lim} throughout the spans ($v_f = 0.62$): optimal layout and displacement computed at the varying loaded point.

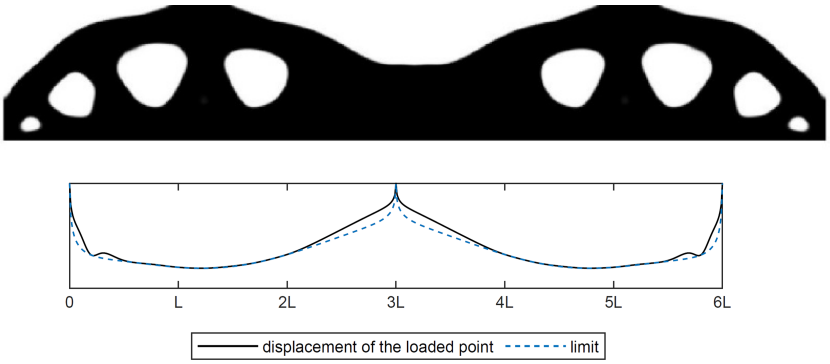

Figure 2.13: Two-span beam: design considering a moving vertical force and a varying u_{lim} aimed at approximating the deflection of a full material beam ($v_f = 0.65$): optimal layout and displacement computed at the varying loaded point.

2.3. Summary and Conclusions

A topology optimization formulation based on the distribution of isotropic material has been worked for identifying structures of minimal volume while adhering to multiple displacement constraints. This problem accommodates fixed points or distributed loads, incorporating loads with various points of application, in which a static moving force can be applied, with a local enforcement to control the relevant displacement.

To address the optimization subject to multiple displacement constraints, a modified augmented Lagrangian approach with sequential convex programming was implemented. This approach effectively manages the complexities inherent in multi-constrained problems, ensuring efficient solution for achieving optimal designs within the large amount of displacement constraints.

Numerical simulations have demonstrated optimal designs characterized by multiple displacement constraints. where two methodologies have been examined for the formulation of deflection enforcement: adhering to conventional practices at the serviceability limit state, wherein a uniform upper bound for displacement is applied across all controlled points, and employing a variable limit that mimic the stiffness exhibited by a full material beam.

Optimal solutions for moving loads have been compared to classical solutions for fixed loads, both point forces and distributed loads. In a few examples, the optimal topology for moving loads was found to be a slightly heavier variation of the topology obtained for a single force applied where the maximum deflection was expected (see results concerning the cantilever beam and the simply supported beam). However, alternative layouts may arise to provide the required support along the entire load path (see results on the two hinged beam). It is also remarked that the strategy adopted to enforce deflection constraints remarkably affects, as expected, the displacement read under the moving force (see results on the two-span beam).

3 | Lightweight Additive Design: Graded Porosity with Displacement Constraints

In this chapter, we explore the capabilities of Additive Manufacturing (AM) in transforming conceptual designs into tangible objects, significantly overcoming the constraints associated with traditional manufacturing techniques. 3D printing, in particular, enables the precise fabrication of products tailored to specific performance requirements through the application of topology optimization.

Porous structures exemplify the advanced features achievable via 3D printing, serving as a key model for the production of lightweight, robust, and multifunctional infills. These structures are often preferred over their solid counterparts for components with predetermined geometries. Among the techniques available for addressing the optimal design of infill and external shapes, multi-scale topology optimization presents an effective and efficient alternative within the same computational framework.

Building on these principles, the chapter introduces a multi-scale topology optimization approach for designing lightweight components that adhere to specified load and displacement limits. This method utilizes hexagonal close-packed arrangements of circular or spherical holes to define 2D or 3D isotropic or transversely isotropic microstructures, where the macroscopic elastic properties depend on the cavity radius, reflecting the material's density. An interpolation law is employed to manage multi-material structures, incorporating both solid and graded materials within a specified density range. This approach also indicates the position of the boundaries of the component and the potential internal configurations of holes facilitating the creation of optimal infill.

Numerical examples are presented to demonstrate the application of this method to both two-dimensional and three-dimensional problems under various types of loads. This discussion aims to highlight the distinctive features and specific properties of the optimized solutions, particularly focusing on coated structures. The feasibility of fabricating these porous layouts using additive manufacturing techniques is also discussed, underscoring the practical implications and potential of this approach in modern manufacturing.

3.1. Preliminaries

Homogenization combines the properties of each discrete component that constitutes the composite material in order to extract its equivalent properties. By means of the homogenization theory the equivalent properties of an isolated from the composite's microstructure unit cell are obtained. The property of the composite material intended to be homogenized is the elasticity tensor of the non-homogeneous unit cell.

Asymptotic homogenization can be employed to compute the effective elastic properties of lattice material in terms of one or more design variables, i.e. one or more geometrical parameters governing a microstructure to be graded within the design domain. Hexagonal close-packed arrangements [140] of circular/spherical holes allow defining 2D/3D isotropic/transversely isotropic microstructures whose homogenized elastic properties can be graded by varying the radius of the cavities. Due to the moderate anisotropy of the three-dimensional porous material, the macroscopic elastic properties of both porous phases can be derived in terms of the bulk modulus and the shear one.

Alternatively, a procedure of inverse homogenization is needed to derive the shape of the microstructure corresponding to intermediate values of the unknown density field.

As investigated e.g. in [48], a hexagonal arrangement of circular holes gives rise to a 2D isotropic porous microstructure, see Figure 3.1. This geometry is quite similar to that of the extreme periodic microstructure found in [134] when using inverse homogenization to maximize the bulk modulus with isotropy constraint, see also [149]. Similarities arise also with respect to some of the base cells presented in [147], where the design for optimized strength against initiation of microscopic buckling is dealt with considering different load cases. It must be also remarked that rounded holes are effective in preventing the arising of undesired stress concentration, see in particular the numerical investigations on material design reported in [41] and [43].

Given a Cartesian reference frame $Oz_1z_2z_3$, a three-dimensional body made of linear elastic isotropic material with Young's modulus E_0 and Poisson's ratio ν_0 occupies the region Ω. Denoting by σ_{ij} and ε_{ij} the components of the stress tensor and of the strain tensor, respectively, the constitutive relation reads:

$$\sigma_{ij} = (K_0 - 2G_0/3)\varepsilon_{kk}\delta_{ij} + 2G_0\varepsilon_{ij}, \tag{3.1}$$

where

$$K_0 = \frac{E_0}{3(1-2\nu_0)}, \; G_0 = \frac{E_0}{2(1+\nu_0)} \tag{3.2}$$

are the three-dimensional bulk modulus and the shear modulus of the material, respectively.

Assuming plane stress elasticity, the stress-strain relation becomes:

$$\sigma_{ij} = (K_0 - G_0)\varepsilon_{kk}\delta_{ij} + 2G_0\varepsilon_{ij}, \tag{3.3}$$

where

$$K_0 = \frac{E_0}{2(1-\nu_0)} \tag{3.4}$$

is the two-dimensional bulk modulus of the material and G_0 is the shear modulus of Eqn.(3.2).

In a density-based approach of topology optimization, $0 \leq \rho \leq 1$ is a variable that governs the elastic properties of the material in Ω through the so-called Solid Isotropic Material with Penalization (SIMP) [15, 17]. One may write:

$$K(\rho) = K_{min} + \rho^p(K_0 - K_{min}), \quad G(\rho) = G_{min} + \rho^p(G_0 - G_{min}), \tag{3.5}$$

where $p > 1$ (usually $p = 3$) is intended to penalize the intermediate range of the density, K_0 is either the three-dimensional bulk modulus of the material or its plane-stress two-dimensional counterpart, depending on the problem, and G_0 is the shear modulus. K_{min} and G_{min} are small nonzero values to be used when computing the solution of the elastic equilibrium of the body via finite element analyses (typically 10^{-9} times the values at full material).

3.1.1. Material Law

Andreassen [6] provided an efficient way to determine effective macroscopic properties, such as the elasticity tensorusing a self-contained Matlab implementation which computes the effective elasticity tensor of a two material composite, where one material could be void. Andreassen [6] provided self-contained matlab code base on numerical homogenization method for 3D cellular materials that shows how the homogenized constitutive matrix is computed by a voxel model with one material to be void and another material to be solid.

3.1.1.1. A Porous Micro-structure with Graded Circular Holes

The material density of a two-dimensional graded porous microstructure featuring an hexagonal arrangement of circular holes can be computed as $\rho_g = 1 - |Y_v|/|Y|$, where $|Y|$ is the volume of the base cell with dimensions $l_{y1} = d, l_{y2} = \sqrt{3}d$ and $|Y_v|$ is the volume of the inner circular-like

voids.

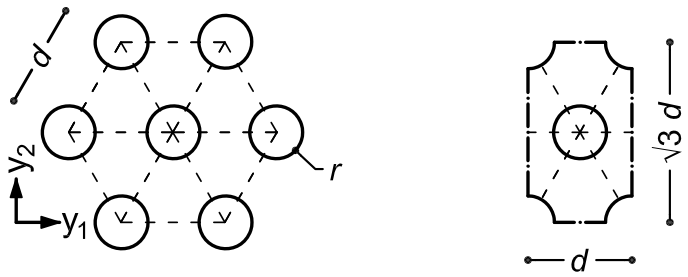

(a) With prescribed reference dimension d and variable radius r

(b) A single base cell

Figure 3.1: 2D version of the porous microstructure hexagonal arrangement of circular holes

The density depends upon the radius of the circular holes as:

$$\rho_g = 1 - \frac{2\pi r^2}{\sqrt{3}d^2} \text{ for } 0 \leq r \leq r_{max}, \text{ with } r_{max} = \frac{d-t}{2}, \tag{3.6}$$

where r_{max} is the maximum radius as a function of the reference dimension of the microstructure, d, and of the minimum thickness of the material between two adjacent holes, t. For $t = 0$, the density of the material would be that of a close-packing of circular holes, i.e. $\rho_{g,min} = 0.093$, see [140].

Polylactic acid (PLA) is assumed in this study as the reference material, being $E_0 = 3.6\,\text{GPa}$ and $\nu_0 = 1/3$. The dependence of the stress-strain matrix on the material density may be evaluated by performing numerical homogenization on the base cell represented in Figure 3.1b. The pixel-based method implemented in [6] is used. Homogenization is run using a regular mesh with pixel dimension $l_{pix} = d/100$, for $0 \leq r < r_{max}$, assuming $t = d/50$ (the material disintegrates for $t = 0$). The achieved results are fitted using a fifth degree polynomial, for which zero stiffness is additionally enforced at $\rho_g = 0$. The material law reads:

$$\begin{aligned} K(\rho_g) &= K_{min} + \left(1.0483\rho_g^5 - 1.1636\rho_g^4 + 0.3993\rho_g^3 + 0.4950\rho_g^2 + 0.2210\rho_g\right)(K_0 - K_{min}), \\ G(\rho_g) &= G_{min} + \left(3.5149\rho_g^5 - 7.6208\rho_g^4 + 5.7678\rho_g^3 - 0.7083\rho_g^2 + 0.0465\rho_g\right)(G_0 - G_{min}), \end{aligned} \tag{3.7}$$

for $0 \leq \rho_g \leq 1$, where K_0 and G_0 are the full material values introduced in Section 3.1 for plane stress, namely K_0 of Eqn.(3.4) and G_0 of Eqn.(3.2), whereas K_{min} and G_{min} are those of Eqn.(3.5).

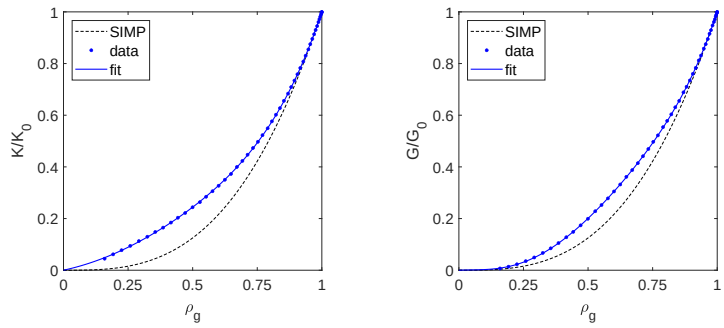

(a) Two-dimensional bulk modulus $K(\rho_g)/K_0$

(b) Shear modulus $G(\rho_g)/G_0$

Figure 3.2: 2D version of the porous microstructure: interpolation laws fitting results from numerical homogenization, as compared to the conventional SIMP

In Figure 3.2, the fitting interpolation laws are compared to the conventional SIMP to point out that the porous microstructure is much stiffer at low and intermediate densities than the conventional penalization with $p = 3$. This applies especially for the two-dimensional bulk modulus.

3.1.1.2. A Porous Micro-structure with Graded Spherical Holes

In geometry, close-packing of equal spheres is a dense arrangement of congruent spheres in an infinite, regular arrangement [140]. There are two simple periodic layouts that achieve the highest average density, namely the Face-Centered Cubic (FCC), also called Cubic Close-Packed, and the Hexagonal Close-Packed (HCP) .

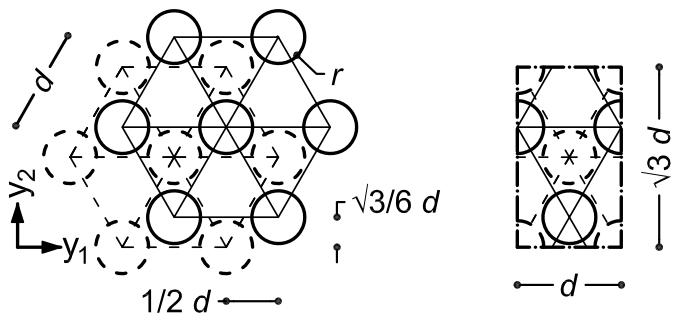

(a) With prescribed reference dimension d and variable radius r

(b) Plan view of a single base cell

Figure 3.3: 3D version of the porous microstructure: superposition of hexagonal layers of spherical holes in the hexagonal close-packed (HCP) arrangement

In Figure 3.3, a sequence of two hexagonal layers of spherical holes in the so-called hexagonal close-packed arrangement is represented. The layer A has the same arrangement already used for circular holes in the 2D porous microstructure. It is represented using dotted lines. The layer B is found by translating the layer A along a vector $(1/2\,d, \sqrt{3}/6\,d, \sqrt{6}/3\,d)$, as depicted using continuous lines in the picture. A six-fold rotational symmetry about the y_3-axis, perpendicular to the hexagonal layers, is observed in the microstructure. Hence, the periodic sequence AB gives rise to a transversally isotropic porous microstructure with axis y_3. It must be remarked that the HCP arrangement achieves the highest average density in the close-packing of equal spheres, herein spherical holes.

The material density of the three-dimensional graded porous microstructure depends upon the radius of the spherical holes as:

$$\rho_g = 1 - \frac{8\pi r^3}{3\sqrt{2}d^3} \text{ for } 0 \leq r \leq r_{max}, \text{ with } r_{max} = \frac{d-t}{2}, \tag{3.8}$$

where r_{max}, d, and t have been already defined in Section 3.1.1.1. For $t = 0$, the minimum density of the material would be that of a close packing of spherical holes i.e. $\rho_{g,min} = 0.259$.

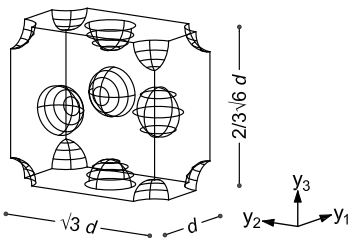

Figure 3.4: 3D version of the porous microstructure: three dimensional view of a single base cell

For transversally isotropic material the stress-strain relationship is a function of five independent parameters. Its dependence on ρ_g can be evaluated by applying the voxel-based homogenization approach presented in [50] to the base cell of Figure 3.4. Homogenization is run assuming Polylactic acid and a regular mesh with voxel dimension $l_{vox} = d/50$ for $0 \leq r \leq r_{max}$, see Eqn.(3.8), with the same minimum thickness already used for the 2D base cell. According to Appendix A.1, the 3D porous microstructure is affected by minor anisotropy. As a simplification, isotropic material modelling will be used in the following.

Along the lines of the procedure followed in the two-dimensional framework, the results achieved through homogenization are fitted using a fifth degree polynomial, for which zero stiffness is

additionally enforced at $\rho_g = 0$. The material law reads:

$$\begin{aligned} K(\rho_g) &= K_{min} + \left(1.7267\rho_g^5 - 2.3570\rho_g^4 + 0.6246\rho_g^3 + 0.9517\rho_g^2 + 0.0540\rho_g\right)(K_0 - K_{min}), \\ G(\rho_g) &= G_{min} + \left(0.7420\rho_g^5 - 1.2437\rho_g^4 + 0.2233\rho_g^3 + 1.2634\rho_g^2 + 0.0151\rho_g\right)(G_0 - G_{min}), \end{aligned} \tag{3.9}$$

for $0 \leq \rho_g \leq 1$, the fitting interpolation laws $K(\rho_g)$ and $G(\rho_g)$ are represented in Figure 3.5, along with the conventional SIMP for $p = 3$. The main consideration set out with regard to the two-dimensional results of Figure 3.2 applies here as well. With respect to SIMP with $p = 3$, the increase in terms of shear modulus is even bigger than that in terms of bulk modulus.

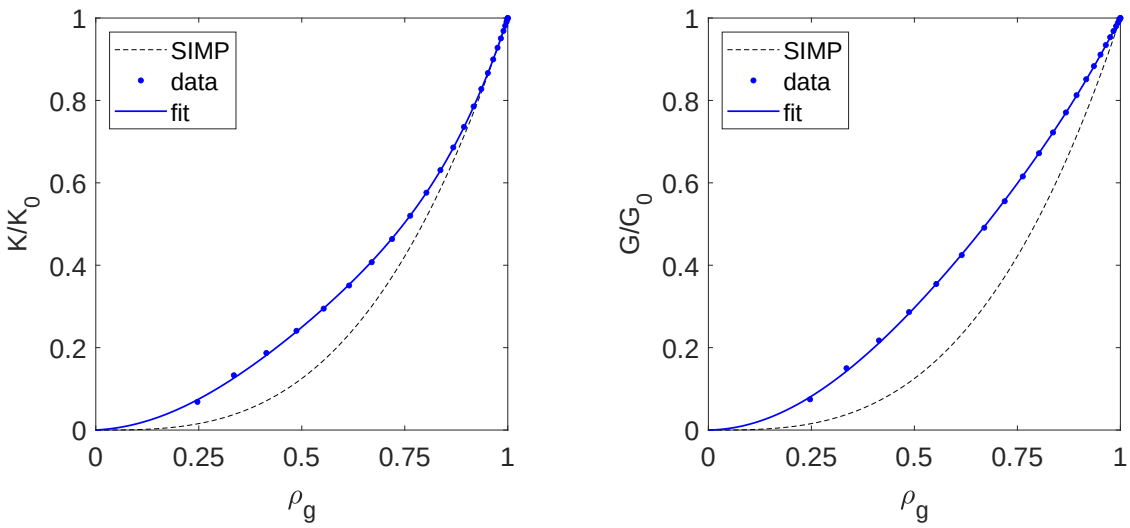

(a) Three-dimensional bulk modulus $K(\rho_g)/K_0$ (b) Three-dimensional shear modulus $G(\rho_g)/G_0$

Figure 3.5: 3D version of the porous microstructure: interpolation laws fitting results from numerical homogenization, as compared to the conventional SIMP

3.1.2. A Two-Phase Material Model with Void

A two-phase interpolation law for the isotropic elastic constants is introduced to allow for the distribution of full material and void (see Section 3.1), along with a fraction of porous microstructure with graded circular/spherical holes (see Sections 3.1.1.1/3.1.1.2). It reads:

$$\begin{aligned} K(\rho, \rho_g) &= \rho^p K_0 + (1 - \rho^p) K(\rho_g), \\ G(\rho, \rho_g) &= \rho^p G_0 + (1 - \rho^p) G(\rho_g), \end{aligned} \tag{3.10}$$

for $0 \leq \rho, \rho_g \leq 1$, where symbols are those already used in Eqns.(3.5), (3.7) and (3.9). For

$\rho = 1$, whatever the value of ρ_g, the bulk modulus and the shear one are those of full material, i.e. K_0 and G_0 respectively. For $\rho = \rho_g = 0$, only the terms K_{min} and G_{min} are nonzero, i.e. the fictitious stiffness of the void is found, see Eqns.(3.7) and (3.9). For $\rho = 0$ and $\rho_g \neq 0$ a porous microstructure may arise according to the adopted interpolation, either Eqn.(3.7) or Eqn.(3.9).

In the above equations, the penalization of ρ is especially conceived to steer the design towards its limit values, i.e. $\rho = 1$ (full material) or $\rho = 0$ (void or porous microstructure graded by ρ_g). Indeed, increasing ρ on a certain place automatically reduces the weight of the complementary phase, thus promoting 0-1 design. Formulations to distribute two distinct materials and void (three phases) using this concept were introduced in [136], as reviewed by [143].

To enhance the effect of such an approach, p is smoothly increased during the simulations from 3 to 6 through a continuation approach, see [58].

3.2. Design for Minimum Weight Under Displacement Constraints

3.2.1. Formulation

A finite element discretization of a given design domain is operated, using four-node and eight-node displacement-based elements in two and three dimensions, respectively. Two sets of element-wise design variables are considered to implement the material law of Eqn.(3.10). In the e-th of the n elements of the mesh, ρ_e and $\rho_{g,e}$ are the discrete counterpart of the variables ρ and ρ_g, respectively.

A problem for the design of a topology of minimum weight under displacement constraints can be stated as:

$$\begin{cases} \min\limits_{\substack{0\leq\rho_e\leq 1 \\ 0\leq\rho_{g,e}\leq\rho_{g,max}}} \quad V = \sum\limits_{e=1}^{n} \Big(\rho_e + (1-\rho_e)\rho_{g,e}\Big) V_{0,e} & \text{(3.11a)} \\ \text{s.t. } \mathbf{K}(\boldsymbol{\rho},\boldsymbol{\rho_g})\,\mathbf{U}_j = \mathbf{F}_j, \quad \text{for } \; j = 1...l, & \text{(3.11b)} \\ \begin{cases} u_i \cdot \text{sign}(u_{lim,i}) \leq |u_{lim,i}|, \quad \text{for } \; i = 1...m \\ \text{sign}(u_i) = \text{sign}(u_{lim,i}) \end{cases} & \text{(3.11c)} \\ \sum\limits_{e=1}^{n} (1-\rho_e)\rho_{g,e} V_{0,e} \geq f_g \sum\limits_{e=1}^{n} V_{0,e}. & \text{(3.11d)} \end{cases}$$

In the above statement, the objective function is the weight of the component, which is computed through the sum of the element contributions $(\rho_e + (1-\rho_e)\rho_{g,e})\,V_{0,e}$, being $V_{0,e}$ the volume of the e-th element for $\rho_e = 1$.

Eqn.(3.11b) prescribes the discrete elastic equilibrium. The global stiffness matrix $\mathbf{K}(\boldsymbol{\rho},\boldsymbol{\rho_g})$ is computed by assembling the element contributions that account for the constitutive law given in Eqn.(3.10). Each of them may be conveniently written as the sum of a contribution depending on the interpolation of the bulk modulus $K(\rho_e,\rho_{g,e})\mathbf{K}_{K0,e}$, and a contribution depending on the shear modulus $G(\rho_e,\rho_{g,e})\mathbf{K}_{G0,e}$, where $\mathbf{K}_{K0,e}$ and $\mathbf{K}_{G0,e}$ both refer to $\rho_e = 1$, see also [26]. For the j-th of the l load cases, $\mathbf{F}_j$ is the load vector, whereas $\mathbf{U}_j$ is the corresponding nodal displacement vector.

The i-th of the m displacement components to be controlled is denoted by u_i. Eqn.(3.11c) enforces a prescribed limit $u_{lim,i}$, where $u_{lim,i}$ stands for the relevant maximum displacement allowed. Assuming that u_i is an entry of $\mathbf{U}_j$, i.e. that the i-th displacement constraint refers to the j-th load case, one has:

$$u_i = \mathbf{L}_i^T \mathbf{U}_j, \tag{3.12}$$

where $\mathbf{L}_i$ is a vector made of zeros except for the entry referring to the i-th displacement degree of freedom, which takes unitary value (see also Chapter 2).

Eqn.(3.11d) prescribes a minimum value for the weight fraction of the porous microstructure, namely f_g.

As discussed in Section 3.1.1.1 and 3.1.1.2, a lower bound $\rho_{g,min}$ applies to avoid collapse of the HCP layout of circular/spherical holes. Also, un upper bound $\rho_{g,max}$ should be prescribed to prevent cavities with radii that are too small with respect to the adopted manufacturing technique. The upper bound is enforced in Eqn.(3.11) through the statement of side constraints for the variables $\rho_{g,e}$. The same technique cannot be used to enforce $\rho_{g,min}$, since, according to Eqn.(3.10), the void phase arises for $\rho = \rho_g = 0$. To prevent values in the undesired range $0 < \rho_g < \rho_{g,min}$ a projection approach can be conveniently implemented when dealing with the simultaneous design of the boundaries of the component and of the internal graded microstructure. Alternatively, when a problem of optimal infill is considered, both $\rho_{g,min}$ and $\rho_{g,max}$ can be straightforwardly enforced through side constraints.

3.2.2. Numerical Implementation

Details are given in Appendix A.2 on the treatment of the density fields to avoid well-known numerical instabilities and achieve a manufacturable porous phase enforcing $\rho_{g,min}$. In the numerical simulations that follow it is assumed that $\rho_{g,min} = 0.30$ and $\rho_{g,max} = 0.85$, both in the two-dimensional and three-dimensional case.

The optimization problem in Eqn.(3.11) is solved via sequential convex programming, adopting the Method of Moving Asymptotes (MMA) as minimizer. The modified augmented Lagrangian approach adopted to address the multi-constrained formulation via a gradient-based algorithm is detailed in Appendix A.3.

3.2.3. Post-Processing for Manufacturing

A simple procedure is proposed to get blueprints, extracting the boundaries of the component and prescribing location and grading of the porous phase, with minor modifications between 2D and 3D problems. As a result of the minimization procedure, an optimal distribution of the element unknowns ρ_e and $\rho_{g,e}$ is found throughout the design domain. The boundaries of the object are detected by processing the distribution of the overall material density, namely $\rho_e + (1-\rho_e)\rho_{g,e}$, thus handling together both the solid material region, i.e. ρ_e, and the graded material one, i.e. $(1-\rho_e)\rho_{g,e}$. The threshold $\rho_{g,min}$ is adopted to detect the final shape of the blueprint: according to the introduced projections, all the regions where the overall material density is less than this value should be considered neither infill nor solid phase, i.e. they should be regarded as void. It must be remarked that the use of $\rho_{g,min}$ as a threshold has a negligible effect on the result of the detection procedure when dealing with the boundary between solid and void. This because of the projection in Eqn.(A.3). The iso-line computed at $\rho_{g,min}$ is used when dealing with the pixel-based density distribution in 2D. The iso-surface computed at the same threshold is used for the voxel-based material densities in 3D. The region inscribed in the detected/assigned boundaries defines a surface in the former case, and a volume in the latter.

Denoting by i_1, i_2 and i_3 three integer indices starting at the origin of a prescribed reference system, the z_1-, z_2- and z_3- coordinates of the centers of the circular/spherical holes in the adopted HCP arrangement (with base cell dimension d) are given by:

$$\left(i_1 + \frac{1}{2}\text{mod}(i_2+i_3,2)\right)d, \quad \left(\frac{\sqrt{3}}{2}i_2 + \frac{1}{2\sqrt{3}}\text{mod}(i_3,2)\right)d, \quad \left(\frac{\sqrt{6}}{3}i_3\right)d, \tag{3.13}$$

where the operator "mod" returns the remainder after division of two terms. For the generic hole, the average value of the quantity $(1-\rho_e)\rho_{g,e}$ is computed over the elements falling within a neighbourhood of its center with diameter $d/2$, and denoted by $\overline{\rho}_g$. No hole is allowed if any of the surrounding elements falling within the area defined above has $\rho_{g,e} = 0$ or $\rho_e = 1$. In 2D, according to Eqn.(3.6), the radius of a circular hole reads:

$$r = \left(\frac{(1-\overline{\rho}_g)\sqrt{3}}{2\pi}\right)^{1/2} d. \tag{3.14}$$

In 3D, according to Eqn.(3.8), the radius of a spherical hole reads:

$$r = \left(\frac{(1-\overline{\rho}_g)3\sqrt{2}}{8\pi} \right)^{1/3} d. \tag{3.15}$$

The final geometry is given by Boolean subtraction of the simple geometrical entities representing the holes (circles or spheres) from the shape representing the region within the external boundaries. The graphical information can be efficiently exported using an Initial Graphics Exchange Specification (IGES) format. Alternatively, a Standard Tassellation Language (STL) format can be used.

A few specimens have been manufactured by means of a Fused Deposition Modeling (FDM) 3D-printer to perform a preliminary test with respect to fabrication of the graded porous microstructures herein considered. The samples shown in Figure 3.6 consist of an optimized cantilever beam with dimensions $125 \times 80 \times 6$ mm and a portion of porous solid material with size $40 \times 20\sqrt{3} \times 10\sqrt{2}/\sqrt{3}$ mm. Samples are as-built, with no finishing. They have been fabricated through deposition of horizontal layers, meaning that the building direction is the vertical one.

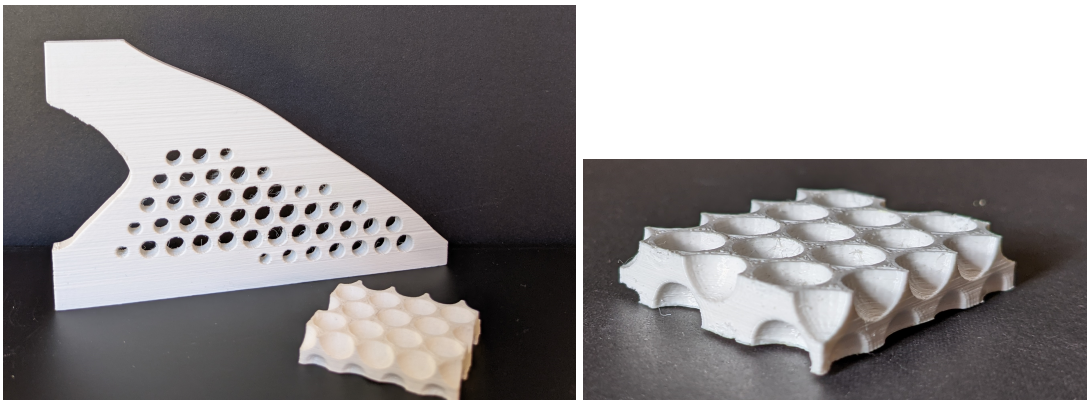

Figure 3.6: Test specimens fabricated by means of Fused Deposition Modeling without the need of supports.

3.3. Numerical Simulations

Numerical examples are presented to assess the method introduced in Section 3.2, considering two- and three- dimensional applications. The constraints enforced to govern the deflection are such that, in each one of the considered nodes, the controlled component of the displacement cannot overcome α times that computed adopting $\rho = 1$ everywhere (full material in the entire design domain). In the two- dimensional numerical applications of Sections 3.3.1- Appendix A.5 it is assumed that $\alpha = 1.5$, whereas $\alpha = 2.5$ is used for the three-dimensional example of

Section 3.3.3. Geometry and boundary conditions are those presented in Figures 3.7 and 3.8.

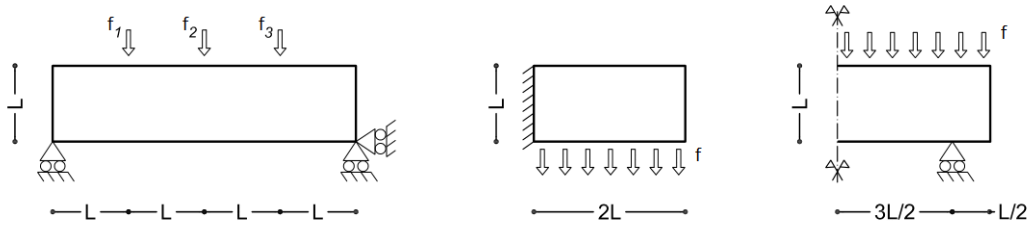

(a) (b) (c)

Figure 3.7: Geometry and boundary conditions for the two-dimensional numerical examples.

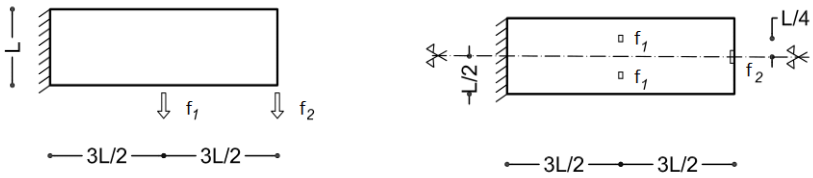

(a) lateral view (b) view from below

Figure 3.8: Geometry and boundary conditions for the three-dimensional numerical example

For all the examples, the filter radius r_f used for ρ_e is $L/10$, whereas the filter radius for $\rho_{g,e}$ reads $r_{g,f} = 2r_f$, if not differently specified. Solutions are generated by enforcing different values of $f_g \geq 0$ in the formulation of Eqn.(3.11). For each numerical investigation, the weight of the achieved optimal design is given in terms of the ratio V/V_0, where V is the weight at convergence and V_0 is the weight of the entire design domain made of full material. All the presented layouts fulfill the enforced displacement constraints. Noting that L= 100 unit length, and f= 1 unit force.

3.3.1. Design of a Simply-Supported Beam Under Multiple Load Cases

The $4L \times L$ simply-supported beam drawn in Figure 3.7a is addressed, adopting a mesh of 400×100 square finite elements. Four load cases are considered: i) f_1, ii) f_2, iii) f_3, iv) f_1, f_2, f_3 acting simultaneously, with $f_1 = f_2 = f_3$. For each one of the load cases, the displacement control is operated as described above, i.e. enforcing that the vertical displacement at the loaded point/points is not bigger than one and a half times that computed for the full material design domain.

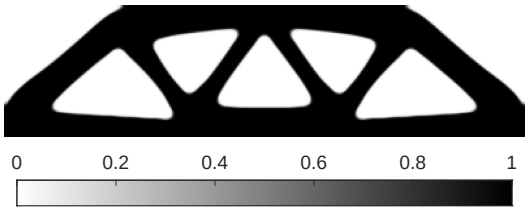

Figure 3.9: Example 1. Optimal design for $f_g = 0$, $V/V_0 = 0.533$.

The optimal solution achieved for $f_g = 0$ is shown through the map of element densities $\rho_e + (1-\rho_e)\rho_{g,e}$ that is represented in Figure 3.9. A black-and-white statically-determinate truss is found to handle multiple load cases. No phase of grade material is used. The weight at convergence is slightly bigger than half of that of the (full material) reference solution, being $V/V_0 = 0.533$. Indeed, the homogenized material laws derived in Section 3.1 are such that no advantage arises in terms of stiffness when using intermediate densities instead of full material, see in particular the numerical investigation and experimental tests reported in [157] and [38], respectively.

By adopting $f_g > 0$ in the formulation of Eqn.(3.11), a minimum amount of graded material is distributed at the cost of an increase in the weight of the optimal solution. This has the aim of exploiting beneficial features that porous microstructures inherently provide, including redundancy of load paths, high bending stiffness-to-weight ratio, and robustness with respect to force variations, see e.g. [30].

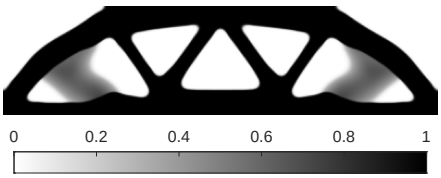

(a) $f_g = 0.05$, $V/V_0 = 0.547$

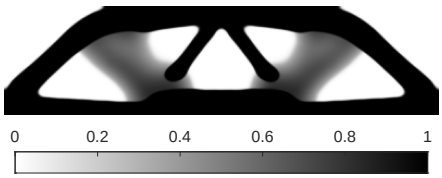

(b) $f_g = 0.10$, $V/V_0 = 0.555$

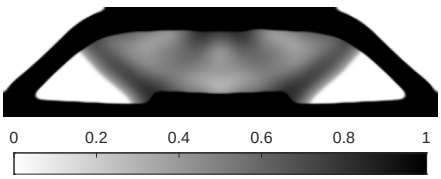

(c) $f_g = 0.15$, $V/V_0 = 0.576$

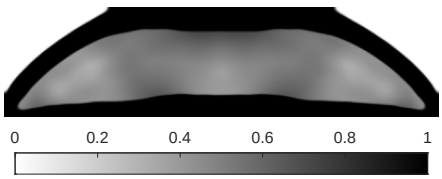

(d) $f_g = 0.20$, $V/V_0 = 0.596$

Figure 3.10: Example 1. Optimal designs

Figure 3.10 shows the optimal material layouts found by enforcing values of f_g in the range 5-20%, while preserving the structural stiffness of the previous black-and-white solution. All the optimal layouts are characterized by the presence of a solid phase (black), a void phase (white) and a phase of graded material (grey) with density falling in the range $\rho_{g,min}$-$\rho_{g,max}$ (0.30-0.85). For $f_g = 0.05$ some graded material arises to the detriment of the outer inclined members lying below the upper chord in the black-and-white solution. Indeed, the increase in weight is quite low with respect to the solution reported in Figure 3.9. For $f_g = 0.10$ these members are completely replaced by porous material, whereas for $f_g = 0.15$ only the upper and lower chord are made of full material. The latter solution has a weight ratio $V/V_0 = 0.576$, i.e. it is only 8% heavier than the black-and-white solution. The solution found for $f_g = 0.20$ is a variation of that achieved for $f_g = 0.15$, in which the region sandwiched between the upper and the lower solid chord consists of the graded material only. In terms of weight, this coated beam costs around 12% more than the truss design of Figure 3.10. No void phase arises within the component, meaning that in a layer-by-layer manufacturing process the additional material needed in the printing process is that related to manufacturing of the graded phase only. It must be remarked that specific approaches of topology optimization exist that have been especially conceived to design coated and composite sandwich structures, see in particular [37, 108, 151, 160, 161]. This kind of structure may spontaneously arise within the proposed procedure, depending on the value of f_g. Differently from the above mentioned contributions, the thickness of the coating, if any, is an outcome of the implemented optimization procedure. However, this could be controlled by leveraging the proposed two-phase material model, that means adopting one of the methods reviewed in [81] to control the minimum and maximum length-scales for the distribution of the minimization unknowns ρ_e. Reference is made also to [107], concerning equal-width length-scale control.

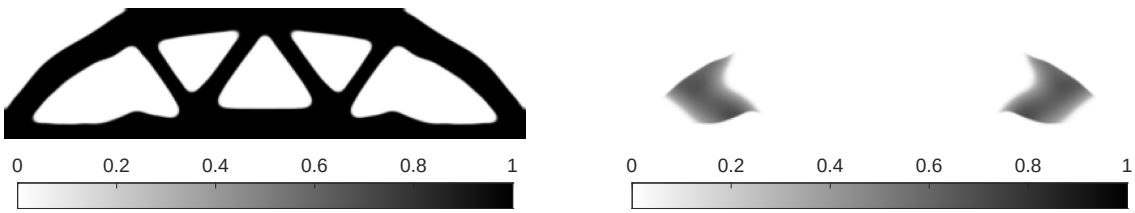

(a) Solid phase ρ_e (b) Infill $(1-\rho_e)\rho_{g,e}$

Figure 3.11: Example 1. Optimal design for $f_g = 0.05$, $V/V_0 = 0.533$: maps of the distribution.

In Figure 3.11 maps of the distribution of the solid phase ρ_e (a) and of the graded phase $(1-\rho_e)\rho_{g,e}$ (b) are shown separately, concerning the design for $f_g = 0.05$, see Figure 3.10a. No overlapping area appears when comparing the two maps of Figure 3.11, thus assessing the

effectiveness of the two-phase material law presented in Section 3.1.2. Indeed, the adoption of two variables is a key feature to control the amount of graded material in the final layout and to avoid the arising of porous material in the range $\rho_{g,max}$-1. Also, no grey region is found with density value falling below the prescribed lower bound $\rho_{g,min}$.

It has been already remarked that the enforcement of $f_g > 0$ does not generally imply a mere addition of some graded phase to the relevant black-and-white-design. Even in the design achieved for the lowest weight fraction of graded material ($f_g = 0.05$) the solid phase is quite different with respect the solution found when using $f_g = 0$. Indeed, looking at Figure 3.11a in comparison to Figure 3.9, one may notice not only a different thickness of some elements, but also a particular arrangement of the lower and the upper chord to accommodate the porous phase.

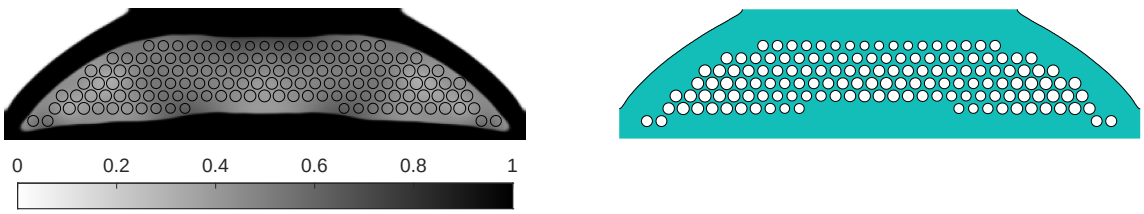

(a) Overlay of the HPC circular holes and of the optimal distribution of material density

(b) Final layout

Figure 3.12: Example 1. Design for $f_g = 0.20$, d=L/9 (a); final layout (b).

Figure 3.12 provides a possible final layout for the sandwich component found when optimizing for $f_g = 0.20$, according to the post-processing procedure detailed in Section 3.2.3. Figure 3.12a shows an overlay of the optimal distribution of material density and of the set of the graded circular holes in a hexagonal-closed-packed arrangement that may be computed for $d = L/9$. In Figure 3.12b the relevant blueprint is depicted.

To improve the match of the grey regions with the distribution of repetitive cells of graded holes (especially in the vicinity of the solid phase), to fully respect separation of length scales, and to minimize any other bias inherent in the post-processing procedure, smaller values of the base cell dimension d may be conveniently used. This mainly depends on the adopted manufacturing technology.

A preliminary numerical investigation is performed to analyze the structural behaviour of the blueprint of the truss represented in Figure 3.9 and that of the blueprint of the sandwich component shown in Figure 3.12, by means of full-scale finite element analyses. The final weight ratio for the former layout is $V/V_0 = 0.555$, whereas $V/V_0 = 0.628$ for the latter. Meshes of

quadrangular elements have been generated enforcing a maximum edge length equal to $10^{-2}L$, ending up with around $20 \cdot 10^3$ and $25 \cdot 10^3$ elements, respectively. The load case labeled as iv) has been considered, namely f_1, f_2, f_3 (with $f_1 = f_2 = f_3 = f$) acting simultaneously. In both models stiffer regions (square zones with side $L/10$) have been introduced around point forces and restraints, see Figure 3.7a, by prescribing a magnified Young's modulus ($\times 10$). These numerical simulations have been performed considering $L = 100\,mm$, out-of-plane thickness $L/10$, $E = 1MPa$, $\nu = 0.3$, $f = 1N$. In Table 3.1, values of the maximum deflection read under the loaded points are reported for the achieved optimal distribution of material (multi-scale design), as well as for full-scale finite element analyses of the blueprints. The maximum deflection occurs at the node where the central load f_2 is applied. When computed for the truss blueprint, it is 5% larger than that read for the blueprint of the sandwich specimen. According to a two-dimensional linear buckling analysis, the first eigenvalue computed for the latter is almost three times that found when analyzing the former.

	Load type	Multi-scale design			Full-scale analysis of blueprints		
		Layout	V/V_0	v^{max}	Layout	V/V_0	v^{max}
Ex. 1	$f_1 = f_2 = f_3$	Fig. 3.9	0.533	7.44	truss	0.555	7.18
		Fig. 3.10d	0.596	7.58	Fig. 3.12 ($d = L/9$)	0.628	6.82
Ex. 2	f	Fig. 3.14	0.556	4.56	truss	0.569	4.36
		Fig. 3.15b	0.578	4.56	Fig. 3.17b ($d = L/12$)	0.608	4.21
					Fig. 3.18 ($d = L/16$)	0.598	4.26
	f_{var}				truss	0.569	4.99
					Fig. 3.17b ($d = L/12$)	0.608	4.53
					Fig. 3.18 ($d = L/16$)	0.598	4.61

Table 3.1: Multi-scale design vs. full-scale finite element analysis of the blueprints: values of the maximum deflection under the loaded points v^{max} (mm).

A final investigation is performed controlling not only the displacements involved in the definition of the work of the external forces, as done above, but also the horizontal displacement at the roller. The former constraints are responsible for the arising of a final layout that is able to carry the loads with limited deflection of the beam, whereas the latter may be seen as an additional serviceability condition (referring in this case to the adopted bearing device). In the simulations presented next, the horizontal displacement at the roller is required not to exceed the value computed for the entire domain made of full material. Four additional constraints are needed to control the displacement, considering the multiple load cases. In Figure 3.13a, the optimal solution achieved for $f_g = 0$ is presented. Compared to that presented in Figure 3.9, a more branched layout arises to meet the prescribed enforcement on the horizontal displacement,

at the cost of a 10% increase in terms of weight. In Figure 3.13b the optimal solution found for $f_g = 0.15$ is reported, consisting of a sandwiched region integrated with elements made of full material. Compared to the layout achieved for the same amount of graded material in Figure 3.10c, the additional control of the horizontal displacement at the roller calls for a 8% increase in the final weight.

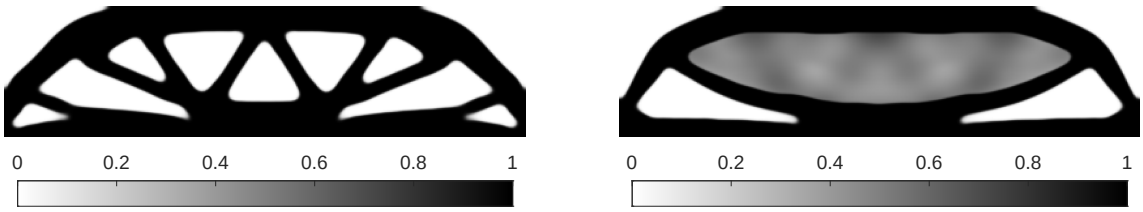

(a) $f_g = 0, V/V_0 = 0.595$ (b) $f_g = 0.15, V/V_0 = 0.621$

Figure 3.13: Example 1. Optimal design, including control on the horizontal displacement at the roller.

3.3.2. Design of a Cantilever Beam Under a Uniformly Distributed Load

The optimal design of the $2L \times L$ cantilever beam in Figure 3.7b is dealt with, adopting a mesh of 200×100 square finite elements. A uniformly distributed load with intensity f acting along the entire lower edge of the rectangular design domain is considered in the optimization. The vertical displacement of each one of the nodes along the edge is controlled by means of a local constraint. In this example, the modified augmented lagrangian approach detailed in Appendix A.3 handles 200 enforcements of the type in Eqn.(3.11c), along with the constraint governing the minimum amount of graded material to be distributed, namely Eqn.(3.11d).

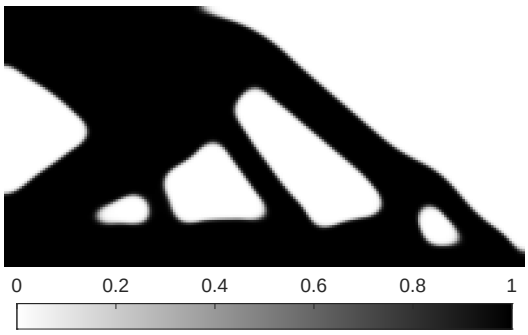

Figure 3.14: Example 2. Optimal design for $f_g = 0, V/V_0 = 0.556$.

At first, the case $f_g = 0$ is considered. The map of element densities $\rho_e + (1-\rho_e)\rho_{g,e}$ achieved

by the implemented multi-constrained formulation is given in Figure 3.14. A black-and-white solution is found, namely $\rho_{g,e} = 0$ in the entire design domain. A thick horizontal element, which collects the orthogonal load while acting as a strut, is hanging from the upper part of the truss through a system of multiple ties. The weight ratio at convergence is $V/V_0 = 0.556$.

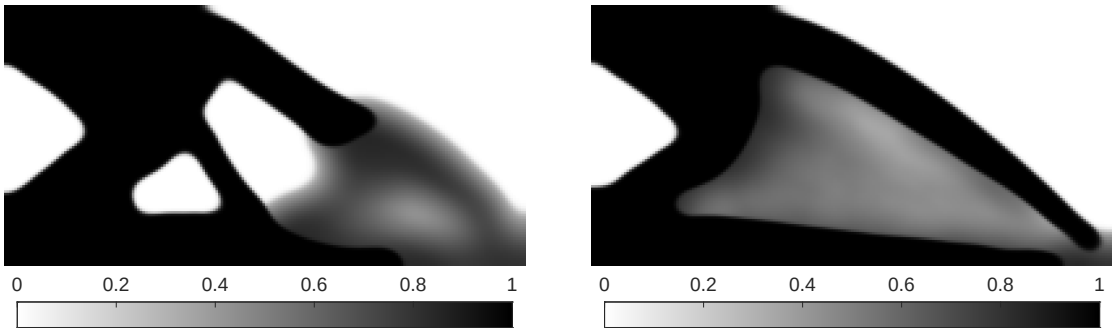

(a) $f_g = 0.125$, $V/V_0 = 0.576$ (b) $f_g = 0.15$, $V/V_0 = 0.578$

Figure 3.15: Example 2. Optimal design.

A minimum amount of graded material appears in the optimal solution, if $f_g > 0$ is enforced in the solution of Eqn.(3.11). In Figure 3.15a and Figure 3.15b the optimal solutions achieved by setting $f_g = 0.125$ and $f_g = 0.15$ are shown, respectively. In the former case, the tip of the cantilever beam, i.e. its less stressed part, is made of porous material. The graded area is supported, from below, by a tapered horizontal element made of full material and, from above, by a single tie. Indeed, the remaining part resembles a standard truss. The final weight ratio is $V/V_0 = 0.576$. In the latter case, the optimal design is not far from the type of solution already seen in Figure 3.10d. Indeed, only the very last end of the tip of the arising cantilever beam is made of graded material only, whereas most of the porous phase is surrounded by a thick coating of solid material. The final weight ratio for the latter design is $V/V_0 = 0.578$, only 4% more than the truss design in Figure 3.14.

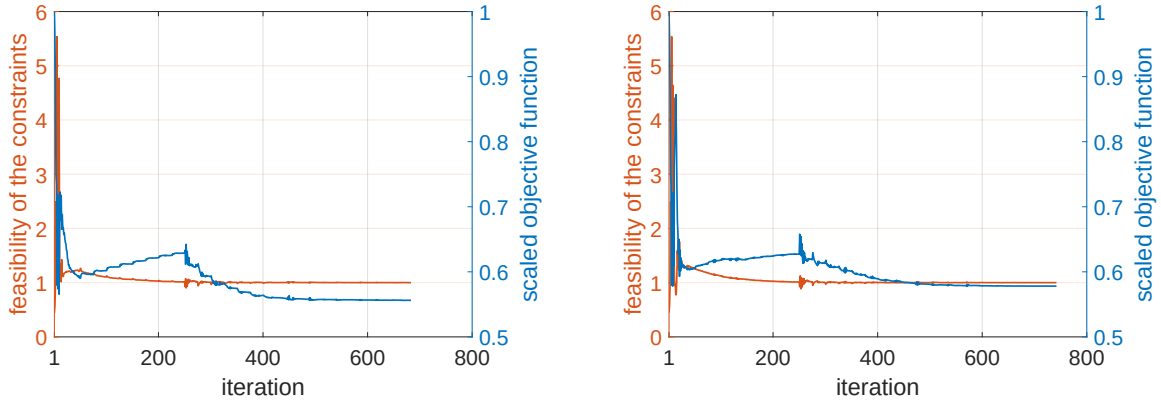

(a) $f_g = 0$, final $V/V_0 = 0.556$

(b) $f_g = 0.15$, final $V/V_0 = 0.578$

Figure 3.16: Example 2. History plot of the scaled objective function V/V_0 and of the feasibility of the constraints.

In Figure 3.16, the history plots of the scaled objective function V/V_0 and the feasibility of the constraints are presented for the minimization problems concerning the design in Figure 3.14, with $f_g = 0$, and the layout in Figure 3.15b, with $f_g = 0.15$. The represented feasibility refers to the maximum value of the left hand side of Eqn.(3.11c) and Eqn.(3.11d) written as $u_i/u_{lim,i} \leq 1$ and $f_g \sum_{e=1}^{n} V_{0,e} / \sum_{e=1}^{n} (1-\rho_e)\rho_{g,e} V_{0,e} \leq 1$, respectively. The optimization is initialized with $\rho_e = 1$ and $\rho_{g,e} = 0$ everywhere. The continuation scheme for p is such that the initial value $p = 3$ is used for the first 50 iterations, whereas an increase of 0.25 is given every 25 iterations until $p = 6$, see Section 3.1.2. The parameter β, both for Eqn.(A.3) and Eqn.(A.4), is equal to 2 in the first 250 iterations; then it increases by 2 every 25 iterations until $\beta = 16$, see Appendix A.2. As expected, the continuation approach used with p is responsible for an increase in the objective function, whereas that used with β is related to a decrease. Both simulations end with full feasibility of the enforced constraints.

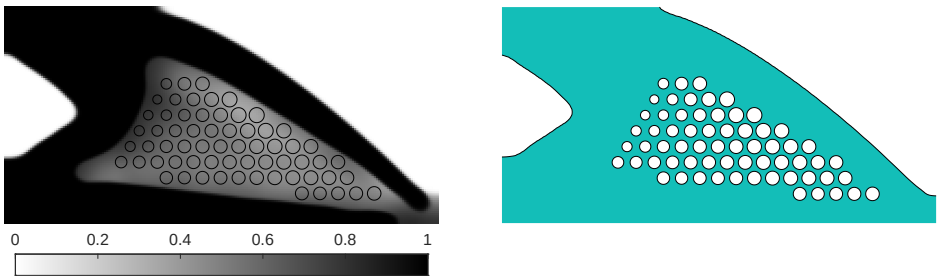

(a) Overlay of the HPC circular holes and of the optimal distribution of material density

(b) Final layout

Figure 3.17: Example 2. Design for $f_g = 0.15$, $d = L/12$, $V/V_0 = 0.608$.

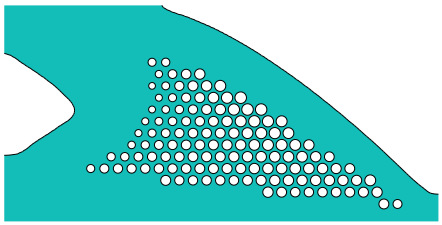

Figure 3.18: Example 2. Final layout, optimal design for $f_g = 0.15$, $d = L/16$, $V/V_0 = 0.598$.

For the component with $f_g = 0.15$, two possible final layouts are given in Figure 3.17 and 3.18, for $d = L/12$ and $d = L/16$ respectively. In Figure 3.17a an overlay of the optimal distribution of material density and of the set of the graded circular holes is provided, as well.

Full-scale finite element analyses have been performed for a preliminary assessment of the structural behaviour of the blueprints represented in Figure 3.17b and Figure 3.18, with respect to the blueprint of the solid-and-void design shown in Figure 3.14. The final weight ratio for the truss-like layout is $V/V_0 = 0.569$. It increases to $V/V_0 = 0.608$ when processing the design for $f_g = 0.15$ using $d = L/12$. For the same density distribution, the adoption $d = L/16$ provides a better approximation of the grey area, and the relevant weight ratio reads $V/V_0 = 0.598$. Meshes of about $15 \cdot 10^3$ quadrangular elements have been generated by enforcing a maximum edge length equal to $7.5 \cdot 10^{-3} L$. Numerical simulations have been performed considering $L = 100\,mm$, out-of-plane thickness $L/10$, $E = 1MPa$, $\nu = 0.3$, $f = 0.01N/mm$. In Table 3.1, values of the maximum deflection read at the tip are reported for the achieved optimal distribution of material (multi-scale design), and for full-scale finite element analyses of the blueprints.

At first, the uniformly distributed load with intensity f is considered in the simulations. The maximum deflection read at the tip of the blueprint of the truss-like layout is 3% and 2% larger

than that read for the full-scale models of the blueprints of Figure 3.17 and Figure 3.18, respectively. When homogenization is used within topology optimization, full-scale analyses are recommended to check that a suitable separation of scales (porous material/structure) exists, such that the multi-scale framework may be effectively relied upon [157]. To this extent, the very small variation that can be read in Table 3.1 looking at the values v^{max} computed via full-scale analyses of the blueprints with $d = L/12$ and $d = L/16$, confirms the validity of the multi-scale approach used in the optimization, at least from an engineering point of view.

A further numerical investigation is performed assuming a variation in the load distribution. Denoting by x the horizontal axis spanning from the left end of the lower edge of the rectangular design domain, the intensity $f_{var} = 5/32\, qx^4/L^4$ is accounted for to shift the (equal) resultant into the right half of the domain. The maximum deflection read at the tip of the blueprint of the truss-like layout is 15% larger than that found in case of uniformly distributed load. As expected, the blueprints originated from the multi-scale design for $f_g = 0.15$ exhibit increased robustness with respect to force variations. For both, the decrease in terms of overall stiffness is around 7%, less than one half that reported for $f_g = 0$.

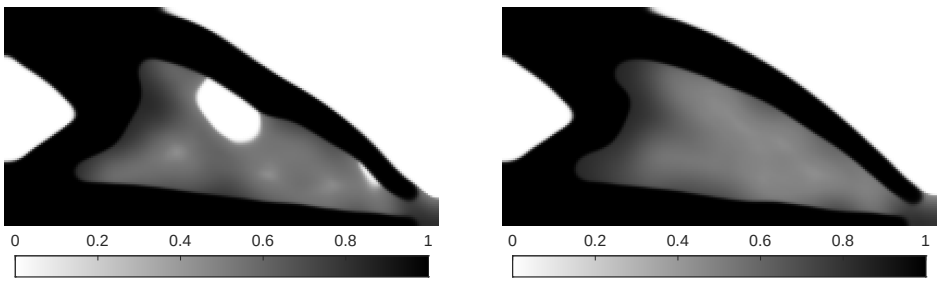

(a) $f_g = 0.15$, $V/V_0 = 0.579$ (b) $f_g = 0.175$, $V/V_0 = 0.582$

Figure 3.19: Example 2. Optimal design with $\rho_{g,min} = 0.45$

The adoption of the two-material law presented in Section 3.1.2 allows controlling the minimum value of the porous material density, $\rho_{g,min}$, in conjunction with a projection of the filtered variables $\rho_{g,e}$, see Section A.2. To assess this feature, the optimization is re-run enforcing $\rho_{g,min} = 0.45$, instead of the value adopted previously ($\rho_{g,min} = 0.30$). The design found for $f_g = 0.15$ is reported in Figure 3.19a. The layout of the solid material is not far from that found for the same value of f_g but smaller $\rho_{g,min}$, see Figure 3.15b. However, two void areas break the continuity of the graded material inside the solid elements. The final weight ratio for the latter design is $V/V_0 = 0.579$, approximately the same as the previous result. By allowing for a larger amount of porous material, i.e. using $f_g = 0.175$, the continuity of the inner graded region is recovered, with a weight ratio $V/V_0 = 0.582$, see Figure 3.19b. In this case, the increase in

$\rho_{g,min}$ can be compensated for by the enforcement of a larger f_g: the type of optimal solution is not affected, whereas the layout of the components (porous and solid material) is re-arranged with a minor increase in weight.

3.3.3. Design of a Three-Dimensional Cantilever Beam

A three-dimensional application is considered. The $3L \times L \times L$ cantilever beam shown in Figure 3.8 is herein analyzed considering three load cases: i) f_1, ii) f_2, iii) f_1, f_2 acting simultaneously. Vertical forces are such that the resultant of f_1 is equal to that of f_2. Due to symmetry in geometry and load, only one half of the specimen is analyzed, using a mesh of $108 \times 36 \times 18$ cubic elements. The deflection control is operated at the loaded nodes: 6 nodes are used to address f_1 and the same for f_2.

The implementation in the three-dimensional framework is fully along the lines of the two-dimensional algorithm. In this extension, the element matrices $\mathbf{K}_{K0,e}$ and $\mathbf{K}_{G0,e}$ of Section 3.2.1 are computed using brick shape functions and three-dimensional elasticity. The two-phase material law of Section 3.1.2 allows for the distribution of full material and void, along with a fraction of porous microstructure with graded spherical holes. Indeed, $K(\rho_g)$ and $G(\rho_g)$ are those derived in Section 3.1.1.2. It must be remarked that the proposed algorithm, which exploits regular meshes and employs the gradient-based Methods of Moving Asymptotes [145], is well-suited to be implemented within large-scale fully parallelized optimization framework, as the one implemented in [1], to allow for an accurate description of the geometry of the optimal layouts.

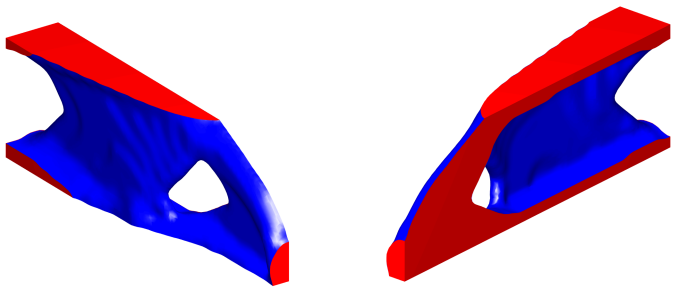

(a) External view (b) Internal view

Figure 3.20: Example 4. Final design for $f_g = 0$, $V/V_0 = 0.242$

The solution found for $f_g = 0$ is presented in Figure 3.20. An external and an internal view of the considered half part of the specimen are shown. Following [58], an iso-surface of the smoothed element densities $\rho_e + (1-\rho_e)\rho_{g,e}$ is employed to represent the boundaries of the optimized object. No fraction of graded material arises. The optimal design consists of a box-

shaped structure connected with a truss-like tip, both made of full material only. Reference is made to [137] for a discussion about optimality of closed-walled layouts for pure stiffness optimization. The weight ratio of the achieved layout reads $V/V_0 = 0.242$.

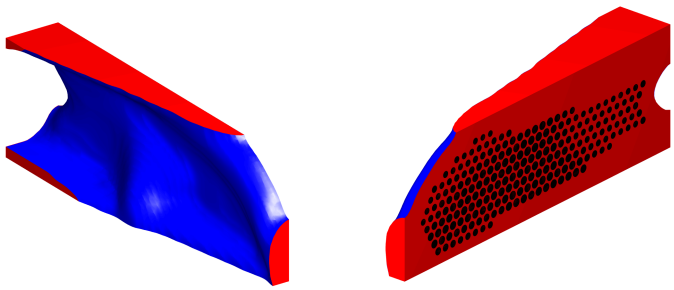

(a) External view (b) Internal view

Figure 3.21: Example 4. Final design for: $f_g = 0.10$, $V/V_0 = 0.274$, $d = L/12$

The optimal solution found for $f_g = 0.10$ is presented in Figure 3.21. As before, the boundaries of the optimized object are sketched by means of an iso-surface of the smoothed element densities. The post-processing procedure in Section 3.2.3 is used with $d = L/12$ to compute position and radius of the spherical holes corresponding to the achieved distribution of the quantity $(1-\rho_e)\rho_{g,e}$. The comments already formulated for the two-dimensional examples on the selection of d, apply here as well. The optimal layout has a final weight ratio of $V/V_0 = 0.274$, approximately 13% more than the previous one. The external shape of the object is not far from that represented in Figure 3.20. However, the internal cavity is replaced by graded porous microstructures, with some benefit, among the others, for layer-by-layer manufacturing.

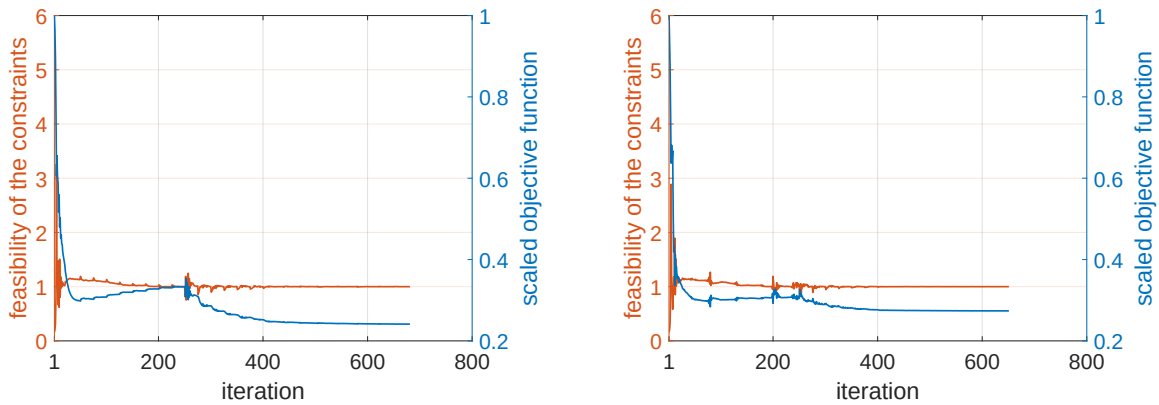

(a) $f_g = 0$, final $V/V_0 = 0.242$ (b) $f_g = 0.10$, final $V/V_0 = 0.274$

Figure 3.22: Example 4. History plot of the scaled objective function V/V_0 and of the feasibility of the constraints

The history plots of the scaled objective function V/V_0 and of the feasibility of the constraints for the considered three-dimensional problems are reported in Figure 3.22. Similar features to those already outlined for the curves in Figure 3.16 can be pointed out.

3.4. Summary and Conclusions

In this work, a multi-scale topology optimization approach has been proposed for designing structural components that achieve minimum weight while adhering to specified load and displacement limits. Through the implementation of numerical homogenization, the macroscopic elastic properties of hexagonal close-packed arrangements with circular and spherical holes were effectively characterized, taking into account the radius of these cavities. The analysis involved applying an isotropic constitutive law for two-dimensional cases and a transversely isotropic law for three-dimensional cases, addressing the moderate anisotropy observed in three-dimensional microstructures. By deriving the elastic properties in terms of the bulk modulus and the shear modulus, and considering varying densities, a comprehensive understanding of both porous phases was achieved.

A notable aspect of this research is the adoption of a multi-material interpolation law, allowing for the simultaneous distribution of a solid phase, a graded porous phase, and void. This approach is complemented by the use of filtering and projection procedures, which work in conjunction with the material law to promote smooth density distributions and prevent the emergence of porous material outside of specified density ranges.

Moreover, the approach includes a mechanism to ensure a minimum amount of graded porous microstructure in the optimal design. The culmination of this methodology is an optimal distribution of material density, which facilitates the clear identification of regions comprised of solid and graded phases. Additionally, a simple post-processing technique has been discussed for defining the boundaries of the component and the potential internal arrangements of circular or spherical holes with graded radii.

The approach also yields coated structures, where a solid coating encloses a region of porous material, adaptable to various load types and displacement constraints. The optimization procedure intrinsically determines the thickness and location of these coatings. Furthermore, full-scale finite element analyses conducted on two-dimensional blueprints, considering varying sizes of the porous microstructure, have validated the approach, showing a good correlation between computed and predicted displacements. Lastly, preliminary tests on the printability of these structures using layer-by-layer additive manufacturing processes have indicated promising results, especially in terms of supporting extended cavities with areas of graded material instead of void regions.

4 | Enhanced Topology Optimization: Graded Infill for Loading Uncertainty

In this chapter, the design optimization of composite structures comprising a solid phase and a specified fraction of graded infill is addressed. Utilizing homogenization-based topology optimization, the analysis incorporates uncertainties in loading amplitude. A two-phase material law incorporating void space is implemented to regulate both the distribution and permissible density of the graded infill. Numerical homogenization techniques are employed to ascertain the macroscopic elastic properties of isotropic and two types of orthotropic infills, prevalent in additive manufacturing applications.

The formulation of a minimum weight problem is enhanced by deterministic displacement constraints, which equivalently address probabilistic displacement enforcements under the assumption of normally distributed force amplitudes. The multi-constrained optimization problem is approached through sequential convex programming, facilitating an efficient resolution method in line with the approaches devised in the previous chapters.

4.1. Uncertainty in Multi-Scale Topology Optimization

In engineering applications, particularly in truss design, various sources of uncertainty such as load, geometry, and mechanical parameters are significant considerations. This concept has been explored extensively, as highlighted in studies like those referenced in [11] and [95]. When it comes to topology optimization, there are several predominant methods. One of these is reliability-based optimization, which involves defining limit states and evaluating their failure probabilities. This approach requires an understanding of the marginal probability density functions for the random variables representing uncertainties, as discussed in [138]. Another method is robust design, which focuses on the first- and second-order stochastic moments of the system response, a concept detailed in [47]. This method has been particularly useful in dealing with random loads in compliant structures, as evidenced by research in [8, 67, 90], and for compliant mechanisms, as seen in [78]. Further extensive discussions on managing geometric and material uncertainties can be found in references [80] and [35].

It must be remarked that only a few investigations are available in the literature considering

load uncertainly in topology optimization with multiple material phases. In [164], robust multi-material structures under interval loading uncertainty are designed by combining orthogonal decomposition with uniform sampling, whereas [61] takes advantage of an alternating active-phase method to minimize a weighted sum of the mean and standard deviation of the structural compliance. In both cases, the strain energy at equilibrium is the objective function to be minimized, whereas the weight of each solid phase, or the available amount of material, is prescribed. No porous structure is allowed in the final design. The arising volume-constrained optimization is solved using evolutionary methods and optimality criteria, in [164] and [61] respectively.

In this contribution, we demonstrate that the original theory presented in [121] can be directly applied to displacement constraints in the context of any linear elastic structure. This application is relevant when dealing with structures subjected to a collection of point forces, all of which are influenced by a similar kind of uncertainty.

4.2. Method: Theory to Implementation

4.2.1. Material Law

A two-phase interpolation law is adopted to distribute full material and void, along with a fraction of a porous graded microstructure with prescribed layout. Assuming plane stress conditions, the Cartesian components of the macroscopic stress tensor σ_{ij} are gathered in the array $\underline{\sigma} = [\sigma_{11}\, \sigma_{22}\, \sigma_{12}]^T$ and, analogously, $\underline{\varepsilon} = [\varepsilon_{11}\, \varepsilon_{22}\, \gamma_{12}]^T$ for the in plane components of the macroscopic strain tensor ε_{ij}. The constitutive law for the herein considered linear elastic material reads $\underline{\sigma} = \mathbf{C}\underline{\varepsilon}$, where:

$$\mathbf{C}(\rho_1, \rho_2, \rho_g) = \mathbf{C}_{min} + \rho_1^p(\mathbf{C}_0 - \mathbf{C}_{min}) + \rho_2^p(1-\rho_1^p)\,(\mathbf{C}_H(\rho_g) - \mathbf{C}_{min})\,, \tag{4.1}$$

with penalization $p \geq 3$. In the above equation, $0 \leq \rho_1, \rho_2 \leq 1$ and $\rho_{g,min} \leq \rho_g \leq \rho_{g,max}$ are three variables governing the material law, being $\rho_{g,min}$ and $\rho_{g,max}$ the bounds of the admissible density range of the porous phase. For $\rho_1 = 1$, whatever the value of ρ_2 and ρ_g, the constitutive matrix is that of full material, i.e. $\mathbf{C}_0$. For $\rho_1 = \rho_2 = 0$, independently on the value of ρ_g, only the terms C_{min} survives, meaning that a fictitious stiffness that stands for void is found. For $\rho_1 = 0$ and $\rho_2 = 1$, a porous microstructure may arise with a macroscopic stiffness tensor $\mathbf{C}_H$ that depends on the density of the porous phase ρ_g, according to the following interpolation:

$$\mathbf{C}_H = \begin{bmatrix} c_{H,11}(\rho_g)C_{0,11} & c_{H,12}(\rho_g)C_{0,12} & 0 \\ & c_{H,22}(\rho_g)C_{0,22} & 0 \\ sym & & c_{H,33}(\rho_g)C_{0,33} \end{bmatrix}. \tag{4.2}$$

In the above equation, $C_{0,ij}$ are the entries of $\mathbf{C}_0$ and $0 \leq c_{H,ij} \leq 1$. It is also remarked that, for $\rho_2 = 1$, either graded or full material arises depending on the value of ρ_1, but void is not allowed. An additional comment is done with respect to the law used in Eqns.(3.10), which similarly handles a solid phase, a porous one and void. The three-parameter interpolation of Eqn.(4.1) may be considered as an enhancement of the two-parameter one in Eqn.(3.10): the use of an additional set of minimization variables allows for a stricter control on the density distribution (especially for what concerns bounds), at the cosy of an increase in terms of computational time. Of course, both laws may be declined for distributing isotropic and anisotropic phases.

The dependence of the macroscopic stress-strain matrix $\mathbf{C}_H$ on the density of the porous phase ρ_g is evaluated by performing numerical homogenization on the base cells represented in Figure 4.1, see in particular [68]. An hexagonal close-packing of circular holes (HCP), a diamond lattice (D), and an elongated diamond lattice (E), are considered in the numerical studies, being d the reference dimension of the microstructure. For the sake of simplicity, unitary Young's modulus and Poisson's ratio equal to $1/3$ are assumed. The pixel-based method implemented in [6] is used addressing a regular mesh with pixel dimension $l_{pix} = d/100$ and values of the material density in the interval 0.15-1. A fifth degree polynomial, for which zero stiffness is additionally enforced at $\rho_g = 0$, is used to fit the achieved results. It is well-known that the HCP microstructure is isotropic [48], whereas both the D and E lattices are orthotropic [79], see results in Table 4.1.

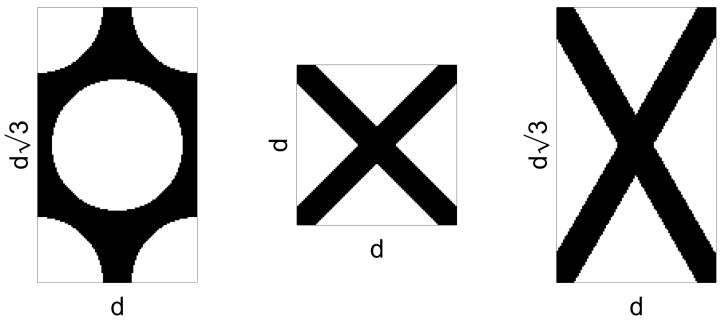

(a) Hexagonal close-packing of circular holes (HCP)

(b) Diamond lattice (D)

(c) Elongated diamond lattice (E)

Figure 4.1: Base cells used in the numerical studies (for $\rho_g = 0.40$)

		α_5	α_4	α_3	α_2	α_1
HCP	$c_{H,11}$	1.8839	−3.3427	2.2047	0.0887	0.1655
	$c_{H,22}$	1.8839	−3.3427	2.2047	0.0887	0.1655
	$c_{H,12}$	−1.3821	5.3524	−5.2365	1.8771	0.3890
	$c_{H,33}$	3.5169	−7.6903	5.9253	−0.8056	0.0537
D	$c_{H,11}$	0.2658	1.0553	−1.0613	0.5657	0.1745
	$c_{H,22}$	0.2658	1.0553	−1.0613	0.5657	0.1745
	$c_{H,12}$	7.1616	−15.3504	11.0124	−2.7829	0.9592
	$c_{H,33}$	2.9682	−5.8757	4.2530	−1.1244	0.7788
E	$c_{H,11}$	3.1347	−3.4690	1.4453	−0.1698	0.0588
	$c_{H,22}$	1.3045	−2.2048	1.5097	−0.1068	0.4974
	$c_{H,12}$	5.9369	−10.3534	5.9877	−1.1476	0.5764
	$c_{H,33}$	3.2259	−5.9110	3.9148	−0.7816	0.5520

Table 4.1: Interpolation law of the type $\alpha_i x^i$, with $i = 1,2,...,5$, for the components of the macroscopic stiffness tensor given in Eqn.(4.2), as computed for an hexagonal close-packing of circular holes (HCP), a diamond lattice (D) and an elongated diamond lattice (E), using numerical homogenization.

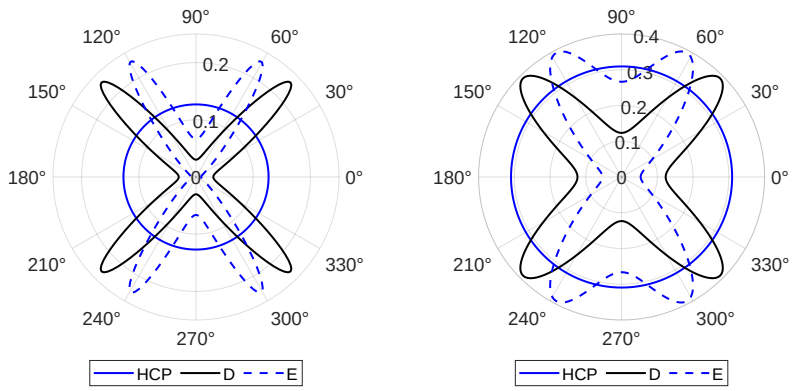

(a) $\rho_g = 0.40$ (b) $\rho_g = 0.60$

Figure 4.2: Apparent Young's modulus of the hexagonal close-packing of circular holes (HCP), diamond lattice (D) and elongated diamond lattice (E), depending on the orientation of the reference system. Values are scaled with respect to that of the full isotropic material phase.

Figure 4.2 shows polar diagrams of the apparent Young's modulus of the considered porous

microstructures for two different values of ρ_g, namely:

$$\frac{1}{E} = \frac{1}{E_1}c^4 + \left(\frac{1}{G_{12}} - 2\frac{\nu_{12}}{E_1}\right)s^2c^2 + \frac{1}{E_2}s^4, \tag{4.3}$$

for $\rho_g = 0.40$ and $\rho_g = 0.60$. Eqn.(4.3) gives the apparent value of the Young's modulus at the orientation θ from the horizontal direction, being $c = \cos\theta$ and $s = \sin\theta$, E_1 and E_2 the macroscopic Young's moduli along the horizontal and the vertical direction, respectively, ν_{12} and ν_{21} the Poisson's ratios (with $\nu_{12}E_2 = \nu_{21}E_1$), and G_{12} the macroscopic shear modulus, i.e.:

$$\begin{aligned} &\nu_{12} = \frac{C_{H,12}}{C_{H,22}}, \quad \nu_{21} = \frac{C_{H,12}}{C_{H,11}}, \quad G_{12} = C_{H,33}, \\ &E_{11} = C_{H,11}(1-\nu_{12}\nu_{21}), \quad E_{22} = C_{H,22}(1-\nu_{12}\nu_{21}), \end{aligned} \tag{4.4}$$

see e.g. [73].

For $\rho_g = 0.40$, the stiffest directions of the diamond infill and of the elongated diamond infill are characterized by an apparent elastic modulus that is almost twice than for the isotropic microstructure. Very small values of the elastic modulus are attained a few degree far away from these directions. For $\rho_g = 0.60$, the difference in terms of maximum stiffness decreases, but the weakest directions of the diamond infill and the horizontal direction of the elongated diamond infill are still characterized by low values of the elastic modulus. Due to the strong anisotropy of the rhombic cells, non-trivial distributions of the infill are expected when looking for optimal distribution of materials through Eqn.(4.1), see also [27].

4.2.2. Probabilistic Formulation

A finite element discretization of a given design domain is operated, using four-node displacement-based plane stress elements. Three sets of element-wise design variables are considered to implement the linear elastic material law of Eqn.(4.1). In the e-th of the n_e elements of the mesh, $\rho_{1,e}$, $\rho_{2,e}$ and $\rho_{g,e}$ are the discrete counterpart of the unknown fields ρ_1, ρ_2 and ρ_g, respectively.

A set of l probabilistic point loads acting simultaneously is considered. The intensity of the j–th force f_j is a random variable with normal (Gaussian) distribution and mean value $\bar{f}_j$. The covariance matrix is denoted as $\mathbf{K}_{ov}$, whose components are $k_{a,b}$. In case of uncorrelated loads, $\mathbf{K}_{ov}$ is a diagonal matrix whose terms are the variances of the random variables, i.e. $k_{a,a} = \sigma_a^2$, being σ_a the standard deviation of the intensity of the a–th force f_a. It is recalled that $\sigma_a = CV_a\bar{f}_a$, where CV_a is the coefficient of variation of f_a. If the loads are correlated, off-diagonal terms arise to account for the (non–zero) covariances, i.e. $k_{a,b} = \sigma_{a,b} = r_{ab}\sigma_a\sigma_b$, being $-1 \leq r_{ab} \leq 1$ the correlation between the intensity of the a–th force f_a and that of the

b–th force f_b.

A problem for the design of a topology of minimum weight under displacement constraints can be stated as:

$$\begin{cases} \min\limits_{\substack{0\leq\rho_{1,e},\rho_{2,e}\leq 1\\ \rho_{g,min}\leq\rho_{g,e}\leq\rho_{g,max}}} V = \sum\limits_{e=1}^{n}\Big(\rho_{1,e}+(1-\rho_{1,e})\rho_{2,e}\rho_{g,e}\Big)V_{0,e} & \text{(4.5a)}\\ \text{s.t. } \mathbf{K}(\boldsymbol{\rho_1},\boldsymbol{\rho_2},\boldsymbol{\rho_g})\,\mathbf{U}_j^{unit}=\mathbf{F}_j^{unit}, \quad \text{for } j=1...l, & \text{(4.5b)}\\ P(u_i\leq u_{lim,i})\geq 1-P_{fail}, \quad \text{for } i=1...m, & \text{(4.5c)}\\ \sum\limits_{e=1}^{n}(1-\rho_{1,e})\rho_{2,e}\rho_{g,e}V_{0,e}\geq f_g\sum\limits_{e=1}^{n}V_{0,e}. & \text{(4.5d)} \end{cases}$$

In the above statement, the objective function is the weight of the component, which is computed through the sum of the element contributions $(\rho_{1,e}+(1-\rho_{1,e})\rho_{2,e}\rho_{g,e})V_{0,e}$, being $V_{0,e}$ the volume of the e-th element for $\rho_e=1$. In this sum, the first term addresses full material, whereas the second the graded one.

Eqn.(4.5b) prescribes the discrete elastic equilibrium. The global stiffness matrix $\mathbf{K}(\boldsymbol{\rho_1},\boldsymbol{\rho_2},\boldsymbol{\rho_g})$ is computed by assembling the element contributions that account for the constitutive law given in Eqn.(4.1). Each of them may be conveniently written accounting separately for the contributions that depends on the interpolation of the terms $C_{H,11}$, $C_{H,12}$, $C_{H,22}$, $C_{H,33}$ in Eqn.(4.2). For the j-th of the l forces acting simultaneously on the domain, $\mathbf{F}_j^{unit}$ is the load vector that refers to a unit force with same point of application and direction of f_j, and $\mathbf{U}_j^{unit}$ is the corresponding nodal displacement vector.

The i-th of the m displacement components to be controlled is denoted by u_i. Eqn.(4.5c) enforces the probability that u_i does not exceed $u_{lim,i}$ to be at least equal to a prescribed value $1-P_{fail}$, being $u_{lim,i}$ for the relevant maximum displacement allowed and P_{fail} the accepted failure probability, see [150]. By exploiting superposition of effects, valid in the considered linear setting, the displacement u_i may be computed as the sum of the (deterministic) displacements $u_{i,j}^{unit}$ due to the forces $\mathbf{F}_j^{unit}$, scaled by the (probabilistic) magnitude f_j, i.e.:

$$u_i=\sum_{j=1}^{l}\mathbf{L}_i^T\mathbf{U}_j^{unit}f_j=\sum_{j=1}^{l}u_{i,j}^{unit}f_j, \tag{4.6}$$

where $\mathbf{L}_i$ is a vector made of zeros except for the entry referring to the i-th displacement degree of freedom, which takes unitary value.

According to [121], if $\xi_1,\xi_2,...,\xi_s$ have a joint normal distribution, then the vector $\mathbf{x}\in\mathbb{R}^s$ with

components $x_1, x_2, ..., x_s$ satisfying:

$$P\left(\sum_{h=1}^{s} x_r \xi_r \leq 0\right) \geq q, \tag{4.7}$$

is the same as that satisfying:

$$\sum_{h=1}^{s} x_h \bar{\xi}_h + \Phi^{-1}(q)\left(\mathbf{x}^T \mathbf{K}_{ov} \mathbf{x}\right)^{1/2} \leq 0, \tag{4.8}$$

where $\bar{\xi}_h$ is the mean value of ξ_h, $\mathbf{K}_{ov}$ is the covariance matrix of the random vector $\boldsymbol{\xi}$, and $\Phi^{-1}(q)$ is the inverse cumulative distribution function of the normal distribution (probit function), evaluated at the prescribed probability f.

Exploiting Eqn.(4.6), the probabilistic constraint of Eqn.(4.5c) may be re-written in the form:

$$P\left(\sum_{j=1}^{l} u_{i,j}^{unit} f_j - u_{lim,i} \leq 0\right) \geq 1 - P_{fail}. \tag{4.9}$$

According to Eqns.(4.7-4.8), since it has been assumed that $f_1, f_2, ..., f_l$ have a joint normal distribution, then the vector $\mathbf{u}_i^{unit}$ with components $u_{i,1}^{unit}, u_{i,2}^{unit}, ..., u_{i,l}^{unit}$ satisfying Eqn.(4.9) is the same as that satisfying:

$$\sum_{j=1}^{l} u_{i,j}^{unit} \bar{f}_j + \Phi^{-1}(1 - P_{fail})\left((\mathbf{u}_i^{unit})^T \mathbf{K}_{ov} \mathbf{u}_i^{unit}\right)^{1/2} - u_{lim,i} \leq 0, \tag{4.10}$$

where $-u_{lim,i}$ of Eqn.(4.9) may be straightforwardly handled through Eqns.(4.7-4.8) by introducing the slack variables $x_{s+1} = -1$ and $\xi_{s+1} = u_{lim,i}$, the latter with zero variance and zero covariance, see [90].

The above deterministic inequality will be implemented in Eqn.(4.5), instead of the original probability constraint.

The case $l = 2$ is analyzed, considering two forces f_1 and f_2, whose intensities are random variables. Eqn.(4.10) reads:

$$u_{i,1}^{unit}\bar{f}_1 + u_{i,2}^{unit}\bar{f}_2 + \Phi^{-1}(1-P_{fail})\left(\sigma_1^2(u_{i,1}^{unit})^2 + \sigma_2^2(u_{i,2}^{unit})^2 + 2\sigma_{12}u_{i,1}^{unit}u_{i,2}^{unit}\right)^{1/2} - u_{lim,i} \leq 0. \tag{4.11}$$

Whit respect to the case of deterministic forces, the probabilistic setting calls for the additional term scaled by $\Phi^{-1}(q)$, i.e the constraint becomes stricter. The term in brackets depends on the variances, σ_1^2 and σ_2^2, and the covariance, σ_{12}, of the intensity of the two considered forces.

Eqn.(4.5d) prescribes a minimum value for the weight fraction of the porous microstructure, namely f_g. A lower bound $\rho_{g,min}$ applies due to manufacturing constraints. An upper bound $\rho_{g,max}$ is prescribed, as well. Both bounds are enforced in Eqn.(4.5) through the statement of side constraints for the variables $\rho_{g,e}$.

4.2.3. Numerical Implementation

Details are given in Appendix B.1 on the treatment of the density fields to avoid numerical instabilities and control mesh-dependence. The well-known gradient-based Method of Moving Asymptotes (MMA) [145] is used to handle the multi-phase and multi-constrained optimization problem. The sensitivity of the probabilistic displacement constraints is computed as detailed in Appendix B.2.

4.3. Numerical Case Studies

Four numerical examples are presented to assess the method introduced in Section 4.2.2. The constraints enforced to govern the deflection are such that, in each one of the considered nodes, the controlled component of the displacement is not allowed to exceed α times that computed adopting $\rho_1 = 1$ everywhere (full material in the entire design domain). In Example 1 it is assumed that $\alpha = 3.0$, $\alpha = 1.5$ is used for Example 2, $\alpha = 2.5$ is used in Example 3, and $\alpha = 1.5$ is used for and Example 4. Geometry and boundary conditions are those presented in Figure 4.3. If not differently specified, the filter radii used in the simulations are $r_{1,f} = r_{2,f} = L/10$, for $\rho_{1,e}$ and $\rho_{2,e}$, whereas $r_{g,f} = 3 \times L/10$ is adopted for $\rho_{g,e}$. Solutions are generated by enforcing different values of $f_g \geq 0$ in the formulation of Eqn.(4.5). For each numerical investigation, the weight of the achieved optimal design is given in terms of the ratio V/V_0, where V is the weight at convergence and V_0 is the weight of the entire design domain made of full material. In the Examples below, L= 100unit length, and mean value of f= 1 unit force.

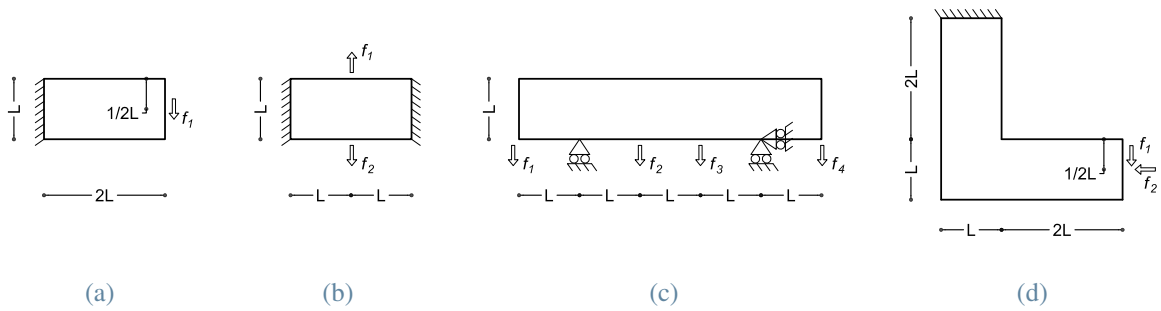

(a) (b) (c) (d)

Figure 4.3: Geometry and boundary conditions for the numerical examples

A preliminary assessment of the numerical implementation can be found in Appendix B.3 is given addressing the cantilever beam sketched in Figure 4.3a. Filter radii $r_{1,f} = r_{2,f} = L/30$ and $r_{g,f} = L/10$ are assumed in this investigation.

In the following sections, rank-2 laminates will be disregarded to focus on restricted design problems in which solid material is distributed along with graded microstructures of the type in Figure 4.1, according to [157], this may be seen as a parameterized unit cell design based on density, which provides far less flexibility than any approach involving a local optimization problem.

The effect of multiple forces will be considered. At first, optimal solutions made of solid and void will be investigated for $f_g = 0$. Then, the enforcement $f_g > 0$ will be exploited to address the design of composite elements. As already discussed in the previous chapter, the adoption of an infill with given layout and orientation is sub-optimal in terms of structural performance, but can be beneficial especially to prevent manufacturing issues.

4.3.1. Assessment of the Formulation: A Short Beam with Fixed Ends

A further assessment of the formulation considering uncertainties in the loading amplitude is given through elaborations on Example 2, as presented in Figure 4.3b. The setting $f_g = 0$ is used throughout this investigation, meaning that no porous phase is required. Assuming that two forces with deterministic amplitude $f_1 = f_2$ are applied at midspan at the top and at the bottom of the specimen, respectively, the optimal 0-1 design is that shown in Figure 4.4. It consists of a straight tie whose cross-section provides the required stiffness. The weight at convergence of this self-equilibrated solution is $V/V_0 = 0.079$.

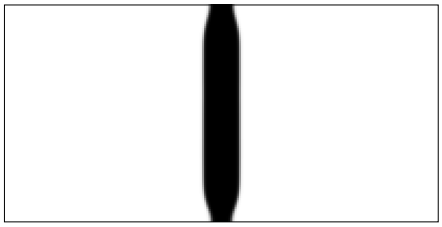

Figure 4.4: Example 2. Optimal design in case of deterministic forces, $V/V_0 = 0.079$.

Probabilistic loading is subsequently addressed, assuming that the average value for both point forces is unitary.

At first, the case of uncorrelated forces with coefficient of variations $CV_1 = CV_2 = 0.05$ is considered. The solutions found for two different values of the accepted failure probability of the displacement constraints are shown in Figure 4.5. A heavier completely constrained structure arises that can handle scenarios in which the upper and the lower forces are not equal in magnitude. To this goal, the middle vertical bar is connected to the ground by means of inclined elements converging to the corners of the design domain. Accepting a $P_{fail} = 0.01$, instead of $P_{fail} = 0.1$, does not affect the layout of the solutions, but requires a weight increase of around 25%. The setting $P_{fail} = 0.1$ will be used throughout the numerical section.

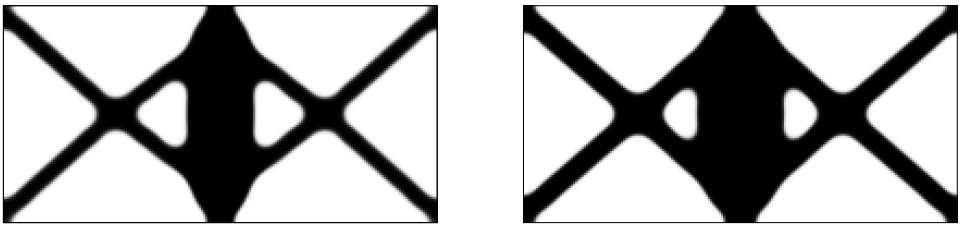

(a) $P_{fail} = 0.1$, $V/V_0 = 0.305$ (b) $P_{fail} = 0.01$, $V/V_0 = 0.384$

Figure 4.5: Example 2. Optimal design in case of uncorrelated forces for different values of the accepted failure probability ($CV_1 = CV_2 = 0.05$)

Additional investigations are performed with respect to the case of uncorrelated forces, considering different assumptions for the coefficient of variations of the magnitude of the two forces. Assuming that $CV_1 = CV_2 = 0.15$, the design represented in Figure 4.6 is achieved. The increased standard deviation calls for an heavier design with respect to that shown in Figure 4.5a, with thicker members and no inner cavity. Assuming that $CV_1 = 0.15$ and $CV_2 = 0.05$, the symmetry of the optimal solution is broken, see Figure 4.6b. Only the inclined members connecting

the load with higher variability to the ground survive in the optimal solution. As expected the relevant weight ratio is in between that of the layout found for $CV_1 = CV_2 = 0.05$ and that of the case $CV_1 = CV_2 = 0.15$.

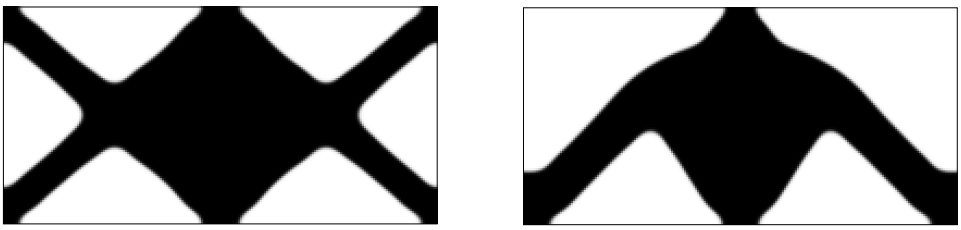

(a) $CV_1 = CV_2 = 0.15$, $V/V_0 = 0.516$ (b) $CV_1 = 0.15$, $CV_2 = 0.05$, $V/V_0 = 0.440$

Figure 4.6: Example 2. Optimal design in case of uncorrelated forces for different values of the coefficient of variation ($P_{fail} = 0.1$).

The effect of correlation is further explored considering two additional scenarios, i.e. perfectly positive correlation and perfectly negative correlation. When $r_{12} = 1$ any change in value of f_1 is exactly proportional to the change in value of f_2, occurring in the same direction. The relevant optimal design, which is represented in Figure 4.7a ($V/V_0 = 0.088$), has the same layout of the self-balanced solution depicted in Figure 4.4. With respect to the deterministic solution, the increase in weight is needed to account for the (perfectly correlated) variability of the amplitude of the two forces. When $r_{12} = -1$, the change in value of f_1 and f_2 are exactly proportional, but an increase in f_1 means a decrease in f_2 and viceversa. The optimal layout found for perfectly negative correlation is that given in Figure 4.7b. This resembles the layout found in case of uncorrelated load, see Figure 4.5a, but requires an increase in weight of around 12%.

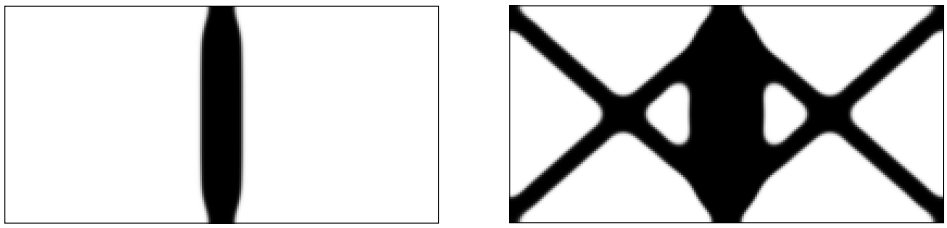

(a) $r_{12} = 1$, $V/V_0 = 0.088$ (b) $r_{12} = -1$, $V/V_0 = 0.342$

Figure 4.7: Example 2. Optimal design in case of correlated forces for different values of the correlation ($CV_1 = CV_2 = 0.05$, $P_{fail} = 0.1$).

4.3.2. Structural Response in Case of Correlated Load

Example 3 addresses the simply-supported beam with overhangs represented in Figure 4.3c. Four point forces are symmetrically applied at the lower edge of the rectangular design domain. The optimal design found for $f_g = 0$ when considering the amplitude of the forces as deterministic and equal in value is represented in Figure 4.8. Two independent structures arise around the supports, whose rotational equilibrium requires $f_1 = f_2$ and $f_3 = f_4$. No porous phase is found.

Assuming that the forces are uncorrelated, all with the same average value and coefficient of variation equal to 0.25, a completely constrained statically determinate structure arises, see Figure 4.9. The weight at convergence of this 0-1 solution is $V/V_0 = 0.497$, with an increase not far from 60% with respect to the layout found in case of deterministic loads.

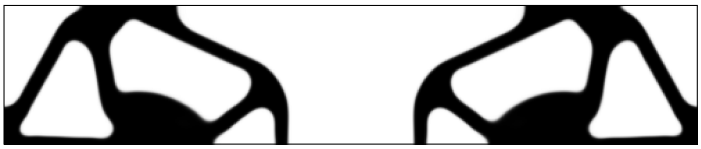

Figure 4.8: Example 3. Optimal design in case of deterministic forces, $V/V_0 = 0.315$.

Figure 4.9: Example 3. Optimal design in case of uncorrelated forces ($CV = 0.25$ for all forces, $P_{fail} = 0.1$), $V/V_0 = 0.497$.

A study was performed to check the result of four cases with four correlated forces. The results can be shown in Appendix B.4

Further numerical investigations are performed, focusing on uncorrelated forces and enforcing a minimum weight of the porous phase where $f_g = 0.25$. At first, it is assumed that the density of the porous material can range between 0.25 and 0.65, due for instance to manufacturing constraints. The optimal layouts are represented in Figure 4.10, considering the three infills introduced in Section 4.2.1, plotting maps of the overall density $\rho_{1,e} + (1-\rho_{1,e})\rho_{2,e}\rho_{g,e}$. Black regions stand for full material, i.e. $\rho_{1,e} = 1$, whereas grey scale gives information on the density

of the porous phase $0.25 \leq \rho_{g,e} \leq 0.65$. Indeed, where a porous phase arises, $\rho_{1,e} = 0$ and $\rho_{2,e} = 1$, meaning that the overall density correspond with $\rho_{g,e}$.

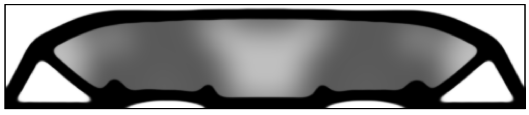

(a) Hexagonal close-packing of circular holes (HCP), $V/V_0 = 0.542$

(b) Diamond lattice (D), $V/V_0 = 0.532$

(c) Elongated diamond lattice (E) , $V/V_0 = 0.526$

Figure 4.10: Example 3. Optimal design using infill in case of uncorrelated forces ($CV = 0.25$ for all forces, $P_{fail} = 0.1$) enforcing $f_g = 0.25$ and $0.25 \leq \rho_g \leq 0.65$.

When using an isotropic microstructure consisting of an HCP arrangement of graded circular holes, the optimal design is that represented in Figure 4.10a. It consists of a coated structure, in which solid material encloses an inner region of infill whose density is not homogenously distributed. In Figure 4.10b, the optimal layout found when adopting the orthotropic diamond infill is represented. Solid material is used to build the upper and the lower chord, in addition to vertical elements that divide the layout in square bays. Some of them are completely filled with the porous phase, whereas some others are braced by inclined members oriented along the direction of maximum stiffness of the infill, i.e. $\pm 45°$ with respect to the vertical axis, see Figure 4.2. The optimal layout found in conjunction with the orthotropic elongated diamond infill is presented in Figure 4.10c. The upper and lower chord of solid material still exist, but bracing is given by elements of porous material inclined of $\pm 30°$ with respect to the vertical axis, i.e. along the direction of maximum stiffness for the adopted porous structures, see again Figure 4.2. Some connections with the lower chord are made in full material.

The enforcement of $f_g > 0$ comes with an increase in terms of the final weight with respect to the solution given in Figure 4.9 that reads 9%, 7% and 6% for the hexagonal close-packing of circular holes, the diamond lattice, and the elongated diamond lattice, respectively.

The material law in Eqn.(4.1) allows for a direct control of the minimum and maximum density of the porous phase that arise in the optimal design. Indeed this is implemented by means of side constraints in Eqn.(4.5). A further set of simulations is performed for $f_g = 0.25$, assuming

that the density of the porous material can range between 0.25 and 0.45. The achieved optimal layouts are presented in Figure 4.11. For all of them the increase in terms of weight is negligible with respect to the relevant composite structures given in Figure 4.10. The layout found for the hexagonal close-packing of circular holes is made of a solid coating, which is almost entirely filled by a region of porous material with homogenous density, see Figure 4.11a. The reduction in the maximum density of the infill calls for the adoption of solid elements crossing the porous phase to connect the chords and provide the requested stiffness to fulfill displacement constraints. Concerning the orthotropic infills, in the optimal layout of Figure 4.11b almost all the squared bays originally observed in Figure 4.10b are completely filled with porous material. The solution presented in Figure 4.11c preserves the same layout of the axes of the bracing elements already commented on when addressing Figure 4.11c, whereas the geometry of the solid elements connecting the lower chord to the inclined bar is affected by major modifications.

(a) Hexagonal close-packing of circular holes (HCP), $V/V_0 = 0.560$

(b) Diamond lattice (D), $V/V_0 = 0.529$

(c) Elongated diamond lattice (E), $V/V_0 = 0.547$

Figure 4.11: Example 3. Optimal design using infill in case of uncorrelated forces ($CV = 0.25$ for all forces, $P_{fail} = 0.1$) enforcing $f_g = 0.25$ and $0.25 \leq \rho_g \leq 0.45$

Notwithstanding the (moderate) increase in terms of weight, the adoption of composite solutions may provide peculiar advantage over a 0-1 layout, including redundancy of load pathes and high bending stiffness-to-weight ratio. In particular, the adoption of a support-free infill can solve overhang issues when manufacturing blueprints of the layout achieved through optimization via layer-by-layer 3d-printing. In the optimal solution given in Figure 4.9 several elements of the upper chords call for ad hoc supports, since their orientation with respect to the vertical axis is not compatible with the admissible overhang angle, typically $\pm 45°$. In the layouts presented in Figure 4.11, the need of additional supports is remarkably reduced and only few limited portions of the upper chord remain unsupported by the infill, see in particular Figure 4.11b and 4.11c. To avoid the arising of any unsupported region, one may leverage on the material law

in Eqn.(4.1) by specifying "passive" domains for the variable $\rho_{2,e}$, see e.g. [16]. Indeed, by setting $\rho_{2,e} = 1$ in a certain domain, either a solid phase or an infill region may arise there. In Figure 4.12 optimal layouts found prescribing passive domains in the region between the upper and lower chord are presented. Minor modifications affect the topology of the solid material, when compared to the layouts of Figure 4.11. The increase in weight to achieve this print-ready layouts is negligible with respect to the previous set of solutions.

(a) Hexagonal close-packing of circular holes (HCP), $V/V_0 = 0.563$

(b) Diamond lattice (D), $V/V_0 = 0.530$

(c) Elongated diamond lattice (E), $V/V_0 = 0.549$

Figure 4.12: Example 3. Optimal design in case of uncorrelated forces ($CV = 0.25$ for all forces, $P_{fail} = 0.1$) enforcing $f_g = 0.25$ and $0.25 \leq \rho_g \leq 0.45$, using passive regions for $\rho_{2,e}$ and an infill.

The optimal layouts represented in Figure 4.9 and Figure 4.12 are further investigated addressing their structural response in case of correlated loads. In Table 4.2, maximum values of the probability of failure for the considered displacement constraints are reported, addressing the four different cases introduced in Appendix B.4. These have been computed by entering the displacements given by Eqn.(4.5b) for different sets of density variables, and solving Eqn.(4.10) for P_{fail}. The 0-1 layout achieved in case of uncorrelated forces exceeds the reference value (0.1) by a noticeable amount in the cases B, C, and D. For composite beams this happens only in the cases B and C, thus confirming the effective structural contribution provided by the graded porous phase when dealing with the shear-dominated case D.

	case A	case B	case C	case D
0-1 design, Fig.4.9	0.078	0.128	0.214	0.140
HCP-based design, Fig.4.12a	0.100	0.125	0.240	0.101
D-based design, Fig.4.12b	0.107	0.126	0.247	0.079
E-based design, Fig.4.12c	0.108	0.125	0.245	0.087

Table 4.2: Example 3. P_{fail} computed for the optimal layouts represented in Figure 4.9 and Figure 4.12, considering different cases of correlation of the forces.

4.3.3. Mechanical Response of the Optimal Layouts in Probabilistic Terms

Example 4 is concerned with the L-shaped cantilever shown in Figure 4.3d. The specimen is fully clamped along the top edge and is subjected to a vertical force with amplitude f_1, and a horizontal one with amplitude f_2. Both are applied at the middle point of the right edge of the domain. The optimal design found for $f_g = 0$, when considering the amplitude of the two forces as deterministic and equal in value, is represented in Figure 4.13. The direction of the bar receiving the load is that of the resultant of the two forces. No other load combination can be effectively handled by such a layout. The weight at convergence is $V/V_0 = 0.479$.

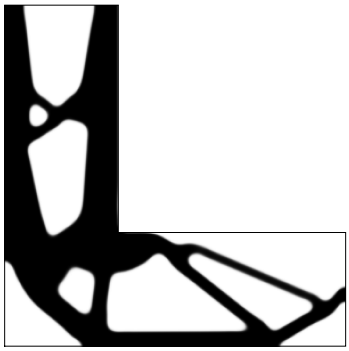

Figure 4.13: Example 4. Optimal design in case of deterministic forces, $V/V_0 = 0.479$.

Concerning probabilistic loading, two scenarios are dealt with in the numerical simulations that follow. In both cases, forces with the same average amplitude and equal coefficient of variation $CV = 0.25$ are considered. In Figure 4.14a, the optimal layout found in case of uncorrelated load is depicted, whereas Figure4.14b addresses forces with perfectly negative correlation. The former solution is heavier than the latter. The increase in weight with respect to the layout found for deterministic load is approximately 35% and 20%, respectively. Both layouts consist of a branched horizontal "beam" and a stiff corner region, but the "column" is lighter when using

$r_{12} = -1$. Indeed, the case of uncorrelated loading is expected to maximize the actions across the structure.

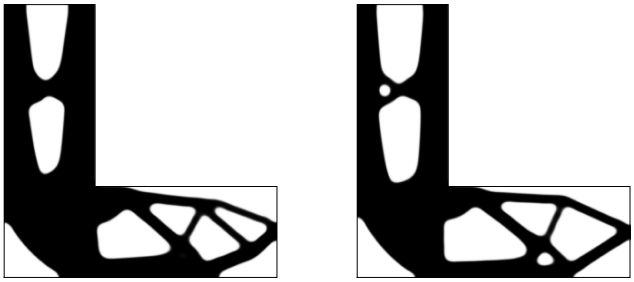

(a) Uncorrelated, $V/V_0 = 0.641$

(b) Correlated with $r_{12} = -1$, $V/V_0 = 0.572$

Figure 4.14: Example 4. Optimal design in case of forces ($CV = 0.25$ for all forces, $P_{fail} = 0.1$)

For the same probabilistic loads, optimal layouts are investigated enforcing $f_g = 0.125$ and using porous phases with density in the range $0.25 \leq \rho_g \leq 0.45$.

At first, the case of uncorrelated loads is considered, see Figure 4.15. Independently of the type of lattice that is used to design the porous phase, i) the corner region is made of full material and, ii) both in the beam and in the column, some solid elements fully or partially enclose a region of infill whose density is smoothly distributed. No additional bracing crosses the porous zones. It may be also noticed that the interface between any orthotropic infill and void is parallel to the direction of maximum stiffness of the porous material. Adopting the considered layouts, no additional support is needed within the chords to build the specimens.

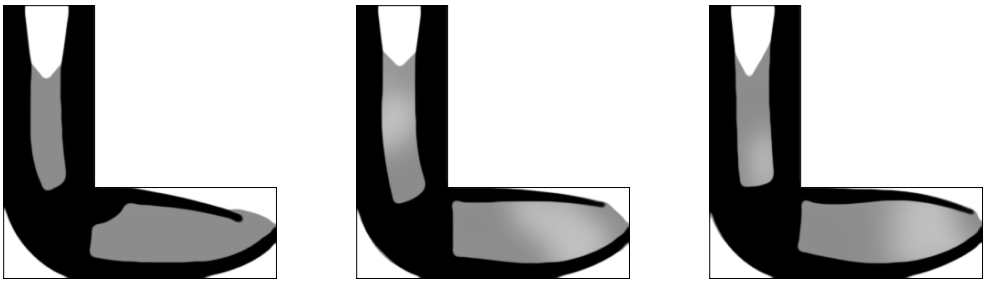

(a) Hexagonal close-packing of circular holes (HCP), $V/V_0 = 0.667$

(b) Diamond lattice (D), $V/V_0 = 0.644$

(c) Elongated diamond lattice (E) , $V/V_0 = 0.652$

Figure 4.15: Example 4. Optimal design using an infill in case of uncorrelated forces ($CV = 0.25$ for all forces, $P_{fail} = 0.1$) enforcing $f_g = 0.125$ and $0.25 \leq \rho_g \leq 0.45$.

This comes with a weight increase with respect to the solution given in Figure 4.14a equal to 4%, 1% and 2% for the hexagonal close-packing of circular holes, the diamond lattice, and the elongated diamond lattice, respectively. Although the optimal layouts represented in Figure 4.15 share a similar overall topology, minor differences remarkably affect the mechanical response of the specimens. A cross-check is performed evaluating the maximum value of P_{fail} when each one of the optimal material distributions represented in Figure 4.15 is used in conjunction with the elastic properties of the other porous microstructures. Variations in the range $10\% - 200\%$ are reported, see Table 4.3. It must be also remarked that convergence to a global minimum cannot be guaranteed for the herein addressed non-convex problem, see in particular [16] and [56]. In each row of the table, P_{fail} is minimum (and equal to 0.1) when the analysis is performed considering the material for which the layout has been designed. This confirms that, among the analysed solutions, no better local minima exists.

	Analysis performed with:		
	HCP infill	D infill	E infill
HCP-based design, Fig.4.15a	(0.100)	0.112	0.121
D-based design, Fig.4.15b	0.235	(0.100)	0.133
E-based design, Fig.4.15c	0.166	0.107	(0.100)

Table 4.3: Example 4. P_{fail} computed for the optimal material distributions represented in Figure 4.15, considering different porous microstructures.

A further set of simulations is performed accounting for the case in which perfectly negative correlation applies. The achieved optimal layouts are shown in Figure 4.16.

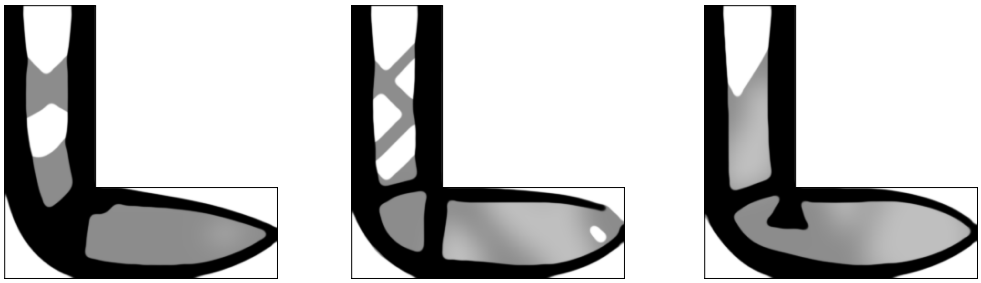

(a) Hexagonal close-packing of circular holes (HCP), $V/V_0 = 0.597$

(b) Diamond lattice (D), $V/V_0 = 0.574$

(c) Elongated diamond lattice (E) , $V/V_0 = 0.576$

Figure 4.16: Example 4. Optimal design using infill in case of correlated forces with $r_{12} = -1$ ($CV = 0.25$ for all forces, $P_{fail} = 0.1$) enforcing $f_g = 0.125$ and $0.25 \leq \rho_g \leq 0.45$.

The enforcement of $f_g > 0$ comes with an increase in terms of the final weight with respect to the solution given in Figure 4.14b that is around 4% for the hexagonal close-packing of circular holes and less than 1% for both the orthotropic lattices. The topology of the corner region is highly affected by the selected type of lattice. Full material is extensively used in the design when the hexagonal close-packing of circular holes is considered. A region of infill enclosed by solid members arises when using the diamond microstructures. A feature similar to that already seen along the lower chord of the composite design in Figure 4.12c is retrieved in the optimal solution implementing the elongated diamond infill. While the optimal design in Figure 4.16c has no cavity within the infill regions, the solutions depicted in Figure 4.16a and 4.16b present some inner voids. To get rid of these features, passive regions could be introduced for $\rho_{2,e}$, as done in Example 3. Alternatively, the value of the filter radius for $\rho_{2,e}$ is herein increased to $r_{2,f} = 3 \times L/10$. The achieved layout are those represented in Figure 4.17. As already found for the optimal solution in Figure 4.16c, no additional support is needed to manufacture the infill inside the coating. This modification has a negligible cost in terms of final weight.

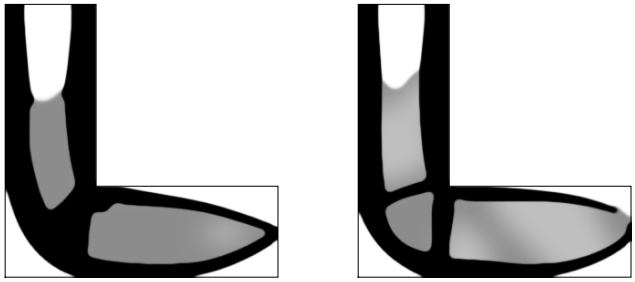

(a) Hexagonal close-packing of circular holes (HCP), $V/V_0 = 0.601$

(b) Diamond lattice (D), $V/V_0 = 0.575$

Figure 4.17: Example 4. Optimal design in case of correlated forces with $r_{12} = -1$ ($CV = 0.25$ for all forces, $P_{fail} = 0.1$) enforcing $f_g = 0.125$ and $0.25 \leq \rho_g \leq 0.45$, using $r_{2,f} = 3 \times L/10$ and an infill.

A final cross-check is operated comparing the mechanical response of the optimal layouts of Figure 4.17 and Figure 4.16c, when adopting the elastic properties of different microstructures for the same optimal distribution of minimization unknowns. As expected, the outlined differences in terms of topology remarkably affect the computed values of the probability of failure for the considered displacement constraints, see Table 4.4.

	Analysis performed with:		
	HCP infill	D infill	E infill
HCP-based design, Fig.4.17a	(0.100)	0.108	0.140
D-based design, Fig.4.17b	0.968	(0.100)	0.420
E-based design, Fig.4.16c	0.910	0.126	(0.100)

Table 4.4: Example 4. P_{fail} computed for the optimal material distributions represented in Figure 4.17 and Figure 4.16c, considering different porous microstructures.

4.4. Summary and Conclusions

A numerical method of homogenization-based topology optimization has been proposed, accounting for uncertainty in loading amplitude. Under the assumption of a joint normal distribution function to describe the uncertainty, stochastic displacement constraints can be re-written as a set of deterministic enforcements. This allows for the design of minimum weight structures for any accepted value of the probability to exceed a given displacement limit.

A two-phase material law with void has been adopted to sketch composite structures made of a solid phase and a given fraction of graded infill with a prescribed layout.

Numerical homogenization has been used to derive the macroscopic elastic constants of an isotropic and two orthotropic infills that are commonly used in additive manufacturing, i.e. an hexagonal arrangement of circular holes with high stiffness-to-weight ratio, and two self-supporting diamond lattices. Leveraging on the adopted material law, the admissible density range of the porous phase is effectively enforced by means of side constraints, whereas the optimization problem has been endowed with an additional enforcement to control the amount of graded infill to be distributed.

Simulations have been performed to assess the proposed numerical method and to highlight peculiar features of the achieved optimal solutions in case of uncorrelated or correlated forces. When the constraint prescribing a minimum fraction of infill has been disregarded, the proposed formulation has retrieved 0-1 layouts characterized by a crisp solid-void interface. It has been shown that partially constrained layouts that may arise among statically determinate solutions in case of deterministic forces are generally replaced by completely constrained ones when uncertainties are accounted for. The cases of perfect correlation should be carefully regarded, see in particular Example 2. When a fraction of graded infill has been prescribed in conjunction with low values of $\rho_{g,max}$, coated structures have been retrieved at the cost of a minor increase in terms of the overall weight. This is in agreement with the outcomes in Chapter 3, where it was

found that coated structures are effective optimal solutions when multiple loads are considered (in a deterministic framework). Sandwich structures embedding a self-supporting infill can be effectively exploited in layer-by-layer additive manufacturing to overcome overhang issues. The adoption of passive regions and a proper setting of filters have been tested as simple methods to preserve continuity of the infill, see Example 3 and 4 respectively. Numerical simulations have shown that the type of lattice to be graded remarkably affects the topology of the optimal results, as well as the structural performance in case of load uncertainties. Indeed, shape and locations of the solid features and of the infill have characteristics that are peculiar to the adopted porous microstructure.

5 | Theses, and Future Developments

In compliance with the formal requirements of the PhD dissertation, this chapter presents the outcomes of the research work. It essentially revisits the conclusions and theses related to various research areas, mirroring the summaries located at the end of Chapters 2, 3, 4.

5.1. Theses

Thesis 1

I developed a topology optimization formulation that minimizes the volume of structures subjected to multiple displacement constraints. This formulation incorporates two deflection enforcement strategies: a uniform upper bound, typical of serviceability limit states, and a variable limit that match the stiffness characteristics of a fully materialized beam.

I utilized a modified augmented Lagrangian method integrated with sequential convex programming to address the complexity of multi-constraint optimization, ensuring efficient design solutions. The formulation accommodates both fixed and distributed loads, adaptable to varying application points of static moving forces.

Related publication: [III] [i]

Thesis 2

a) I developed a multi-scale topology optimization method for lightweight structural design, utilizing numerical homogenization to assess the properties of porous materials and implementing a mixed-material approach for optimal density distribution that utilizes hexagonal close-packed arrangements of circular or spherical holes to define 2D or 3D isotropic or transversely isotropic microstructures.

b) I verified the method by achieving an optimal distribution of material density, enabling clear identification of solid and graded regions, and discussed post-processing techniques for defining component boundaries and internal structures. The approach also allows for the creation of coated structures adaptable to various loads and displacement constraints.

Related publication: [II] [ii] [b] [c]

Thesis 3

a) I proposed a numerical method of homogenization-based topology optimization, accounting for uncertainty in loading amplitude. By assuming a joint normal distribution for uncertainty and transforming probabilistic displacement constraints into deterministic enforcements, enabling the design of minimum weight structures with specific probabilities of exceeding displacement limits.

b) I derived the macroscopic elastic constants of isotropic and orthotropic infills commonly used in additive manufacturing through numerical homogenization, and I adopted a two-phase material law with void to design composite structures composed of a solid phase and a fraction of graded infill with a prescribed layout. And I proved that partially constrained layouts typically seen in deterministic forces can be replaced by completely constrained ones under uncertainty. I also found that the type of graded lattice significantly affects the topology and structural performance under load uncertainties, indicating that the shape and locations of solid features and infill in coated structures are unique to the adopted porous microstructure.

Related publication: [IV] [iii] [a] [d]

5.2. Future Development

In the future, I will emphasize the application of the proposed method to constraints on the stress field in linear elastic structures under probabilistic loading. The focus will be on formulating and validating equivalent deterministic local strength enforcements to effectively address uncertainties in loading amplitude. This will involve in-depth investigation into the behavior of structures subjected to varied and uncertain loads, aiming to enhance the reliability and safety of structural designs in the case of uncertain external forces. Broader developments should include the inclusion of buckling constraints and the extension to account for uncertainties in geometry and material properties, as well. In parallel, the proposed numerical techniques for multi-constrained optimization could be re-formulated to advance the optimization of reticulated shells and spatial trusses, employing sequential convex programming to address equilibrium and complex enforcements in structural design. Classical optimization approaches incorporating constraints to prevent yielding, buckling, and nodal instability could be conveniently aligned with specific geometric and manufacturing requirements. Additionally, the research could explore the integration of continuous optimization variables and the adaptation of discrete cross-sections suited for additive manufacturing.

Related publication: [e]

5.3. List of Publications

1. **Journal Papers:**

   I Lógó, János, and Ismail, Hussein. "Milestones in the 150 Years History of Topology Optimization: A Review." Computer Assisted Methods in Engineering and Science 27, 2–3 (2020): 97–132.

   II Bruggi, Matteo, Ismail, Hussein, Lógó, János, and Paoletti, Ingrid. "Lightweight Design With Displacement Constraints Using Graded Porous Microstructures." Computers and Structures 272 (2022): 106873.

   III Ismail, Hussein, Bruggi, Matteo, and Lógó, János. "Topology Optimization for Loads with Multiple Points of Application". Acta Polytechnica Hungarica 20, 1 (2023): 29–44.

   IV Bruggi, Matteo, Ismail, Hussein, and Lógó, János. "Topology Optimization with Graded Infill Accounting for Loading Uncertainty". Composite Structures 311 (2023): 116807.

2. **Conference Papers:**

   i Bruggi M., Ismail H., Lógó, J., Optimal design with multiple displacement constraints, 12th IEEE International Conference on Cognitive Infocommunications – CogInfoCom 2021, September 23-25, 2021 (online) Proceedings with ISBN 978-1-6654-2495-0.

   ii Ismail H., Bruggi M., Lógó, J., Multiscale Optimal Design of Grid Systems for High-rise Buildings, WEO 2021 - 2nd Workshop on Engineering Optimization, 7-8 October 2021, Warsaw, Poland (online) Proceedings with ISBN 978-83-65550-23-1.

   iii Bruggi M., Ismail H., Lógó, J., An application of multiscale topology optimization with loading uncertainty, The Fourteenth International Conference on Computational Structural Technology 23-25 August 2022, Montpellier, France, Proceedings with ISSN 2753-3239.

3. **Conference Abstracts:**

   a J. Lógó, P. Tauzowski, B. Błachowski, and H. Ismail. "Reliability-based approaches for topology optimization of elasto-plastic structures." In 25th International Congress of Theoretical and Applied Mechanics: Book of Abstracts, 2911-2912. Milan, Italy (2021). Paper: O106110-FS10. ISBN number: 978 -83-65550-31-6

b Ismail H., Lógó, J., Bruggi M., Optimal design of grid systems for tall buildings using lattice structures In: Book of abstracts of the 14th World Congress of Structural and Multidisciplinary Optimization (WCSMO-14), Colorado, US (2021) p. 44. Paper: Abstract ID: 62.

c Ismail H., Bruggi M., Lógó, J., "Integrating Porous Material in Light Weight Topology Optimization Designs." In Proceedings of Extended Abstracts 20th International Conference of Modelling in Mechanics, Technical University of Ostrava, Czech Republic (2022).

d Bruggi M., Ismail H., Lógó, J., Multi-scale topology optimization of composite beams accounting for loading uncertainty. 25th International Conference on Composite of Structures, Porto, Portugal (2022).

e Bruggi M., Ismail H., Lógó, J., Optimal design of reticulated shells accounting for strength, local buckling and overhang angles. 15th World Congress of. Structural and Multidisciplinary Optimisation, Cork, Ireland (2023).

Bibliography

[1] N. Aage, E. Andreassen, and B. S. Lazarov. Topology optimization using PETSc: An easy-to-use, fully parallel, open source topology optimization framework. *Struct. Multidiscipl. Optim.*, 51(3):565–572, Mar. 2015.

[2] W. Achtziger. *Topology Optimization of Discrete Structures*, pages 57–100. Vienna, 1997.

[3] G. Allaire, F. Jouve, and A.-M. Toader. A level-set method for shape optimization. *Comptes Rendus Mathematique*, 334(12):1125–1130, 2002.

[4] G. Allaire, C. Dapogny, R. Estevez, A. Faure, and G. Michailidis. Structural optimization under overhang constraints imposed by additive manufacturing technologies. *Journal of Computational Physics*, 351:295–328, 2017.

[5] G. Allaire, P. Geoffroy-Donders, and O. Pantz. Topology optimization of modulated and oriented periodic microstructures by the homogenization method. *Computers & Mathematics with Applications*, 78(7):2197–2229, 2019.

[6] E. Andreassen and C. S. Andreasen. How to determine composite material properties using numerical homogenization. *Computational Materials Science*, 83:488–495, 2014.

[7] E. Andreassen, A. Clausen, M. Schevenels, B. S. Lazarov, and O. Sigmund. Efficient topology optimization in Matlab using 88 lines of code. *Structural and Multidisciplinary Optimization*, 43:1–16, 2011.

[8] B. Balogh, M. Bruggi, and J. Lógó. Optimal design accounting for uncertainty in loading amplitudes: A numerical investigation. *Mechanics Based Design of Structures and Machines*, 46(5):552–566, 2018.

[9] J. Barta. On the minimum weight of certain redundant structures. *Acta Technica Academiae Scientiarum Hungaricae*, 18:67–76, 1957.

[10] A. T. Beck and W. J. de Santana Gomes. A comparison of deterministic, reliability-based and risk-based structural optimization under uncertainty. *Probabilistic Engineering Mechanics*, 28:18–29, 2012.

[11] A. Ben-Tal and A. Nemirovski. Robust truss topology design via semidefinite programming. *SIAM Journal on Optimization*, 7(4):991–1016, 1997.

[12] A. Ben-Tal and A. Nemirovski. Robust convex optimization. *Math. Oper. Res.*, 23(4): 769–805, Nov. 1998.

[13] M. P. Bendsøe. Optimal shape design as a material distribution problem. *Structural Optimization*, 1(4):193–202, Dec. 1989.

[14] M. P. Bendsøe. *Optimization of structural topology, shape, and material*. Berlin, Heidelberg, 1995.

[15] M. P. Bendsøe and O. Sigmund. Material interpolation schemes in topology optimization. *Arch. Appl. Mech.*, 69(9-10):635–654, Nov. 1999.

[16] M. P. Bendsoe and O. Sigmund. *Topology optimization: theory, methods, and applications*. 2003.

[17] M. P. Bendsøe and N. Kikuchi. Generating optimal topologies in structural design using a homogenization method. *Computer Methods in Applied Mechanics and Engineering*, 71(2):197–224, 1988.

[18] L. Berke. An efficient approach to the minimum weight design of deflection limited structures. *Rep. Air Force Flight Dynamics Lab*, 1970.

[19] L. Berke and N. Khot. *Use of optimality criteria methods for large scale systems*. Air Force Flight Dynamics Laboratory, 1974.

[20] T. Borrvall and J. Petersson. Topology optimization using regularized intermediate density control. *Computer Methods in Applied Mechanics and Engineering*, 190(37):4911–4928, 2001.

[21] B. Bourdin. Filters in topology optimization. *International Journal for Numerical Methods in Engineering*, 50(9):2143–2158, 2001.

[22] B. Bourdin and A. Chambolle. Design-dependent loads in topology optimization. *ESAIM Control Optim. Calc. Var.*, 9:19–48, Jan. 2003.

[23] A. M. Brandt. *Criteria and methods of structural optimization, PWN – Polish Sci- entific Publishers*. PWN - Polish Sci- entific Publishers, Warsaw, 1984.

[24] D. Briccola and M. Bruggi. Analysis of 3d linear elastic masonry-like structures through the api of a finite element software. *Advances in Engineering Software*, 133:60–75, 2019.

[25] M. Bruggi. On an alternative approach to stress constraints relaxation in topology optimization. *Structural and multidisciplinary optimization*, 36:125–141, 2008.

[26] M. Bruggi. Topology optimization with mixed finite elements on regular grids. *Computer Methods in Applied Mechanics and Engineering*, 305:133–153, 2016.

[27] M. Bruggi, V. Laghi, and T. Trombetti. Simultaneous design of the topology and the build orientation of wire-and-arc additively manufactured structural elements. *Computers & Structures*, 242:106370, 2021.

[28] M. Bruyneel and P. Duysinx. Note on topology optimization of continuum structures including self-weight. *Struct. Multidiscipl. Optim.*, 29(4):245–256, Apr. 2005.

[29] G. C. Calafiore and F. Dabbene. Optimization under uncertainty with applications to design of truss structures. *Struct. Multidiscipl. Optim.*, 35(3):189–200, Mar. 2008.

[30] A. Casalotti, F. D'Annibale, and G. Rosi. Multi-scale design of an architected composite structure with optimized graded properties. *Composite Structures*, 252:112608, 2020.

[31] A. S. Chan. The design of michell optimum structures. *College of Aeronautics Report*, 1960.

[32] H. S. Y. Chan. Optimal michell frameworks for three parallel forces. *College of Aeronautics Report*, 1963.

[33] H. S. Y. Chan. On Foulkes Mechanism in Portal Frame Design for Alternative Loads. *Journal of Applied Mechanics*, 36(1):73–75, 03 1969.

[34] Y. Chen, X. Peng, L. Kong, G. Dong, A. Remani, and R. Leach. Defect inspection technologies for additive manufacturing. *International Journal of Extreme Manufacturing*, 3, 01 2021.

[35] J. Chun, J. Song, and G. Paulino. Structural topology optimization under constraints on instantaneous failure probability. *Structural and Multidisciplinary Optimization*, 53, 04 2016.

[36] F. H. Cilley. The exact design of statically indeterminate frame works. an exposition of its possibility, but futility. *Transactions of the American Society of Civil Engineers*, 43 (1):353–407, 1.

[37] A. Clausen, N. Aage, and O. Sigmund. Topology optimization of coated structures and material interface problems. *Computer Methods in Applied Mechanics and Engineering*, 290:524–541, 2015.

[38] A. Clausen, N. Aage, and O. Sigmund. Exploiting additive manufacturing infill in topology optimization for improved buckling load. *Engineering*, 2(2):250–257, 2016.

[39] P. M. Clausen and O. Sigmund. The pressure load problem re-visited. In *IUTAM Symposium on Topological Design Optimization of Structures, Machines and Materials: Status and Perspectives*, pages 261–267. Springer, 2006.

[40] P. G. Coelho, P. R. Fernandes, and H. C. Rodrigues. Multiscale modeling of bone tissue with surface and permeability control. *Journal of Biomechanics*, 44(2):321–329, 2001.

[41] P. G. Coelho, J. M. Guedes, and J. B. Cardoso. Topology optimization of cellular materials with periodic microstructure under stress constraints. *Struct. Multidiscipl. Optim.*, 59(2):633–645, Feb. 2019.

[42] M. Collet, M. Bruggi, and P. Duysinx. Topology optimization for minimum weight with compliance and simplified nominal stress constraints for fatigue resistance. *Struct. Multidiscipl. Optim.*, 55(3):839–855, Mar. 2017.

[43] M. Collet, L. Noël, M. Bruggi, and P. Duysinx. Topology optimization for microstructural design under stress constraints. *Struct. Multidiscipl. Optim.*, 58(6):2677–2695, Dec. 2018.

[44] H. L. Cox. The theory of design. *Aeronautical Research*, 1958.

[45] H. L. Cox. Structures of minimum weight: the basic theory of design applied to the beam under pure bending. *Aeronautical Research*, 1958.

[46] A. Csébfalvi and J. Lógó. A critical analysis of expected-compliance model in volume-constrained robust topology optimization with normally distributed loading directions, using a minimax-compliance approach alternatively. *Advances in Engineering Software*, 120:107–115, 2018.

[47] G. da Silva and E. Cardoso. Stress-based topology optimization of continuum structures under uncertainties. *Computer Methods in Applied Mechanics and Engineering*, 313: 647–672, 2017.

[48] A. Day, K. Snyder, E. Garboczi, and M. Thorpe. The elastic moduli of a sheet containing circular holes. *Journal of the Mechanics and Physics of Solids*, 40(5):1031–1051, 1992.

[49] T. Djourachkovitch, N. Blal, N. Hamila, and A. Gravouil. Multiscale topology optimization of 3d structures: A micro-architectured materials database assisted strategy. *Computers & Structures*, 255:106574, 2021.

[50] G. Dong, Y. Tang, and Y. F. Zhao. A 149 Line Homogenization Code for Three-

Dimensional Cellular Materials Written in Matlab. *Journal of Engineering Materials and Technology*, 141(1):011005, 07 2018.

[51] D. C. Drucker and R. T. Shield. Bounds on minimum weight design. *Quart. Appl. Math.*, 15(3):269–281, 1957.

[52] P. Dunning, A. Kim, and G. Mullineux. Introducing uncertainty in direction of loading for topology optimization. In *51st AIAA/ASME/ASCE/AHS/ASC Structures, Structural Dynamics, and Materials Conference*. 2010.

[53] P. D. Dunning, H. A. Kim, and G. Mullineux. Introducing loading uncertainty in topology optimization. *AIAA Journal*, 49(4):760–768, 2011.

[54] P. Duysinx and M. P. Bendsøe. Topology optimization of continuum structures with local stress constraints. *International Journal for Numerical Methods in Engineering*, 43(8): 1453–1478, 1998.

[55] T. F. Edgar. Nonlinear programming: Theory and algorithms, 3rd edition by m.s. bazarra, h.d. sherali, and c.m. shetty. *IIE Transactions*, 40(6):627–628, 2008.

[56] H. A. Eschenauer and N. Olhoff. Topology optimization of continuum structures: A review. *Appl. Mech. Rev.*, 54(4):331–390, July 2001.

[57] J. Farkas. Theorie der einfachen ungleichungen. *Journal für die reine und angewandte Mathematik*, 124:1–27, 1902.

[58] F. Ferrari and O. Sigmund. A new generation 99 line matlab code for compliance topology optimization and its extension to 3d. *Struct. Multidiscip. Optim.*, 62(4):2211–2228, oct 2020.

[59] J. Foulkes. The minimum-weight design of structural frames. *Proceedings of the Royal Society of London. Series A, Mathematical and Physical Sciences*, 223(1155):482–494, 1954.

[60] J. Fu, H. Li, L. Gao, and M. Xiao. Design of shell-infill structures by a multiscale level set topology optimization method. *Computers & Structures*, 212:162–172, 11 2018.

[61] X. Gao, W. Chen, Y. Li, and G. Chen. Robust topology optimization of multi-material structures under load uncertainty using the alternating active-phase method. *Composite Structures*, 270:114065, 2021.

[62] O. Giraldo-Londoño and G. Paulino. Polystress: a Matlab implementation for local stress-constrained topology optimization using the augmented lagrangian method. *Structural and Multidisciplinary Optimization*, 63(4):2065–2097, Apr. 2021.

[63] O. Giraldo-Londoño and G. H. Paulino. PolyStress: a Matlab implementation for local stress-constrained topology optimization using the augmented lagrangian method. *Struct. Multidiscipl. Optim.*, 63(4):2065–2097, Apr. 2021.

[64] J. Groen and O. Sigmund. Homogenization-based topology optimization for high-resolution manufacturable micro-structures. *International Journal for Numerical Methods in Engineering*, 113(8):1148–1163, 2018.

[65] J. Guedes and N. Kikuchi. Preprocessing and postprocessing for materials based on the homogenization method with adaptive finite element methods. *Computer Methods in Applied Mechanics and Engineering*, 83(2):143–198, 1990.

[66] J. Guest, J. Prevost, and T. Belytschko. Achieving minimum length scale in topology optimization using nodal design variable and projection functions. *International Journal for Numerical Methods in Engineering*, 61:238 – 254, 09 2004.

[67] J. K. Guest and T. Igusa. Structural optimization under uncertain loads and nodal locations. *Computer Methods in Applied Mechanics and Engineering*, 198(1):116–124, 2008.

[68] B. Hassani and E. Hinton. A review of homogenization and topology optimization i—homogenization theory for media with periodic structure. *Computers & Structures*, 69(6):707–717, 1998.

[69] J. Hu, Y. Luo, and S. Liu. Two-scale concurrent topology optimization method of hierarchical structures with self-connected multiple lattice-material domains. *Composite Structures*, 272:114224, 2021.

[70] M. Jansen and O. Pierard. A hybrid density/level set formulation for topology optimization of functionally graded lattice structures. *Computers & Structures*, 231:106205, 2020.

[71] K. P. Jayachandran, J. M. Guedes, and H. C. Rodrigues. Optimal configuration of microstructure in ferroelectric materials by stochastic optimization. *Journal of Applied Physics*, 108(2), 07 2010.

[72] W. Karush. Minima of functions of several variables with inequalities as side conditions. Master's thesis, University of Chicago, Department of Mathematics, 12 1939.

[73] A. K. Kaw. *Mechanics of composite materials, second edition*. Boca Raton, FL, 2 edition, Nov. 2005.

[74] A. Kawamoto, T. Matsumori, S. Yamasaki, T. Nomura, T. Kondoh, and S. Nishiwaki.

Heaviside projection based topology optimization by a pde-filtered scalar function. *Structural and Multidisciplinary Optimization*, 44:19–24, 07 2011.

[75] G. Kazinczy. Experiments with clamped end beams. *Betonszemle*, 2:101–104, 1914.

[76] G. Kazinczy. Plastic behaviour of the materials regarding the load carrying capacity of structures. *Lecture Notes III, Hungarian Royal Academic Press*, page 13, 1942. Hungarian Royal Academic Press.

[77] C. Kim, S. Wang, I. Hwang, and J. Lee. Application of reliability-based topology optimization for microelectromechanical systems. *AIAA J.*, 45(12):2926–2934, Dec. 2007.

[78] N. Kogiso, W. Ahn, S. Nishiwaki, K. Izui, and M. Yoshimura. Robust topology optimization for compliant mechanisms considering uncertainty of applied loads. *Journal of Advanced Mechanical Design Systems and Manufacturing - J ADV MECH DES SYST MANUF*, 2:96–107, 03 2008.

[79] R. S. Kumar and D. L. McDowell. Generalized continuum modeling of 2-d periodic cellular solids. *International Journal of Solids and Structures*, 41(26):7399–7422, 2004.

[80] B. Lazarov, M. Schevenels, and O. Sigmund. Topology optimization considering material and geometric uncertainties using stochastic collocation methods. *Structural and Multidisciplinary Optimization*, 46(4):597–612, 2012.

[81] B. S. Lazarov, F. Wang, and O. Sigmund. Length scale and manufacturability in density-based topology optimization. *Arch. Appl. Mech.*, 86(1-2):189–218, Jan. 2016.

[82] J. Lee and N. Kikuchi. Structural topology optimization of electrical machinery to maximize stiffness with body force distribution. *IEEE Trans. Magn.*, 46(10):3790–3794, Oct. 2010.

[83] J. Lee, J. H. Seo, and N. Kikuchi. Topology optimization of switched reluctance motors for the desired torque profile. *Structural and multidisciplinary optimization*, 42:783–796, 2010.

[84] T. Lewiński and G. Rozvany. Exact analytical solutions for some popular benchmark problems in topology optimization iii: L-shaped domains. *Structural and Multidisciplinary Optimization*, 35(2):165–174, 2008.

[85] T. Lewiński, M. Zhou, and G. I. N. Rozvany. Extended exact solutions for least-weight truss layouts—part i: Cantilever with a horizontal axis of symmetry. *Int. J. Mech. Sci.*, 36(5):375–398, May 1994.

[86] T. Lewiński, T. Sokół, and C. Graczykowski. *Michell Structures*. Springer International Publishing, 2018.

[87] J. Liu, A. Gaynor, S. Chen, Z. Kang, K. Suresh, A. Takezawa, L. Li, J. Kato, J. Tang, C. Wang, L. Cheng, X. Liang, and A. To. Current and future trends in topology optimization for additive manufacturing. *Structural and Multidisciplinary Optimization*, 57 (6):2457–2483, 2018. ISSN 1615-147X.

[88] K. Liu and A. Tovar. An efficient 3D topology optimization code written in Matlab. *Struct. Multidiscipl. Optim.*, 50(6):1175–1196, Dec. 2014.

[89] I. Lochner-Aldinger and A. Schumacher. Homogenization method: Distribution of material densities. *Shell Structures for Architecture: Form Finding and Optimization*, pages 211–223, 2014.

[90] J. Lógó. New type of optimality criteria method in case of probabilistic loading conditions. *Mechanics Based Design of Structures and Machines*, 35(2):147–162, 2007.

[91] J. Lógó. Simp type topology optimization procedure considering uncertain load position. *Periodica Polytechnica Civil Engineering*, 56:213–219, 2012.

[92] J. Lógó, M. Ghaemi, and A. Vásárhelyi. Stochastic compliance constrained topology optimization based on optimality critera method. *Periodica Polytechnica Civil Engineering*, 51(2):5–10, 2007.

[93] J. Lógó, M. Ghaemi, and M. M. Rad. Optimal topologies in case of probabilistic loading: The influence of load correlation. *Mechanics Based Design of Structures and Machines*, 37(3):327–348, 2009.

[94] J. Lógó, B. Balogh, and E. Pintér. Topology optimization considering multiple loading. *Computers and Structures*, 207:233–244, 2018. doi: https://doi.org/10.1016/j.compstruc.2017.03.018.

[95] K. Marti. *Stochastic optimization methods*. Springer, New York, NY, Jan. 2005.

[96] K. Maute and D. M. Frangopol. Reliability-based design of MEMS mechanisms by topology optimization. *Comput. Struct.*, 81(8-11):813–824, May 2003.

[97] J. C. Maxwell. I.—on reciprocal figures, frames, and diagrams of forces. *Earth and Environmental Science Transactions of The Royal Society of Edinburgh*, 26(1):1–40, 1870.

[98] E. Melan. Theorie statisch unbestimmter systeme. In *Prelim. Publ. 2nd Congress Int. Ass. Bridge Struct. Eng. Berlin*, pages 43–64. 1936.

[99] R. E. Melchers. On extending the range of michell-like optimal topology structures. *Struct. Multidiscipl. Optim.*, 29(2):85–92, Feb. 2005.

[100] L. Meng, W. Zhang, D. Quan, G. Shi, L. Tang, Y. Hou, P. Breitkopf, J. Zhu, and T. Gao. From topology optimization design to additive manufacturing: Today's success and tomorrow's roadmap. *Archives of Computational Methods in Engineering*, 27:805–830, 2020.

[101] A. G. M. Michell. LVIII. The limits of economy of material in frame-structures. *The London, Edinburgh, and Dublin Philosophical Magazine and Journal of Science*, 8(47): 589–597, 1904. doi: 10.1080/14786440409463229.

[102] H. P. Mlejnek. Some aspects of the genesis of structures. *Structural Optimization*, 5 (1-2):64–69, Mar. 1992.

[103] Z. Mróz. On a problem of minimum weight design. *Quarterly of Applied Mathematics*, 19:1, 05 1960. doi: 10.1090/qam/135327.

[104] J. Nagtegaal and W. Prager. Optimal layout of a truss for alternative loads. *International Journal of Mechanical Sciences*, 15(7):583–592, 1973.

[105] J. Neyman, editor. *Proceedings of the Second Berkeley Symposium on Mathematical Statistics and Probability, Nonlinear Programming*, volume 2, Statistical Laboratory of the University of California, Berkeley, 1951. H. W. Kuhn, A. W. Tucker.

[106] S. Nishiwaki, M. I. Frecker, S. Min, and N. Kikuchi. Topology optimization of compliant mechanisms using the homogenization method. *International Journal for Numerical Methods in Engineering*, 42(3):535–559, 1998.

[107] B. Niu and E. Wadbro. On equal-width length-scale control in topology optimization. *Struct. Multidiscipl. Optim.*, 59(4):1321–1334, Apr. 2019.

[108] B. Niu and E. Wadbro. Multiscale design of coated structures with periodic uniform infill for vibration suppression. *Computers & Structures*, 255:106622, 2021.

[109] N. Olhoff and J. Du. *Structural Topology Optimization with Respect to Eigenfrequencies of Vibration*, pages 275–297. Vienna, 2014.

[110] A. Panesar, M. Abdi, D. Hickman, and I. Ashcroft. Strategies for functionally graded lattice structures derived using topology optimisation for additive manufacturing. *Additive Manufacturing*, 19:81–94, 2018.

[111] G. Papanicolau, A. Bensoussan, and J. Lions. *Asymptotic Analysis for Periodic Structures*. Elsevier Science, 1978.

[112] V. Pareto. *Cours d'économie politique*. Droz, Genéve, 1896.

[113] D. Pasini and J. Guest. Imperfect architected materials: Mechanics and topology optimization. *MRS Bulletin*, 44:766–772, 10 2019.

[114] E. Pintér, A. Lengyel, and J. Lógó. Structural topology optimization with stress constraint considering loading uncertainties. *Period. Poly. Civ. Eng.*, 59(4):559–565, 2015.

[115] J. Plocher and A. Panesar. Review on design and structural optimisation in additive manufacturing: Towards next-generation lightweight structures. *Materials & Design*, 183:108164, 2019.

[116] W. Prager. Optimization of structural design. *J. Optim. Theory Appl.*, 6(1):1–21, July 1970.

[117] W. Prager. Foulkes mechanism in optimal plastic design for alternative loads. *International Journal of Mechanical Sciences*, 13(11):971–973, 1971.

[118] W. Prager and G. I. N. Rozvany. Optimal layout of grillages. *Journal of Structural Mechanics*, 5(1):1–18, 1977.

[119] W. Prager and R. Shield. Optimal design of multi-purpose structures. *International Journal of Solids and Structures*, 4(4):469–475, 1968.

[120] W. Prager and J. E. Taylor. Problems of Optimal Structural Design. *Journal of Applied Mechanics*, 35(1):102–106, 03 1968.

[121] A. Prékopa. *Stochastic Programming*. Budapest, Dordrecht: Akadémia Kiadő and Kluwer, 1995.

[122] M. Rashki, M. Miri, and M. A. Moghaddam. A simulation-based method for reliability based design optimization problems with highly nonlinear constraints. *Autom. Constr.*, 47:24–36, Nov. 2014.

[123] H. Rodrigues, J. M. Guedes, and M. Bendsoe. Hierarchical optimization of material and structure. *Structural and Multidisciplinary Optimization*, 24:1–10, 2002.

[124] M. P. Rossow and J. E. Taylor. A finite element method for the optimal design of variable thickness sheets. *AIAA Journal*, 11(11):1566–1569, 1973.

[125] G. I. N. Rozvany. Some shortcomings in michell's truss theory. *Structural Optimization*, 12(4):244–250, Dec. 1996.

[126] G. I. N. Rozvany. *Structural design via optimality criteria*. Mechanics of Elastic and Inelastic Solids. Springer, Dordrecht, Netherlands, 1989 edition, Dec. 2012.

[127] W. S. Hemp. Theory of structural design. Technical Report 214, NATO Studies, Paris, 1958.

[128] L. A. Schmit. Structural design by systematic synthesis. In *Proceeding 2nd ASCE Conference on Electronic Computation*, pages 105–132. Royal Society of Edinburgh Scotland Foundation, 1960.

[129] A. Schumacher and C. Olschinka. Robust design considering highly nonlinear structural behavior. *Struct. Multidiscipl. Optim.*, 35(3):263–272, Mar. 2008.

[130] Y. L. Shengfang Zhang, Jian Yin. Structural topology optimization of brake disc using the equivalent moving load method. *Journal of Engineering and Technological Sciences*, 51(6):791–804, 2019.

[131] R. T. Shield. Optimum design methods for multiple loading. *Z. Angew. Math. Phys.*, 14 (1):38–45, 1963.

[132] R. T. Shield. Optimum design of structures through variational principles. In *Optimization and Stability Problems in Continuum Mechanics*, pages 13–37. Springer Berlin Heidelberg, Berlin, Heidelberg, 2008.

[133] J. Sienz and E. Hinton. Reliable structural optimization with error estimation, adaptivity and robust sensitivity analysis. *Comput. Struct.*, 64(1-4):31–63, July 1997.

[134] O. Sigmund. A new class of extremal composites. *Journal of the Mechanics and Physics of Solids*, 48(2):397–428, 2000.

[135] O. Sigmund. A 99 line topology optimization code written in matlab. *Structural and Multidisciplinary Optimization*, 21:120–127, 04 2001.

[136] O. Sigmund and S. Torquato. Design of materials with extreme thermal expansion using a three-phase topology optimization method. *Journal of the Mechanics and Physics of Solids*, 45(6):1037–1067, 1997.

[137] O. Sigmund, N. Aage, and E. Andreassen. On the (non-)optimality of michell structures. *Struct. Multidiscipl. Optim.*, 54(2):361–373, Aug. 2016.

[138] G. Silva and A. Beck. Reliability-based topology optimization of continuum structures subject to local stress constraints. *Structural and Multidisciplinary Optimization*, 57, 06 2018.

[139] R. Sivapuram, P. Dunning, and H. A. Kim. Simultaneous material and structural optimization by multiscale topology optimization. *Structural and Multidisciplinary Optimization*, 54:1267–1281, 11 2016.

[140] N. J. A. Sloane and J. H. Conway. *Sphere Packings, Lattices and Groups*. New York, 1999.

[141] J. Sokolowski and A. Zochowski. On the topological derivative in shape optimization. *SIAM Journal on Control and Optimization*, 37(4):1251–1272, 1999.

[142] S. Sotiropoulos, G. Kazakis, and N. D. Lagaros. Conceptual design of structural systems based on topology optimization and prefabricated components. *Computers & Structures*, 226:106136, 2020.

[143] J. Stegmann and E. Lund. Discrete material optimization of general composite shell structures. *International Journal for Numerical Methods in Engineering*, 62(14):2009–2027, 2005.

[144] K. Suzuki and N. Kikuchi. A homogenization method for shape and topology optimization. *Computer Methods in Applied Mechanics and Engineering*, 93(3):291–318, 1991. ISSN 0045-7825.

[145] K. Svanberg. The method of moving asymptotes—a new method for structural optimization. *International Journal for Numerical Methods in Engineering*, 24(2):359–373, 1987.

[146] G. Sved. The minimum weight of certain redundant structures. *Australian Journal of Applied Sciences*, 5:1–9, 1954.

[147] C. R. Thomsen, F. Wang, and O. Sigmund. Buckling strength topology optimization of 2d periodic materials based on linearized bifurcation analysis. *Computer Methods in Applied Mechanics and Engineering*, 339:115–136, 2018.

[148] M. Valdebenito and G. Schuëller. A survey on approaches for reliability-based optimization. *Structural and Multidisciplinary Optimization*, 42:645–663, 11 2010.

[149] S. Vigdergauz. Two-Dimensional Grained Composites of Extreme Rigidity. *Journal of Applied Mechanics*, 61(2):390–394, 06 1994.

[150] T. Vrouwenvelder. The jcss probabilistic model code. *Structural Safety*, 19(3):245–251, 1997.

[151] E. Wadbro and B. Niu. Multiscale design for additive manufactured structures with solid coating and periodic infill pattern. *Computer Methods in Applied Mechanics and Engineering*, 357:112605, 2019.

[152] C. Wang, W. Zhang, L. Zhou, T. Gao, and J. Zhu. Topology optimization of self-

supporting structures for additive manufacturing with b-spline parameterization. *Computer Methods in Applied Mechanics and Engineering*, 374:113599, 2021.

[153] F. Wang, B. Lazarov, and O. Sigmund. On projection methods, convergence and robust formulations in topology optimization. *Structural and Multidisciplinary Optimization*, 43:767–784, 06 2011.

[154] M. Y. Wang, X. M. Wang, and D. M. Guo. A level set method for structural topology opti- mization. *Computer Methods in Applied Mechanics and Engineering*, 192(1-2): 227–246, 2003.

[155] S. Wang and K. Tai. Graph representation for structural topology optimization using genetic algorithms. *Computers & Structures*, 82(20):1609–1622, 2004. ISSN 0045-7949.

[156] Y. Wang, H. Xu, and D. Pasini. Multiscale isogeometric topology optimization for lattice materials. *Computer Methods in Applied Mechanics and Engineering*, 316:568–585, 2017.

[157] J. Wu, O. Sigmund, and J. P. Groen. Topology optimization of multi-scale structures: a review. *Structural and Multidisciplinary Optimization*, 63:1455 – 1480, 2021.

[158] Y. Xie and G. Steven. A simple evolutionary procedure for structural optimization. *Computers & Structures*, 49(5):885–896, 1993.

[159] L. Xu and Z. Qian. Topology optimization and de-homogenization of graded lattice structures based on asymptotic homogenization. *Composite Structures*, 277:114633, 2021.

[160] B. Yi, G. H. Yoon, and X. Peng. A simple density filter for the topology optimization of coated structures. *Engineering Optimization*, 53(12):2088–2107, 2021.

[161] G. H. Yoon and B. Yi. A new coating filter of coated structure for topology optimization. *Struct. Multidiscipl. Optim.*, 60(4):1527–1544, Oct. 2019.

[162] K.-I. Ypsilantis, G. Kazakis, and N. Lagaros. An efficient 3d homogenization-based topology optimization methodology. *Computational Mechanics*, 67:481–496, 02 2021.

[163] Z. Zeng and F. Ma. An efficient gradient projection method for structural topology optimization. *Advances in Engineering Software*, 149:102863, 2020.

[164] Y. Zheng, D. Da, H. Li, M. Xiao, and L. Gao. Robust topology optimization for multi-material structures under interval uncertainty. *Applied Mathematical Modelling*, 78:627–647, 2020.

[165] M. Zhou and G. Rozvany. The coc algorithm, part ii: Topological, geometrical and generalized shape optimization. *Computer Methods in Applied Mechanics and Engineering*, 89(1):309–336, 1991.

[166] M. Zhou and G. I. N. Rozvany. The COC algorithm, part II: Topological, geometrical and generalized shape optimization. *Comput. Methods Appl. Mech. Eng.*, 89(1-3):309–336, Aug. 1991.

[167] B. Zhu, X. Zhang, H. Zhang, J. Liang, H. Zang, H. Li, and R. Wang. Design of compliant mechanisms using continuum topology optimization: A review. *Mechanism and Machine Theory*, 143:103622, 2020.

[168] R. H. Zuberi, Z. Zhengxing, L. Kai, and L. Wen. Topological optimization of constant beam section under moving load condition". In *2010 International Conference on Mechanic Automation and Control Engineering*, pages 354–359. 2010.

List of Figures

1.1 Simple tension structures by Cox. 5
1.2 The development of the optimal solutions 6
1.3 The exact optimal solution by Lewiński, Zhou and Rozvany [85]. 8
1.4 The exact optimal solution of the L-shape beam by Lewiński and Rozvany [84]. 9
1.5 The pressure load solution by Clausen and Sigmund [39]. 9

2.1 Cantilever beam examples 23
2.2 Cantilever beam: optimal design considering a force applied at the tip ($v_f = 0.50$). 24
2.3 Cantilever beam with a uniform distributed load 24
2.4 Deformed shapes of the layouts achieved considering a uniformly distributed load 24
2.5 Deformed shapes of the minimum compliance layouts 25
2.6 Cantilever beam subjected to moving load 26
2.7 Single Span Beam: Initial problems 26
2.8 Simply supported beam 27
2.9 Hinged beam layout 28
2.10 Two Span Beam: Initial Problems 29
2.11 Two-span beam with uniformly distributed load 29
2.12 Two-span beam with a moving vertical force-1 30
2.13 Two-span beam with a moving vertical force-2 30

3.1 2D version of HCP 35
3.2 Interpolation laws fitting results 36
3.3 3D version of HCP 36
3.4 3D view of a single base cell. 37
3.5 Interpolation laws fitting results, 3D 38
3.6 Test specimens fabricated by means FDM 42
3.7 Geometry and boundary conditions for the two-dimensional numerical examples 43
3.8 Geometry and boundary conditions for the three-dimensional numerical example 43
3.9 Example 1, $f_g = 0$ 44
3.10 Example 1, $f_g > 0$ 44

3.11 Example 1, $f_g = 0.05$ 45
3.12 Example 1, HCP final layout 46
3.13 Example 1. including control on the horizontal displacement 48
3.14 Example 2. Optimal design for $f_g = 0$ 48
3.15 Example 2. Optimal design. 49
3.16 Example 2. History plot of the scaled objective function 50
3.17 Example 2. Design for $f_g = 0.15$, $d = L/12$ 51
3.18 Example 2. optimal design for $f_g = 0.15$, $d = L/16$, ... 51
3.19 Example 2. Optimal design with $\rho_{g,min} = 0.45$ 52
3.20 3D optimal design for $f_g = 0$ 53
3.21 3D optimal design for $f_g = 0.10$ 54
3.22 3D optimal design history plot 55

4.1 Base cells 59
4.2 Apparent Young's modulus of the base cells 60
4.3 Examples geometry 65
4.4 Example 2. Optimal design in case of deterministic forces 66
4.5 Example 2. Optimal design in case of uncorrelated forces-1 66
4.6 Example 2. Optimal design in case of uncorrelated forces-2 67
4.7 Example 2. Optimal design in case of uncorrelated forces-3 67
4.8 Example 3. Optimal design in case of deterministic forces 68
4.9 Example 3. Optimal design in case of uncorrelated forces 68
4.10 Example 3. Optimal design using infill in case of uncorrelated forces-1 69
4.11 Example 3. Optimal design using infill in case of uncorrelated forces-2 70
4.12 Example 3. Optimal design using infill in case of uncorrelated forces-3 71
4.13 Example 4. Optimal design in case of deterministic forces 72
4.14 Example 4. Optimal design in case of probabilistic loading 73
4.15 Example 4. Optimal design using an infill 73
4.16 Example 4. Optimal design using infill in case of correlated forces 74
4.17 Example 4. Optimal design in case of correlated forces with $r_{12} = -1$ 75

A.1 Dependence of the Young modulus on the direction 101
A.2 Example 3. Optimal designs-1. 105
A.3 Example 3. Optimal designs-2. 106
A.4 Example 3. Overlay of the HPC circular holes 106
A.5 Optimal design with $\rho_{g,min} = 0.45$ 107

B.1 Example 1. Optimal design in case of a deterministic force 110

B.2 Example 1. Optimal design in case of a force f_1 with $CV_1 = 0.15$ 111
B.3 Optimal design using the code in [157] 112
B.4 Example 3. Optimal design in case of correlated forces for different values of the correlation 113

List of Tables

3.1 Multi-scale design vs. full-scale finite element analysis of the blueprints: values of the maximum deflection under the loaded points v^{max} (mm). 47

4.1 Interpolation law of the type $\alpha_i x^i$, with $i = 1, 2, ..., 5$, for the components of the macroscopic stiffness tensor given in Eqn.(4.2), as computed for an hexagonal close-packing of circular holes (HCP), a diamond lattice (D) and an elongated diamond lattice (E), using numerical homogenization. 60

4.2 Example 3. P_{fail} computed for the optimal layouts represented in Figure 4.9 and Figure 4.12, considering different cases of correlation of the forces. 72

4.3 Example 4. P_{fail} computed for the optimal material distributions represented in Figure 4.15, considering different porous microstructures. 74

4.4 Example 4. P_{fail} computed for the optimal material distributions represented in Figure 4.17 and Figure 4.16c, considering different porous microstructures. . . 76

A | Appendix A

A.1. 3D Isotropic behavior of HCP

Focusing on a transversally isotropic material with the axis of symmetry which is that characterized by the index 3, the components of the stress tensor may be derived from those of the strain tensor as:

$$\begin{bmatrix} \sigma_{11} \\ \sigma_{22} \\ \sigma_{33} \\ \sigma_{13} \\ \sigma_{23} \\ \sigma_{12} \end{bmatrix} = \begin{bmatrix} C_{11} & C_{12} & C_{13} & 0 & 0 & 0 \\ & C_{11} & C_{13} & 0 & 0 & 0 \\ & & C_{33} & 0 & 0 & 0 \\ & & & C_{44} & 0 & 0 \\ & \text{syms} & & 0 & C_{44} & 0 \\ & & & 0 & 0 & \frac{1}{2}(C_{11}-C_{12}) \end{bmatrix} \begin{bmatrix} \varepsilon_{11} \\ \varepsilon_{22} \\ \varepsilon_{33} \\ 2\varepsilon_{13} \\ 2\varepsilon_{23} \\ 2\varepsilon_{12} \end{bmatrix}, \tag{A.1}$$

where C_{11}, C_{12}, C_{13}, C_{33}, C_{44} are five independents elastic constants. For the graded porous microstructure described in Section 3.1.1.2, a deviation from the isotropic behavior can be appreciated only for low material densities. Figure A.1 shows dependence of the Young modulus on the direction, for two different values of the density. Colour, as well as distance of the surface points from the center, represents E/E_0 along the corresponding direction. For $\rho_g = 0.62$, Figure A.1a, a sphere is found, whereas some minor deviation arises for $\rho_g = 0.33$, due to an increased stiffness at the poles along the y_3-axis, Figure A.1b. The above results suggest the adoption of the isotropic material model as a reasonable approximation to handle the three-dimensional porous microstructure in the multi-scale approach of topology optimization. To avoid overestimating the elastic constants, the shear modulus G is computed from C_{44}, whereas the bulk modulus K from C_{11}, i.e. assuming that $G(\rho_g) = C_{44}(\rho_g)$ and $K(\rho_g) = C_{11}(\rho_g) - 4G(\rho_g)/3$.

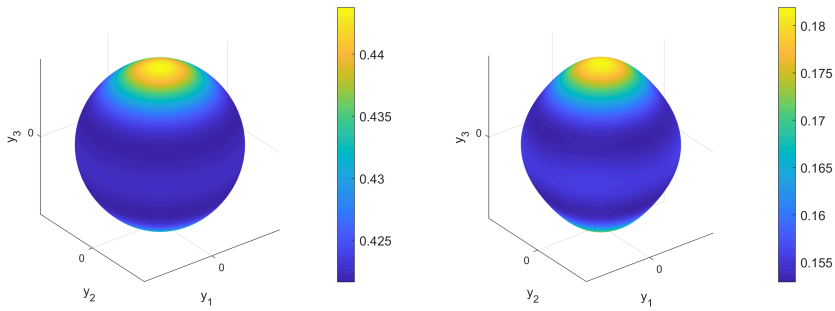

(a) $\rho_g = 0.62$ (b) $\rho_g = 0.33$

Figure A.1: 3D version of the porous microstructure: dependence of the Young modulus on the direction (colour, as well as distance of the surface points from the center, represents E/E_0 in the corresponding direction)

A.2. Filtering

In the whole work, a standard linear filter [20, 21] is implemented on the element variables ρ_e to avoid potential issues that are well-known in topology optimization, i.e. the arising of mesh dependence and checkerboard patterns. With reference to the problem in Chapter 3, the original variables ρ_e and $\rho_{g,e}$ are mapped to the new sets $\tilde{\rho}_e$ and $\tilde{\rho}_{g,e}$ as follows:

$$\tilde{\rho}_e = \frac{1}{\sum_n H_{es}} \sum_n H_{es}\, \rho_e, \quad \tilde{\rho}_{g,e} = \frac{1}{\sum_n H_{es}} \sum_n H_{es}\, \rho_{g,e} \tag{A.2a}$$

$$H_{es} = \max(0, r_f - \mathrm{dist}(e,s)), \quad H_{g,es} = \max(0, r_{g,f} - \mathrm{dist}(e,s)) \tag{A.2b}$$

$$\tag{A.2c}$$

where $\mathrm{dist}(e,s)$ is the distance between the centroid of the e-th and s-th element, whereas r_f and $r_{g,f}$ are the filter radius used for ρ_e and $\rho_{g,e}$, respectively.

Then, the filtered densities $\tilde{\rho}_e$ are mapped to the set of projected (physical) densities $\widehat{\rho}_e$ in order to achieve 0-1 solutions, i.e. a clear separation between full material and porous material or void. The formulation proposed in [153] is herein adopted:

$$\widehat{\rho}_e = \frac{\tanh(\beta\eta) + \tanh(\beta(\tilde{\rho}_e - \eta))}{\tanh(\beta\eta) + \tanh(\beta(1-\eta)}, \tag{A.3}$$

with threshold $\eta = [0,1]$ and sharpness factor $\beta = [1,\infty]$. The Heaviside function projects densities below the threshold to 0 and densities above it to 1, depending on the value of the sharpness factor, see e.g. [66, 74]. In the numerical section $\eta = 0.5$, whereas β is smoothly

increased during the simulations from 2 to 16 by means of the continuation approach in [58].

To enforce the lower bound $\rho_{g,min}$ without jeopardizing the arising of the void phase, filtered densities $\tilde{\rho}_{g,e}$ are mapped to a set of projected densities $\widehat{\rho}_{g,e}$, along the line of the approach proposed by [64], see also [70]. One has:

$$\widehat{\rho}_{g,e} = \tilde{\rho}_{g,e} \frac{\tanh(\beta_g \rho_{g,min}) + \tanh(\beta_g(\tilde{\rho}_{g,e} - \rho_{g,min}))}{\tanh(\beta_g \rho_{g,min}) + \tanh(\beta_g(1 - \rho_{g,min})}, \tag{A.4}$$

with threshold $\rho_{g,min}$ and sharpness factor $\beta_g = [1, \infty]$. The Heaviside function scales $\tilde{\rho}_{g,e}$ such that densities below the threshold are projected to 0, whereas densities above remain unchanged. The sharpness factor β_g is smoothly increased during the simulations using the same continuation approach already introduced for β.

When dealing with the design of the optimal infill for a specimen with given external boundaries, no projection is needed on $\widehat{\rho}_{g,e}$.

A.3. Solving Algorithm

The optimization problems handled in this work, as it is for Eqn.(3.11), are solved via sequential convex programming, adopting the Method of Moving Asymptotes (MMA) as minimizer. The displacement constraints in Eqn.(3.11c) and the weight constraint in Eqn.(3.11d) are handled by means of an augmented Lagrangian (AL) approach, similarly to what implemented in [62] for minimum weight problems with local stress constraints.

Among the successful applications of MMA, the design of compliant mechanisms involves the non-trivial control of displacement components other than those involved in the definition of the work of the external forces at equilibrium, see in particular [167]. Although the simulations presented address at most a few hundreds of local enforcements, the AL method has been selected to speed up the computations of the basic MMA.

Both the constraints in Eqn.(3.11c) and Eqn.(3.11d) can be written in the form:

$$h_l / h_{lim,l} \leq 1, \tag{A.5}$$

where $h_{lim,l}$ is the upper bound of h_l in the l-th enforcement.

At the k-th AL step, an unconstrained problem is considered whose objective function reads:

$$\mathscr{W} + \frac{1}{m+1}\sum_{l=1}^{m+1}\left(a_l^{(k)}q_l + \frac{b^{(k)}}{2}q_l^2\right), \quad \text{with} \quad q_l = \max\left(\frac{h_l}{h_{lim,l}}, -\frac{a_l^{(k)}}{b^{(k)}}\right), \tag{A.6}$$

where $a_l^{(k)}$ is the l-th entry of the vector $\mathbf{a}^{(k)}$ of the lagrangian multiplier estimators, and $b^{(k)} > 0$ is a penalty factor. The function in Eqn.(A.6) is normalized with respect to the number of constraints, namely $m+1$, to avoid the added term prevail over W.

Following [62], MMA is used to cope with the unconstrained minimization of the normalized function in Eqn.(A.6), which is in turn adopted to update the current values of the lagrangian multiplier estimators and penalty factor for the $(k+1)$-th step. One has:

$$a_l^{(k+1)} = a_l^{(k)} + b^{(k)}q_l \quad \text{and} \quad b^{(k+1)} = \min\left(\alpha b^{(k)}, b_{max}\right), \tag{A.7}$$

where $\alpha > 1$ is an update parameter and b_{max} an upper bound against numerical issues. In the numerical simulations, the same input parameters given in [62] are used.

The overall process is repeated until convergence is achieved, i.e. the maximum difference in terms of the values of the set of minimization unknowns ρ_e and $\rho_{g,e}$ between two subsequent steps is less than 10^{-3}.

The adjoint method is used to compute sensitivity and run the gradient-based minimizer, see Appendix A.4.

A.4. Sensitivity

The sensitivity of the objective function and of the constraints in Eqn.(3.11) are computed through the adjoint method, see e.g. [16]. Accordingly, u_i in Eqn.(3.11c) does not change when adding at the right hand side a zero function derived from the equilibrium of Eqn.(3.11b):

$$-\boldsymbol{\lambda}_i^T\left(\mathbf{K}(\boldsymbol{\rho},\boldsymbol{\rho_g})\mathbf{U}_j - \mathbf{F}_j(\boldsymbol{\rho},\boldsymbol{\rho_g})\right), \tag{A.8}$$

where $\boldsymbol{\lambda}_i$ is any arbitrary but fixed vector and $\mathbf{F}_j = \mathbf{F}_j(\boldsymbol{\rho},\boldsymbol{\rho_g})$, i.e. the case of design-dependent loads such as self-weight, is considered. The derivative of u_i with respect to the element unknown ρ_s, which can be indifferently an entry either of $\boldsymbol{\rho}$ or of $\boldsymbol{\rho_g}$, may be computed as:

$$\frac{\partial u_i}{\partial \rho_s} = \boldsymbol{L}_i^T\frac{\partial \mathbf{U}_j}{\partial \rho_s} - \boldsymbol{\lambda}_i^T\frac{\partial \mathbf{K}(\boldsymbol{\rho},\boldsymbol{\rho_g})}{\partial \rho_s}\mathbf{U}_j - \boldsymbol{\lambda}_i^T\mathbf{K}(\boldsymbol{\rho},\boldsymbol{\rho_g})\frac{\partial \mathbf{U}_j}{\partial \rho_s} + \boldsymbol{\lambda}_i^T\frac{\partial \mathbf{F}_j(\boldsymbol{\rho},\boldsymbol{\rho_g})}{\partial \rho_s}. \tag{A.9}$$

After re-arrangement of terms, one has:

$$\frac{\partial u_i}{\partial \rho_s} = \left(\boldsymbol{L}_i^T - \boldsymbol{\lambda}_i^T \mathbf{K}(\boldsymbol{\rho}, \boldsymbol{\rho_g})\right) \frac{\partial \mathbf{U}_j}{\partial \rho_s} - \boldsymbol{\lambda}_i^T \frac{\partial \mathbf{K}(\boldsymbol{\rho}, \boldsymbol{\rho_g})}{\partial \rho_s} \mathbf{U}_j + \boldsymbol{\lambda}_i^T \frac{\partial \mathbf{F}_j(\boldsymbol{\rho}, \boldsymbol{\rho_g})}{\partial \rho_s}, \tag{A.10}$$

that can be in turn written as:

$$\frac{\partial u_i}{\partial \rho_s} = -\boldsymbol{\lambda}_i^T \frac{\partial \mathbf{K}(\boldsymbol{\rho}, \boldsymbol{\rho_g})}{\partial \rho_s} \mathbf{U}_j + \boldsymbol{\lambda}_i^T \frac{\partial \mathbf{F}_j(\boldsymbol{\rho}, \boldsymbol{\rho_g})}{\partial \rho_s}, \tag{A.11}$$

where $\boldsymbol{\lambda}_i$ satisfies the adjoint equation:

$$\mathbf{K}(\boldsymbol{\rho}, \boldsymbol{\rho_g}) \boldsymbol{\lambda}_i = \left(\frac{\partial u_i}{\partial \mathbf{U}_j}\right)^T = \mathbf{L}_i. \tag{A.12}$$

The derivatives in Eqn.(A.11) can be evaluated accounting for the material law in Eqn.(3.10). The sensitivity of the objective function and the weight constraint in Eqn.(3.11c) are straightforward. The derivatives with respect to the filtered variables ($\tilde{\rho}_e$, $\tilde{\rho}_{g,e}$) and the projected ones ($\widehat{\rho}_e$, $\widehat{\rho}_{g,e}$) can be easily evaluated by applying the chain rule to Eqn.(B.1) and Eqns.(A.3-A.4), respectively. It is also remarked that, at each iteration, only one inverse of the stiffness matrix $\mathbf{K}(\boldsymbol{\rho}, \boldsymbol{\rho_g})$ must be computed to evaluate constraints and their sensitivities. Indeed the linear systems in Eqn.(3.11b) and Eqn.(A.8) share the same coefficient matrix.

A.5. Topology Optimization Accounting for Self-Weight - Optimal Grading for an Infill Problem

As an additional design test, an infill problem is dealt with, addressing a $4L \times L$ simply-supported beam. The rectangular shape of the boundary is fixed, and the infill of minimum weight is sought considering the structural response to two types of load: (i) a uniformly distributed one acting along the upper edge and (ii) self-weight. Due to symmetry in load and geometry, only the right half of the beam is discretized, as shown in Figure 3.7c. A mesh of 200×100 square finite elements is adopted to perform the numerical study.

The formulation in Eqn.(3.11) is implemented, controlling the vertical displacement of each one of the unrestrained nodes located along the lower edge of the specimen. As detailed in Section 3.2, when dealing with infill problems, $\rho_{g,min}$ and $\rho_{g,max}$ are enforced through side constraints. The adoption of the two-phase material law of Section 3.1.2 prevents the arising of porous material in the range $\rho_{g,max}$=1. Void is not allowed, because $\rho = \rho_g = 0$ is not a feasible solution for the problem. No control is operated on the minimum amount of graded material,

i.e. $f_g = 0$ is set in Eqn.(3.11d).

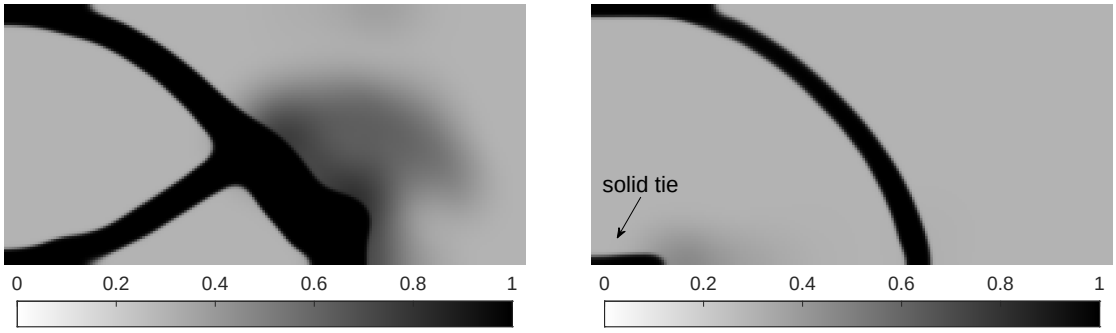

(a) Considering only distributed load, $V/V_0 = 0.491$ (b) Considering only self-weight, $V/V_0 = 0.354$

Figure A.2: Example 3. Optimal designs-1.

At first, the optimization is performed considering only the distributed load. The map of element densities $\rho_e + (1-\rho_e)\rho_{g,e}$ achieved by the implemented multi-constrained formulation is given in Figure A.2a. The weight ratio at convergence reads $V/V_0 = 0.491$. This means that the weight of the filled specimen is nearly one half of the specimen made of full material (whereas the deflection of the former is one and half that of the latter). In the inner part of the specimen a sort of lenticular truss arises. Two chords made of full material surround an inner area of porous phase, whose density is nearly homogeneous and equal to $\rho_{g,min}$. In the lateral overhang, load transferring is provided by the graded porous phase only. The highest density of the porous material is found within a region centered on the beam support.

Then the optimization is performed considering only the self-weight, which is implemented as a consistent load in the finite element model. The final result is presented in Figure A.2b. The solid phase consists of an arch-like structure spanning between the supports. The horizontal thrust is sustained by a solid tie, which spreads in porous material when moving towards the restraints. Porous material of lower density arises elsewhere. The weight ratio of the this optimal layout reads $V/V_0 = 0.354$. This means that, reducing by approximately two third the weight of the specimen made of full material, the maximum deflection increases by half. Indeed, removing material implies not only a loss in stiffness, but also a decrease in load, see the non-monotonous sensitivity in Eqn.(A.11). This was originally discussed in [28], addressing design-dependent minimum compliance problems of topology optimization.

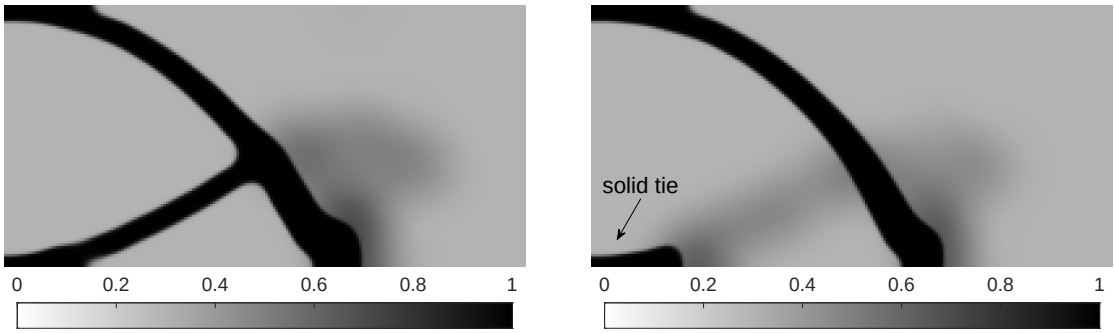

(a) Considering distributed load and self-weight, $V/V_0 = 0.425$

(b) Considering half distributed load and self-weight, $V/V_0 = 0.354$

Figure A.3: Example 3. Optimal designs-2.

In Figure A.3, optimal results found for loads i) and ii) that act simultaneously are shown. At first, it is assumed that the resultant of the distributed load equals the weight of the entire specimen made of full material. The achieved design, see Figure A.3a, is similar to that found when considering only the distributed load. However, the chords of the lenticular truss are thinner and the porous material around the support is less dense. This implies a lower weight ratio, namely $V/V_0 = 0.425$. Then, self-weight is coupled with a distributed load with half the intensity considered above. In this case, the design is dominated by the design-dependent load. A heavier version of the solution shown in Figure A.2b is represented in Figure A.3b. In this case, a region of graded material with $\rho_{g,e} > \rho_{g,min}$ connects the tie to the outer arch, while strengthening the overhang next to the support. The weight ratio at convergence, namely $V/V_0 = 0.404$, is lower than that of the design in Figure A.3a.

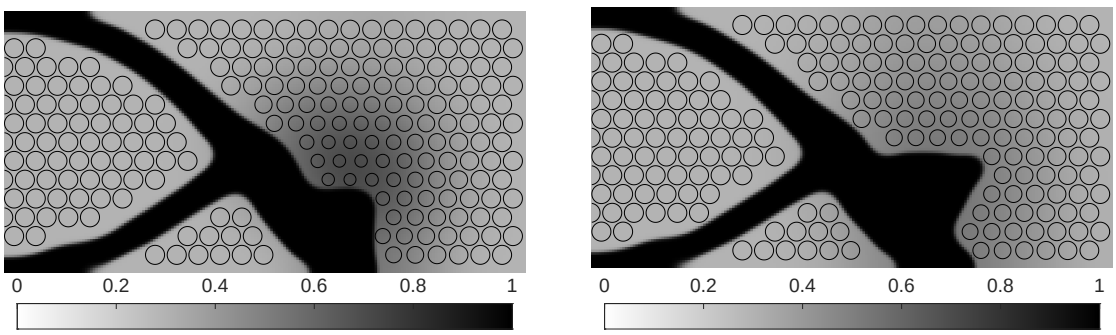

(a) $r_{g,f} = 4r_f$, $V/V_0 = 0.495$

(b) $r_{g,f} = 6r_f$, $V/V_0 = 0.500$

Figure A.4: Example 3. Overlay of the HPC circular holes ($d = L/12$) and of the optimal distribution of material density considering distributed load only.

The optimization of the infill considering only the distributed load is revisited by investigating the effect of an increase in the filter radius adopted to manipulate the porous phase $r_{g,f}$. In Figure A.4a and A.4b the optimal distribution of material density is given as found using $r_{g,f} = 4r_f$ and $r_{g,f} = 6r_f$, respectively. In the same pictures, the set of the graded circular holes that may be computed for $d = L/12$ according to the post-processing procedure detailed in Section 3.2.3 is given, as well. As expected, an increase in $r_{g,f}$ promotes a smoother variation in the spatial distribution of $\rho_{g,e}$. This has a minor effect on the final weight, whereas some impact is reported also on the distribution of the solid phase. Reference is made to the layout in the vicinity of the support in Figure A.4a and in Figure A.4b, compared to that shown in Figure A.2a.

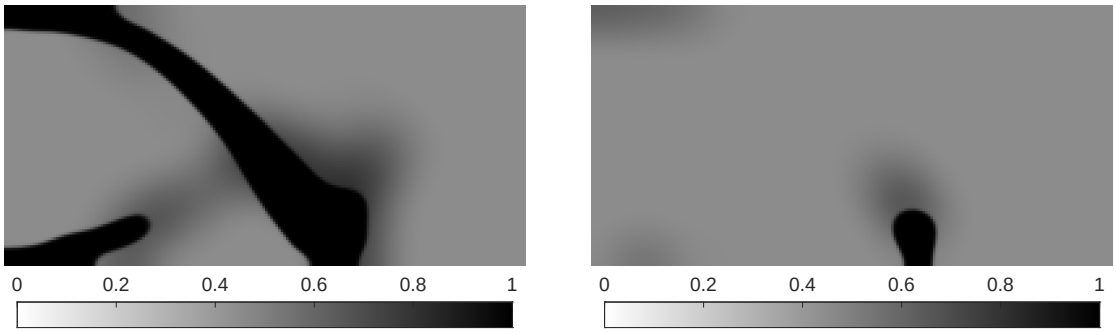

(a) Considering only distributed load, $V/V_0 = 0.574$ (b) Considering only self-weight, $V/V_0 = 0.469$

Figure A.5: Example 3. Optimal design with $\rho_{g,min} = 0.45$.

A further test is performed considering the optimal infill problem while enforcing $\rho_{g,min} = 0.45$, instead of the value adopted in the previous simulations ($\rho_{g,min} = 0.30$). This is operated as a modification of the side constraints of the variables $\rho_{g,e}$. The case of distributed load only, and self-weight only are considered, see results in Figure A.5. The infill problem is particularly sensitive to $\rho_{g,min}$. By comparing the achieved solutions with those already found for the reference value, see Figure A.2b, noticeable changes in terms of both design and weight ratio may be pointed out. When the distributed load is applied, part of the solid lenticular truss is replaced by porous material and the overall increase in weight is around 15%. Considering the self-weight only, the solid structure disappears in favour of graded material, except for a small region around the support. With respect to the reference solution, this costs an increase in terms of weight around 25%.

B | Appendix B

B.1. Filtering

The specialization of the standard linear filter [20, 21] to filtering the problem introduced in Chapter 4 is addressed. The original variables $\rho_{1,e}$, $\rho_{2,e}$, $\rho_{g,e}$ are mapped to the new sets $\tilde{\rho}_{1,e}$, $\tilde{\rho}_{2,e}$ and $\tilde{\rho}_{g,e}$ as follows:

$$\tilde{\rho}_{1,e} = \frac{1}{\sum_n H_{1,es}} \sum_n H_{1,es}\,\rho_{1,e}, \;\; \tilde{\rho}_{2,e} = \frac{1}{\sum_n H_{2,es}} \sum_n H_{2,es}\,\rho_{2,e}, \;\; \tilde{\rho}_{g,e} = \frac{1}{\sum_n H_{g,es}} \sum_n H_{g,es}\,\rho_{g,e} \tag{B.1a}$$

$$H_{1,es} = \max(0, r_{1,f} - d_{e,s}), \;\; H_{2,es} = \max(0, r_{2,f} - d_{e,s}), \;\; H_{g,es} = \max(0, r_{g,f} - d_{e,s}) \tag{B.1b}$$

where $d_{e,s}$ is the distance between the centroid of the e-th and s-th element, whereas $r_{1,f}$, $r_{2,f}$ and $r_{g,f}$ are the filter radius used for $\rho_{1,e}$, $\rho_{2,e}$ and $\rho_{g,e}$, respectively. The filters on $\rho_{1,e}$ and $\rho_{2,e}$ can be used to control heuristically the minimum size of the features arising in the optimal layout, for solid and porous material respectively. The filter for $\rho_{g,e}$ can be used to promote a smooth variation of the density of the graded material throughout the region occupied by the porous phase.

The filtered densities $\tilde{\rho}_{1,e}$ and $\tilde{\rho}_{2,e}$ are mapped to the set of projected (physical) densities $\widehat{\rho}_{1,e}$ and $\widehat{\rho}_{2,e}$, respectively, in order to achieve 0-1 solutions, i.e. a clear separation between full material and porous material or void. The formulation proposed in [153] is herein adopted:

$$\widehat{\rho}_{1,e} = \frac{\tanh(\beta\eta) + \tanh(\beta(\tilde{\rho}_{1,e} - \eta))}{\tanh(\beta\eta) + \tanh(\beta(1-\eta)}, \;\; \widehat{\rho}_{2,e} = \frac{\tanh(\beta\eta) + \tanh(\beta(\tilde{\rho}_{2,e} - \eta))}{\tanh(\beta\eta) + \tanh(\beta(1-\eta)}, \tag{B.2}$$

with threshold $\eta = [0,1]$ and sharpness factor $\beta = [1,\infty]$ in both cases. The Heaviside function projects densities below the threshold to 0 and densities above it to 1, depending on the value of the sharpness factor, see e.g. [66, 74]. In the numerical section $\eta = 0.5$, whereas β is smoothly increased during the simulations from 2 to 16 by means of the continuation approach in [58].

B.2. Sensitivity Computation

The derivative of Eqn.(4.10) with respect to the element unknown ρ_k, which can be indifferently an entry of $\boldsymbol{\rho_1}$, $\boldsymbol{\rho_2}$ or $\boldsymbol{\rho_g}$, may be computed as:

$$\sum_{j=1}^{l} \frac{\partial u_{i,j}^{unit}}{\partial \rho_k} \bar{f}_j + \Phi^{-1}(q)(\mathbf{u}_i^{unit})^T \mathbf{K}_{ov} \frac{\partial \mathbf{u}_i^{unit}}{\partial \rho_k} \left((\mathbf{u}_i^{unit})^T \mathbf{K}_{ov} \mathbf{u}_i^{unit} \right)^{-1/2}, \tag{B.3}$$

The sensitivity of $u_{i,j}^{unit}$ may be computed through the adjoint method, see e.g. [16]. Accordingly, $u_{i,j}^{unit}$ in Eqn.(4.6) does not change when adding at the right hand side a zero function derived from the equilibrium of Eqn.(4.5b):

$$-\boldsymbol{\lambda}_i^T \left(\mathbf{K}(\boldsymbol{\rho_1}, \boldsymbol{\rho_2}, \boldsymbol{\rho_g}) \mathbf{U}_j^{unit} - \mathbf{F}_j^{unit} \right), \tag{B.4}$$

where $\boldsymbol{\lambda}_i$ is any arbitrary but fixed vector and it is assumed that $\mathbf{F}_j$ does not depend on $\boldsymbol{\rho_1}, \boldsymbol{\rho_2}, \boldsymbol{\rho_g}$. After re-arrangement of terms, the derivative of $u_{i,j}^{unit}$ with respect to the element unknown ρ_k reads:

$$\frac{\partial u_{i,j}^{unit}}{\partial \rho_k} = \left(\boldsymbol{L}_i^T - \boldsymbol{\lambda}_i^T \mathbf{K}(\boldsymbol{\rho_1}, \boldsymbol{\rho_2}, \boldsymbol{\rho_g}) \right) \frac{\partial \mathbf{U}_j^{unit}}{\partial \rho_k} - \boldsymbol{\lambda}_i^T \frac{\partial \mathbf{K}(\boldsymbol{\rho_1}, \boldsymbol{\rho_2}, \boldsymbol{\rho_g})}{\partial \rho_k} \mathbf{U}_j^{unit}, \tag{B.5}$$

that can be in turn written as:

$$\frac{\partial u_{i,j}^{unit}}{\partial \rho_k} = -\boldsymbol{\lambda}_i^T \frac{\partial \mathbf{K}(\boldsymbol{\rho_1}, \boldsymbol{\rho_2}, \boldsymbol{\rho_g})}{\partial \rho_k} \mathbf{U}_j^{unit}, \tag{B.6}$$

where $\boldsymbol{\lambda}_i$ satisfies the adjoint equation:

$$\mathbf{K}(\boldsymbol{\rho_1}, \boldsymbol{\rho_2}, \boldsymbol{\rho_g}) \boldsymbol{\lambda}_i = \left(\frac{\partial u_{i,j}^{unit}}{\partial \mathbf{U}_j^{unit}} \right)^T = \mathbf{L}_i. \tag{B.7}$$

The derivatives in Eqn.(B.6) can be evaluated accounting for the material law in Eqn.(4.1). The sensitivity of the objective function and the weight constraint in Eqn.(4.5c) are straightforward. The derivatives with respect to the filtered variables ($\tilde{\rho}_{1,e}$, $\tilde{\rho}_{2,e}$. $\tilde{\rho}_{g,e}$) and the projected ones ($\widehat{\rho}_{1,e}$, $\widehat{\rho}_{2,e}$) can be easily evaluated by applying the chain rule to Eqns.(B.1) and Eqns.(B.2), respectively. It is also remarked that, at each iteration, only one inverse of the stiffness matrix $\mathbf{K}(\boldsymbol{\rho_1}, \boldsymbol{\rho_2}, \boldsymbol{\rho_g})$ must be computed to evaluate constraints and their sensitivities. Indeed the linear systems in Eqn.(4.5b) and Eqn.(B.4) share the same coefficient matrix. The overall process is repeated until convergence is achieved, i.e. the maximum difference in terms of the values of the set of minimization unknowns $\rho_{1,e}$, $\rho_{2,e}$ and $\rho_{g,e}$ between two subsequent steps is less than 10^{-3}.

B.3. Preliminary Assessment of the Three-variable Multi-scale Approach, a Cantilever

A preliminary assessment of the numerical implementation of the formulation introduced in Chapter 4 is herein given addressing the cantilever beam sketched in Figure 4.3a. Filter radii $r_{1,f} = r_{2,f} = L/30$ and $r_{g,f} = L/10$ are assumed in this investigation.

A deterministic problem of volume-constrained minimum compliance for the cantilever represented in Figure 4.3a has been tackled. The result found using the displacement-constrained formulation of Eqn.(4.5), assuming deterministic load f_1, $\alpha = 3.0$, $f_g = 0$, and $0.05 \leq \rho_g \leq 0.65$, is shown in Figure B.1. The achieved layout is independent on the type of infill selected in the material interpolation law of Eqn.(4.1). The weight at convergence is $V/V_0 = 0.252$. The optimal topology is in good agreement with those found in [137] when investigating minimum compliance design for low volume fraction and small filter radius, both working with SIMP and using an interpolation scheme based on the Hashin-Strikhman upper bounds for bulk and shear moduli.

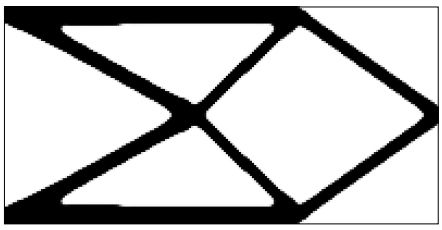

Figure B.1: Example 1. Optimal design in case of a deterministic force f_1, $V/V_0 = 0.252$.

The displacement-constrained formulation of Eqn.(4.5) is then tested for probabilistic loading, assuming unitary average value $\bar{f}_1$ and coefficient of variation $CV_1 = 0.15$. Denoting by u_1 the vertical displacement at the point loaded by $\bar{f}_1$, the deterministic inequality that is equivalent to the probabilistic displacement constraint simplifies to:

$$c_1 u_1 \leq u_{lim}, \text{ with } c_1 = 1 + \Phi^{-1}(1 - P_{fail})\sigma_1,$$

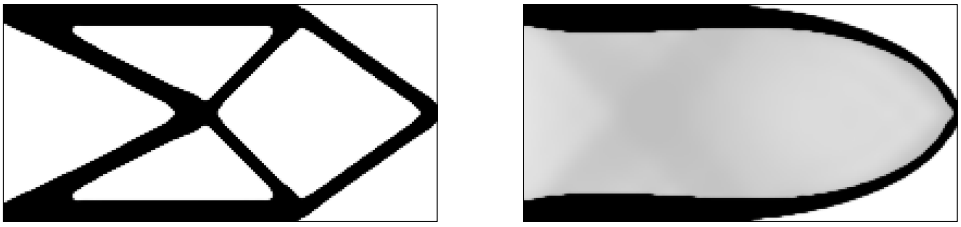

(a) $f_g = 0$, $V/V_0 = 0.300$

(b) $f_g = 0.125$ with an infill of diamond lattice (D), $V/V_0 = 0.318$

Figure B.2: Example 1. Optimal design in case of a force f_1 with $CV_1 = 0.15$

see Eqns.(4.10) and (4.11). This is in turn equivalent to solving a deterministic problem in which the controlled displacement cannot exceed $1/c_1 \cdot 3.0 = 2.52$ times that computed adopting $\rho_1 = 1$ everywhere. The allowed displacement $1/c_1 \cdot u_{lim}$ is nearly 16% less than the limit prescribed in the problem involving deterministic loading (u_{lim}). The optimal design found for $f_g = 0$ in case of probabilistic loading is represented in Figure B.2a. Again, the solution is independent on the type of infill selected in the material interpolation law. The achieved layout is similar to that shown in Figure B.1, with an increase in terms of weight that is around 16%, as expected.

In Figure B.2b, the optimal design using an infill of diamond lattice is shown, as found enforcing $f_g = 0.125$ in the formulation of Eqn.(4.5). A composite structure arises that is made of an inner grey area, standing for low density infill, surrounded by a layer of solid material. The weight is nearly 6% larger than in the previous case. A similar layout was retrieved in [157] when investigating minimum compliance design using an interpolation scheme derived from the homogenization of a diamond lattice. The composite layout was shown to be a sub-optimal solution with respect to the design made of full material and void only. Indeed, the optimal solution was found using rank-2 laminates having orthogonal layers aligned with the principal stresses, see in particular [13]. This was expected, since the optimal set of elasticity tensors for rank-2 material is defined without any restriction related to the adoption of cells having given orientation.

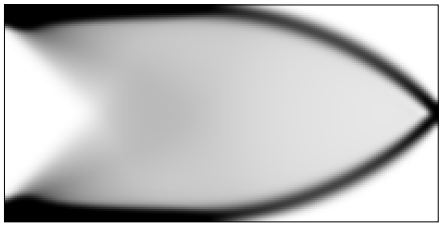

Figure B.3: Example 1. Optimal design using the code in [157] for rank-2 material, achieving $\alpha = 2.52$, $V/V_0 = 0.268$.

A final investigation on the cantilever of Example 1 is performed using the code provided in [157] for volume-constrained minimum compliance with rank-2 material. The input volume is iteratively changed to match a final value of the structural compliance corresponding to $\alpha = 1/c_1 \cdot 3.0 = 2.52$. The relevant distribution of rank-2 material is that represented in Figure B.3. The weight is $V/V_0 = 0.268$, approximately 12% lighter than the design made of full material and void in Figure B.2a, and almost 19% lighter than the composite solution in Figure B.2b. This is in agreement with the findings reported above.

B.4. Effect of Different Correlations of Loads

Four cases for Example 2 in Chapter 4 were considered to test the method in case of different correlation of the applied forces, i.e.:

$$\begin{aligned}
&\text{case}\,A\text{:}\quad r_{12} = r_{23} = r_{34} = 0.5,\ r_{13} = r_{24} = -0.5,\ r_{14} = -1,\\
&\text{case}\,B\text{:}\quad r_{12} = r_{13} = r_{14} = r_{23} = r_{24} = r_{31} = -0.33,\\
&\text{case}\,C\text{:}\quad r_{12} = r_{13} = r_{24} = r_{34} = -1,\ r_{14} = r_{23} = 1,\\
&\text{case}\,D\text{:}\quad r_{12} = r_{14} = r_{23} = r_{34} = -1,\ r_{13} = r_{24} = 1.
\end{aligned}$$

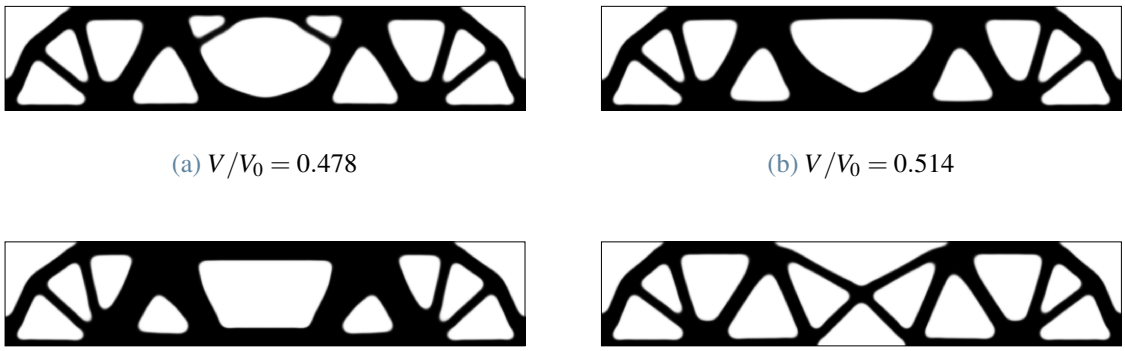

(a) $V/V_0 = 0.478$ (b) $V/V_0 = 0.514$

(c) $V/V_0 = 0.551$ (d) $V/V_0 = 0.407$

Figure B.4: Example 3. Optimal design in case of correlated forces for different values of the correlation ($CV = 0.25$ for all forces, $P_{fail} = 0.1$)

The achieved optimal layouts are reported in Figure B.4. In case A, the correlation of any force is positive with forces whose application point is not farther than L, otherwise negative. It is recalled that, for positive correlation two variables tend to change in the same direction, whereas negative correlation describes variables that tend to move in opposite direction from one another. The relevant design, see Figure B.4a, is lighter than that found in case of uncorrelated loads, exhibiting a slightly different design only in the central region. In case B, addressing negative correlation for all the forces, the optimal layout, see Figure B.4b, has the same topology of that represented in Figure 4.9, with a minor increase in terms of weight. Case C addresses perfectly positive correlation between the forces applied at the tip of the overhangs and between those applied in the central span, whereas perfectly negative correlation is prescribed between forces of the former and the latter group. The relevant optimal design is that represented in Figure B.4c. In the central region of the specimen only horizontal bars arise, since no shear is expected. However, the overall weight is 10% larger than for uncorrelated forces, due to the increased bending moments the specimen is likely to undergo. In case D, perfectly positive correlation is assumed between f_1 and f_3, and between f_2 and f_4, whereas perfectly negative correlation for the remaining combinations. The relevant optimal design, which is represented in Figure B.4d, is characterized by a cross-shaped layout in the central region that provides bracing according to the expected shear internal action. In this case, the optimal layout is much lighter (nearly 20%) than that found when no correlation is assumed among the forces.